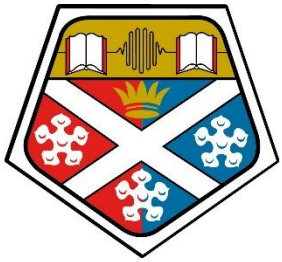

University of Strathclyde Glasgow

Supramolecular Chemistry for the application to hair dye technology

Lloyd Farquhar

Thesis submitted to the Strathclyde Institute of Pharmacy and Biomedical Sciences at the University of Strathclyde in accordance with the requirements for the Degree of the Doctor of Philosophy

December 2022

Declaration of Authenticity

This thesis is the result of the author's original research. It has been composed by the author and has not been previously submitted for examination which has led to the award of a degree.

Abstract

This thesis investigates the use of co-crystallisation and crystal engineering to create novel coloured co-crystalline materials (*i.e.* co-crystals or salts) which can be used to colour hair. Based on the limited previous work on supramolecular hair dyes, we attempted to increase the range of available colours.

Firstly, the solution reactivity of *p*-phenylenediamine (PPD) was investigated through the use of UV/Vis, HPLC, LC-MS and NMR spectroscopy which was monitored over three months. The colour of the PPD solutions was observed to change from colourless to a deep red/black during this time which suggested that oxidation was possibly occurring which was confirmed through the use of HPLC, LC-MS and NMR. These techniques, particularly LC-MS allowed us to identify the nature of these oxidation products.

Secondly, the effect small structural changes to PPD would have on the resultant colour was investigated using *o*-phenylenediamine (OPD), *m*-phenylenediamine (MPD) and 4-iodoaniline (4IODAN). The results showed small shifts by UV/Vis occurring over time which from the PPD work in the previous chapter was more likely a result of oxidation. The impact of ionisation was also investigated through ionic co-crystals of PPD which were unsuccessful, although formation of the HCl salt did result in a colour change in the solution state.

Lastly, alizarin was screened for new multi-component forms that could extend the range of available colours. A new pyridine solvate as well as three new co-crystals were identified through solution crystallisation and ball milling experiments. An additional ALZ-PHN co-crystal was identified through liquid-assisted grinding (LAG) experiments which was isostructural to the ACR co-crystal. UV/Vis analysis of these new crystalline materials identified did not show any shift in colour with respect to ALZ and as a result did not offer any advantage over pure ALZ.

Acknowledgments

Firstly, I'd like to thank my supervisor Dr Iain Oswald for your support and guidance throughout the years. Particularly in the early years, our weekly meetings and conversations were invaluable for the success of this project and I'm very thankful for your continued support and advice during the long write up process. I also want to thank my industrial supervisor Dr Daniel Nowlan for his wealth of knowledge and expertise in hair colour chemistry and for always providing a help handing with mass spec and NMR interpretation. Thanks to the Aveda Corporation for funding my PhD.

Thanks to fellow group members of the Oswald group, Dr Abdullah Al Balushi, Dr Lauren Connor, Dr Suse Bebiano, Dr Martin Ward and Eleanor Jones for all of your help, words of advice, training in the lab and for making it a great 3 years. Thanks to Dr Darren Edwards and Dr Dave Watson for all of your help and advice regarding problems with HPLC and LC-MS.

I would like to thank my work colleagues at Johnson Matthey for their continued support over the last few years, in particular Dr Mateusz Pitak, Dr Suzanne Buttar and Dr Craig Grant for allowing me time off to get this PhD finished, it's very much appreciated.

Finally, I'd like to thank my family and close friends for their continued support and encouragement, it's really appreciated and helping get me over the line.

Contents

List of Figures

List of Tables

List of Abbreviations

Acetonitrile	MeCN
Active Pharmaceutical Ingredient	API
Crystal Structure Prediction	CSP
Differential Scanning Calorimetry	DSC
Dimethylsulfoxide	DMSO
High Performance Liquid Chromatography	HPLC
4-iodoaniline	4IODAN
Lawsone	L
Liquid Chromatography Mass Spectrometry	LC-MS
Liquid Assisted Grinding	LAG
m-phenylenediamine	MPD
Neat Grinding	NG
Nuclear Magnetic Resonance	NMR
Oxidative Hair Dye's	OHD's
o-phenylenediamine	OPD
Powder X-ray Diffraction	PXRD
p-phenylenediamine	PPD
Sebacic Acid	SebA
Single Crystal X-ray Diffraction	SCXRD
Thermogravimetric Analysis	TGA
Trimesic Acid	TMA

Chapter One - Introduction

1 Introduction

1.1 Polymorphism and Physical Properties

In the design and synthesis of functional solid materials, the ability to control the solid-state assembly of molecules into crystals is of paramount importance and as a result significant effort has gone into the study of polymorphism.[1] Polymorphism is the ability of a compound to exist in multiple crystal forms as a result of differences in molecular conformation and/or in the molecular packing arrangement that leads to potential differences in physiochemical properties including melting point, stability and solubility, *etc.*[2-3] These differences in physiochemical properties can hugely impact pharmaceutically important parameters, *e.g.* tabletability, bioavailability and dissolution rate, therefore it is vital that the polymorphism of an API is tightly controlled to ensure the medicine's properties are reliable.[4] Polymorphism is a well-known occurrence in both inorganic and organic compounds as well as proteins hence it is critical to have a deep understanding, if not, control over it so as to direct the materials functional properties to particular scientific led challenges.[5] This phenomenon perhaps tends to be more prominent in molecules that display multiple hydrogen bonding moieties, forming multiple supramolecular synthons and/or conformational flexibility as was observed with 5-methyl-2-[(2-nitrophenyl)amino]-3-thiophenecarbonitrile (ROY) and various active pharmaceutical ingredients (APIs) including piracetam[6], virazole[7] and aspirin.[8]

Conformational polymorphism is the term for the occurrence of polymorphism from different conformations of the same molecule.[9] The best example of conformational polymorphism is ROY exhibiting seven polymorphic forms which have been structurally characterised by single crystal X-ray diffraction with an eighth form being characterised more recently using a combination of crystal structure prediction (CSP) and X-ray powder diffraction.[10-11] In recent years, several heavily polymorphic compounds have come to light including aripiprazole[12] and flufenamic acid[13] which have eleven (eight fully characterised) and nine (six fully characterised) known polymorphs respectively. More recently, galunisertib (GAL) has emerged as the current leader with ten structurally characterised polymorphs, the highest number to date.[14] In addition, concomitant polymorphism which is the crystallisation of polymorphic crystals from the same conditions can take place under certain conditions.[15-16] The formation of concomitant polymorphs are influenced by the crystallisation kinetics and thermodynamics of the crystal packing. Studies have argued that this phenomenon results from variation in molecular conformation, differences in intermolecular interaction and crystal packing.[17]

Amorphous solids are materials in which the atom's arrangements lack any long-range order, which is characteristic of crystalline solids, although amorphous solids may have short-range molecular order similar to crystalline solids.[18-19] Amorphous materials can be considered liquid which have been solidified through the removal of solvent/thermal energy in a way that circumvents crystallisation.[19] Amorphous drugs, unlike crystalline drugs, are more disordered at the molecular level in their physical structures as a result of their lack of long-range order which as a result leads to a reduction in lattice energy and an increase in the Gibbs free energy.[20] The low density/high free energy of the amorphous phase results in amorphous drugs dissolving faster than crystalline drugs, however, their metastable nature and conversion to the crystalline state during storage are major concerns for drug developers.[21] Amorphous solid dispersions are highly desirable for the improvement of poorly water-soluble drugs and are widely used for stabilisation of a drug's amorphous state by dispensing it in active carriers, *e.g.* polymers.[22-23] Co-amorphous technology has recently been introduced as a way of stabilising amorphous drugs for drug development.[23] Co-amorphous phases are defined as "multi-component single phase amorphous solids in which the drug is stabilized through intermolecular interactions with a co-former lacking long-range periodic arrangement in the solid phase".[24] The co-amorphous formulations may contain molecules, solvates or salts and can consist of a single active pharmaceutical ingredient (API) and a small molecule excipient. These co-amorphous formulations can improve the solubility/dissolution rates through the presence of different intermolecular interactions between the components. Co-amorphous systems are similar to co-crystals with the advantage of greater molecular configuration variety/higher relative energy and the disadvantage of metastability.[25]

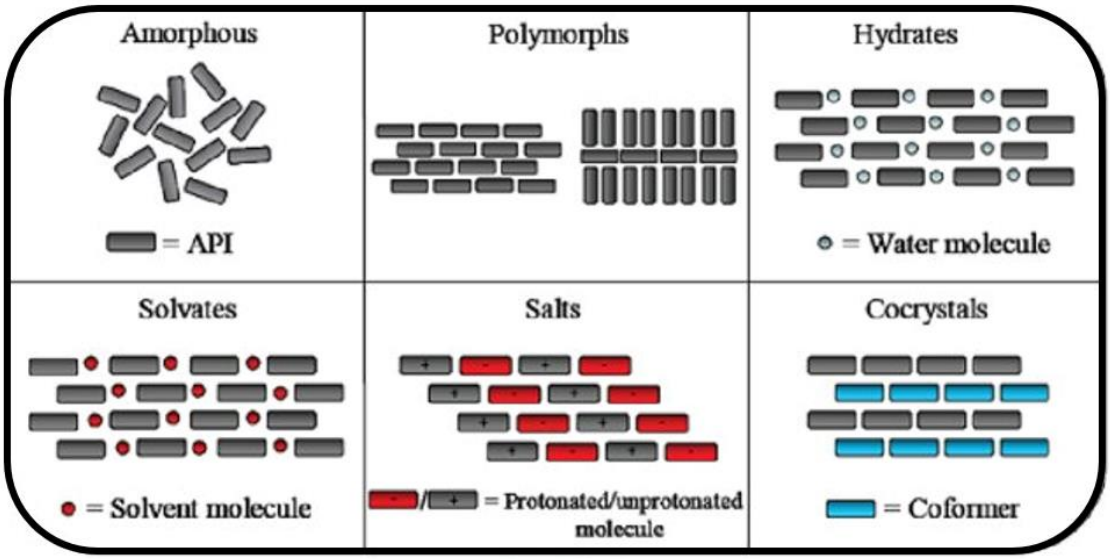

Figure 1.1: Schematic representation of the different types of solid forms. Adapted from Thenge, R., Patel, R., Mahajan, N & Kayande, N. Co-crystallization- A Novel Prospective to Improve Physiochemical Properties of APIs. J Drug Deliv. Ther. 9, 351-357 (2019).

1.2 Crystal Engineering

The concept of creating crystalline solids by design or with a purpose is reflected in the term "crystal engineering" which was first coined by Pepinsky in 1955 during a meeting of the American Physical Society.[26] Crystal engineering contributes an understanding of the intermolecular interactions which govern crystal packing allowing the design of new solids with tailored chemical and physical properties.[27] Crystal engineering has been defined as "the understanding of intermolecular interactions in the context of crystal packing and the utilisation of such understanding in the design of new solids with desired physical and chemical properties".[26–28] The use of weak intermolecular interactions in crystal engineering, *e.g.* hydrogen and halogen bonds, in combination with molecular flexibility can be tuneable through the use of appropriate molecular design allowing for the molecules to assemble into desired packing arrangements. This is of vital importance as organic molecules can assemble into a range of crystal forms, termed polymorphs which show differing chemical and physical properties, with the design of molecular packing architectures requiring a thorough understanding of intermolecular interactions as well as the molecular flexibility.[29-30]

The term "synthon" was first introduced by Corey in 1967 and has been defined as "structural units within molecules which can be formed and/or assembled through known conceivable synthetic operations" which also contains chemical and geometrical information necessary for functional group recognition in molecular solids.[31-32] Supramolecular synthons which is a concept developed by Desiraju can be utilised to form co-crystals of APIs and is of vital importance in crystal engineering as they are a modular representation between functional groups and can be categorised into homo and heterosynthons.[33–35] Zawortoko *et al.* distinguished between supramolecular homosynthons which are comprised of identical complementary functional groups, *e.g.* amide dimers and carboxylic acid dimers and supramolecular heterosynthons which are comprised of different, but complementary functional groups, *e.g.* hydroxyl-aromatic nitrogen, acid-aromatic nitrogen and acid-amide.[36]

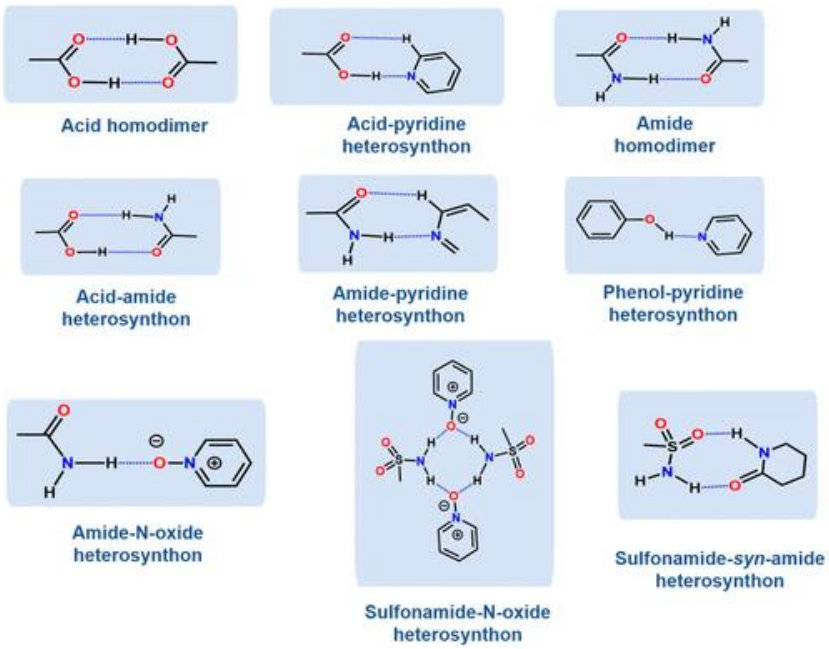

Figure 1.2: The common supramolecular synthons utilised in crystal engineering. Adapted from Bolla, G., Sarma, B. & Nangia, A. K. Crystal Engineering of Pharmaceutical Cocrystals in the Discovery and Development of Improved Drugs. Chem. Rev. **122**, 11514–11603 (2022).

1.2.1 Hydrogen and Halogen Bonding

The hydrogen bond is the most important of all the intermolecular interactions which has been used extensively in crystallisation control and structural design with it being the most reliable interaction in a crystal engineer's toolkit.[30,37] The electrostatic contribution is the largest term in a typical hydrogen bond which also features a charge transfer contribution. The hydrogen bond can be defined as "an attractive interaction between a hydrogen atom from a molecule or a molecular fragment X−H in which X is more electronegative than H, and an atom or a group of atoms in the same or a different molecule, in which there is evidence of bond formation".[38] A classic hydrogen bond is denoted as X−H···Y−Z with X−H and Y−Z describing the hydrogen-bond donors and acceptors respectively with the attractive nature of the interaction represented by the dots. The energy of the hydrogen bonds ranges from 0.2-40 kcal/mol^{-1} with the polarization, electrostatic, dispersion, charge transfer and exchange repulsion forces determine the exact energy. Hydrogen bonds can be classified as weak, moderate or strong depending on their bond energies with weak hydrogen bonds being dominated by dispersive and electrostatic forces with energies of less than 4 kcal/mol^{-1}. Moderate hydrogen bonds are electrostatic in nature and have energies between 4-15 kcal/mol^{-1}, with strong hydrogen bonds being strongly covalent in nature and featuring energies between 15-40 kcal/mol^{-1}.

Defining the strength of a hydrogen bond is one consideration, however, the crystal structure is a balance of all forces. For pharmaceutically relevant or organic materials, the hydrogen-bonding patterns can be complex hence an efficient method was required to systematically and consistently decode the crystal structure into simple terms with this method known as graph set analysis. Graph set analysis is a method based on graph theory which categorises hydrogen-bond motifs in a manner that allows ease of comparison between crystal structures. Graph sets are descriptions like the crystallographer's space group or the organic chemist's empirical formula which provides information on the number of donor's and acceptor's used in a hydrogen-bonding pattern as well as the nature of the pattern.[39] The graph-set approach allows for even complicated hydrogen-bonding networks to be simplified to combinations of four simple patterns, specified by a descriptor: rings (R), intramolecular hydrogen-bonded patterns (S), chains (C) and other finite patterns (D). The pattern is given a subscript designating the number of hydrogen-bond donor's, d and a superscript designating the number of hydrogen-bond acceptor's, a. Additionally, the number of atoms in the pattern is known as the degree of the pattern and is denoted by n. The graph-set descriptor is shown below with G representing one of the four possible designators.[40]

$$G_d^a\ (n) \qquad \text{Equation 1.1}$$

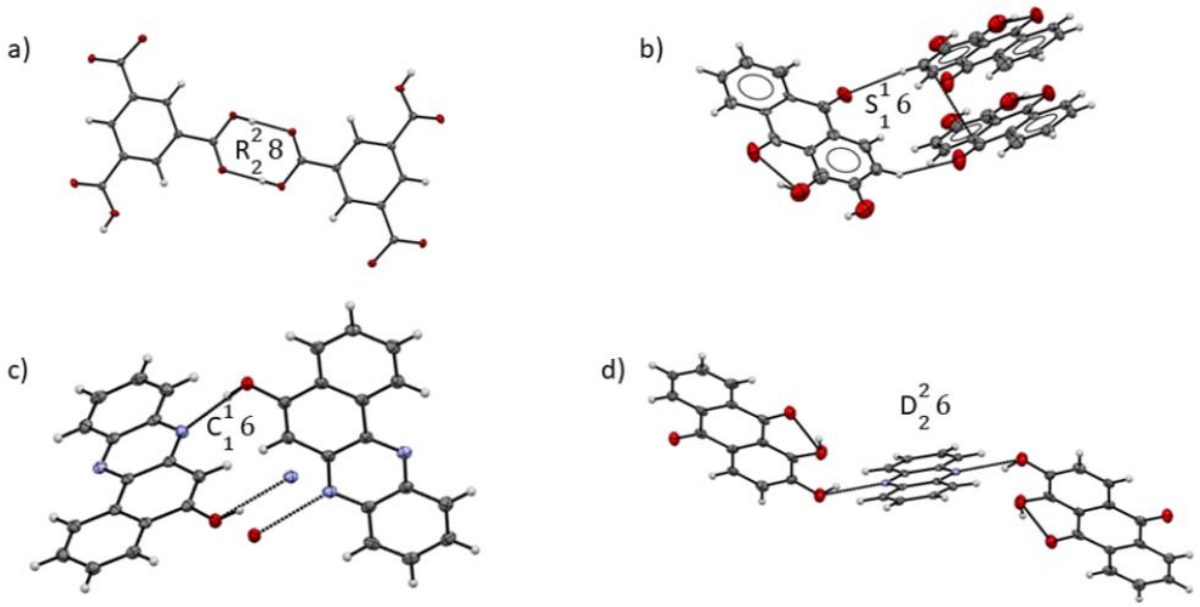

Figure 1.3: Examples of graph-set motifs presented in this thesis: a) MPD-TMA (1:1) salt, b) ALZ Form I, c) OPD-L and d) ALZ-PHN (2:1) co-crystal

Halogen bonding which is similar to hydrogen bonding in some ways belongs to the family of non-covalent interactions and the use of these non-covalent interactions in the creation of new materials and pharmaceutical ligands has only been established in the last decade.[41] Halogen bonding (XB) can be defined as a non-covalent interaction where halogen atoms (X = Br, Cl, I) act as electron acceptors which is considered to be an important tool in the field of crystal engineering.[42-43] This interaction resembles hydrogen bonding and has been proposed as a complementary tool in the rational modulation of molecular recognition events in the field of chemistry and biology.[44] The halogen bond has emerged as an effective tool for tailoring an APIs biophysical properties with recent studies where the halogen bond drives the self-assembly between an API and co-former.[45] A halogen bond R−X···Y−Z is formed when "there is evidence of a net attractive interaction between an electrophilic region associated with a halogen atom in a molecular entity and a nucleophilic region in another, or the same, molecular entity".[46] Halogen bonds tend to be more directional than hydrogen bonds with the R−X···B bond angle being closer to 180° which contains an electron-poor halogen-bond donor (X = I, Br, Cl, F) and an electron-rich halogen-bond acceptor (B). The distance between the X and B atoms is lower than the sum of their van der Waals radii. Halogen bonds bonding energy is up to 200 kJ mol^{-1} making it comparable to that of hydrogen bonds with the same charge-transfer interaction which allows halogen bonds to show similar trends to that of hydrogen bonds in terms of geometric and energetic properties. As X atoms are significantly larger than H and the interaction between X−B is more sensitive to secondary interactions/steric bulk.[47] It has also been shown that the strength of halogen bonds can be easily tuned through the choice of halogen and is also dependent strongly on the surroundings of which the halogen atom is bound.[48] The main

reason for the non-covalent interaction in halogen bonds is because of the presence of an area of positive charge along the extension of the C−X bond commonly termed as the σ-hole.[41]

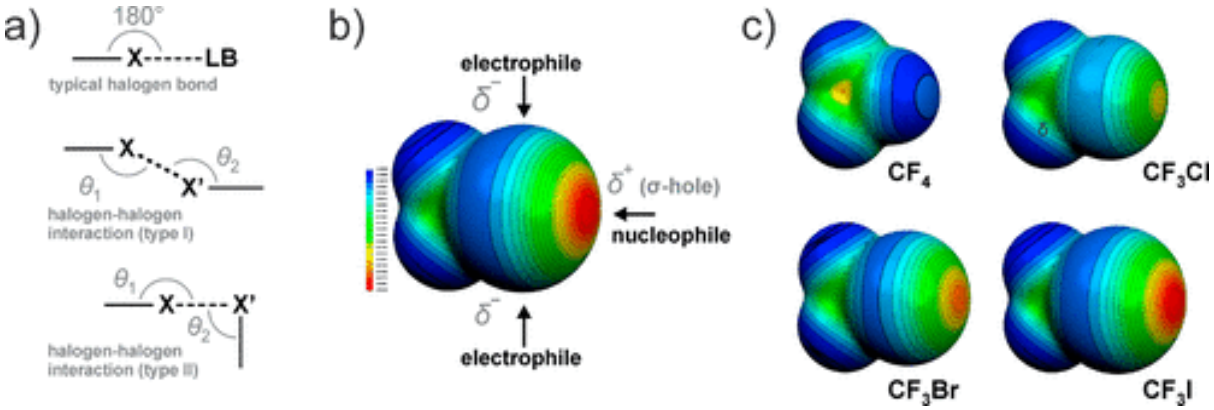

Figure 1.4: a) a typical halogen bond with Lewis Bases (LB) and the two known halogen-halogen interactions; b) CF_3I electrostatic potential map showing the positive/negative regions on iodine which normally participates in halogen bonding; c) CF_3I, CF_3Br, CF_3Cl, CF_4 electrostatic potential maps indicating how the σ-hole is shaped by the halogen-bond donor's polarizability. Adapted from Corpinot, M. K. & Bučar, D.-K. A Practical Guide to the Design of Molecular Crystals. Cryst. Growth Des. *(2018).*

The σ-hole concept was first introduced by Clark *et al.* in 2007 and arises when a group IVA-VIIA atom is bonded covalently to chemical functionalities that are more electronegative forming anisotropic distribution of electron density on the atoms resulting in regions which are more electron deficient than their surroundings.[49-50] The σ-hole can be defined as a "non-covalent interaction between a covalently-bonded atom of group IVB-VIIB and a negative site, *e.g.* an anion or a lone pair of Lewis base" involving a region of positive electrostatic potential positioned on the extension of the covalent bonds to the atom. This interaction is a consequence of the anisotropy of the atom's charge distribution.[51] The σ-hole bond is much more general compared to the halogen bond and other intermolecular interactions involving groups IVB-VIIB, even group VIIA, elements are only subsets and are special cases of the σ-hole. These σ-hole interactions are also capable of interacting with electron-rich sites to form directional and weak non-covalent interactions which resembles the halogen bond.[52]

1.2.2 π-π stacking interactions

It has been recognised that non-covalent interactions between aromatics referred to as π-π stacking interactions may play a pivotal role in a wide range of chemical systems.[53] These π-π stacking interactions are a direct attractive non-covalent interaction between aromatic rings which contain π orbitals and these π-π interactions between two aromatics can be classified into: parallel displaced, edge-to face T shape and cofacial parallel stacked.[53-54] Unsubstituted small aromatics prefer to adopt edge-to face T shape geometry, whereas large multi-ring and substituted aromatics prefer to adopt parallel displaced geometry.[55] The influence of parallel π-stacking on pyridine's hydrogen

bonding ability has recently been studied, as well as imidazole/pyrimidine stacking with a series of substituted benzenes investigating the job of orientation between stacked compounds. These studies showed that parallel stacking improves the bases hydrogen-bond accepting with this effect being greater for electron-donating benzene substituents compared to T-shaped stacking.[56]

1.2.3 Van Der Waals

The study of non-covalent or intermolecular interactions has long been vital to our understanding of complex molecular systems, especially when considering the assembly of molecules into supramolecular synthons. Predicting and studying cohesion in molecular materials heavily relies on accurate and physically realistic treatments for the various intermolecular interactions rising in such materials with those resulting from the instantaneous fluctuations of electrons referred to as dispersion or van der Waals interactions. Although they are generally weaker than hydrogen bonds or electrostatic interactions, their ubiquity and long-ranged nature in all molecular systems means they can play a pivotal role in non-covalent bonding.[57] Van der Waals forces are weaker than covalent bonds and the solids held together by van der Waals forces are softer in nature and feature lower melting points in comparison to other solids. These forces are never saturated/diminished and are independent of direction with the strength of this force being less, so it's not commonly observed in large molecules greater than 10 μm due to it being linear to particular diameter. The permanent dipoles result in distortion of the electric charge as well as shifting the electrostatic charge to the neighbouring non-polar/polar molecules and induce polarizability. The attractive forces between the ion and the permanent dipole are known as a dipole-induced dipole/Debye force and an energy of 1-3 kcal/mol^{-1} is required for this interaction.[58]

1.2.4 Co-crystallisation

Co-crystallisation is a crystal engineering approach used in the formation of new multi-component crystalline solids which uses complementary molecules based on molecular recognition and supramolecular chemistry principles.[59] The aim of co-crystallisation is to modify the physiochemical properties of APIs by altering the solubility, chemical stability, bioavailability, dissolution rate, hygroscopicity, mechanical behaviour, *etc.*[60] Co-crystallisation is a powerful application of crystal engineering which has been efficaciously employed in a range of fields over the last decade including high-energy materials, agrochemicals, food, pharmaceuticals, *etc.*[61]

An API can display several solid forms including hydrates, solvates, polymorphs, co-crystals and salts which can be explored during drug development. Polymorphic forms of an API represent alternative arrangements of the same material in the crystal structure that can be viewed as the simplest solid form given that the remaining solid forms are comprised of more than one component. Solvates are crystalline materials in which the crystal structure contains a solvent molecule, which are termed "hydrates" when the included guest or crystallisation solvent is water.[62] Salts and co-crystals are both classified as multi-component materials depending on whether the transfer of a proton from an acid to a base has occurred.[63] The pK_a rule is often used to predict whether an acid-base pair of compounds will crystallise as a co-crystal or a salt, and the rule states that a pK_a difference between the co-crystallising acid and base is greater than 2 or 3, then salt formation is expected. For $\Delta pK_a > 4$, ionised acid-base complexes are observed exclusively, whereas a $\Delta pK_a < -1$ results in non-ionised acid-base complexes.[64] There are many definitions reported in the literature for co-crystals, however, we will be using the following definition. Co-crystals are defined as crystalline multi-component materials comprised of at least two neutral molecules, an API and a co-former which are both solids under ambient conditions and which are held together via non-covalent interactions.[65]

There are various techniques utilised in the preparation of multi-component materials including slurry conversion, neat and liquid-assisted grinding (NG and LAG, respectively), solution crystallisation (*i.e.* cooling and evaporation), growth from the melt and spray drying.[66-67] Slow solvent evaporation is normally the preparation method of choice, but mechanical grinding of molecular materials has emerged as a more effective and direct approach to the formation of molecular and ionic co-crystals.[68] Each of these techniques will be discussed in Section 1.3.

1.3 Crystallisation Techniques

1.3.1 Solution Crystallisation

Crystallisation is an important purification and separation process in the pharmaceutical industry.[69] In solution crystallisation, the process requires the solution to be supersaturated for nucleation and crystal growth to commence.[70] In the pharmaceutical, agrochemicals and fine chemicals industry, the crystal product qualities, *e.g.* purity, morphology and crystal size distribution are highly influenced by the crystallisation process conditions.[71] The driving force for nucleation is the solute's change in chemical potential, $\Delta\mu$, as a consequence of the phase transformation as the supersaturation, S, which is defined as the ratio of solute concentration, C, to its solubility, C_{eq}, expressed using the following equation.[72]

$$S = \frac{C}{C_{eq}} \qquad \text{Equation 1.2}$$

Nucleation is the formation of entities of a new phase from a parent phase whereby a species new particles dissolved in solution form from its homogeneous solution after the generation of supersaturation which can be divided into primary and secondary nucleation.[73-74] Primary nucleation takes place by mechanisms not requiring the presence of crystalline matter in solution with the formation of primary nuclei occurring spontaneously at random sites in the bulk solution, *i.e.* homogeneous nucleation or heterogeneous nucleation taking place at solid surfaces that act as centres for crystallisation both occurring at high degrees of supersaturation. Secondary nucleation takes place in the presence of parent crystals of the solute and due to the reduced energy that is needed for secondary nucleation, it can occur at lower levels of supersaturation compared to primary nucleation.[75]

Solution crystallisation techniques can be classified according to the way in which supersaturation is generated, *i.e.* evaporative, reactive, cooling and antisolvent crystallisation.[76] In evaporative crystallisation (Figure 1.5a), the solution is initially undersaturated and through evaporation of solvent, supersaturation is generated. In cooling crystallisation (Figure 1.5b), a decrease in temperature results in a solubility decrease which induces supersaturation which in turn is reduced further by the growth of crystals. Cooling crystallisation is often utilised when the solubility shows a strong positive temperature dependence. Antisolvent crystallisation is another method for generating supersaturation. In antisolvent crystallisation (Figure 1.5c), supersaturation is generated by addition of a suitable antisolvent (*i.e.* solvent/antisolvent are both miscible) which lowers the concentration and also dilutes the mixture.[77-78]

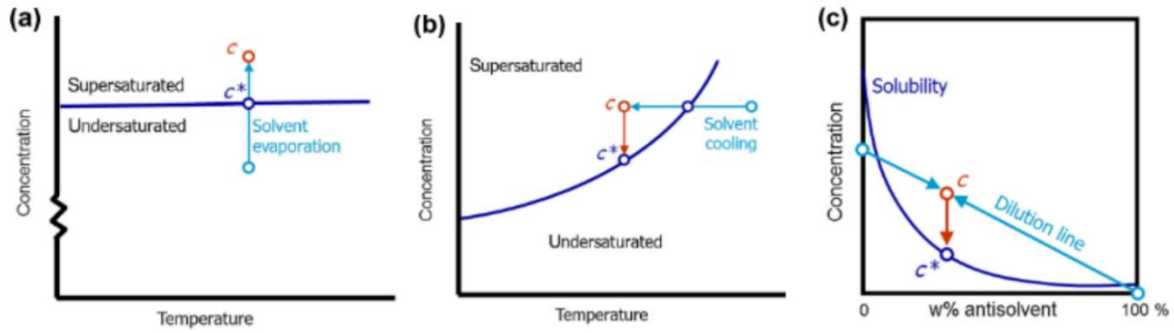

Figure 1.5: Schematic showing the methods of reaching supersaturation for different solution based crystallisation techniques a) evaporative crystallisation; b) cooling crystallisation and c) anti-solvent crystallisation. Adapted from (ter Horst, J. H., Schmidt, C. & Ulrich, J. Fundamentals of Industrial Crystallization. Handbook of Crystal Growth: Bulk Crystal Growth: Second Edition *(2014).*

The commonly used methods of preparing co-crystals include spray drying, solution crystallisation and grinding with the spray drying/grinding approaches being difficult to apply on an industrial scale making solution crystallisation the preferred method. The use of ternary phase diagrams can be used as a guide for selecting a suitable synthetic method/solvent for co-crystal formation as well as determining the screening combinations at which the thermodynamically stable co-crystals are expected to crystallise is valuable information to obtain prior to experiments and can be obtained from thermodynamic phase diagrams.[79-80] Ternary phase diagrams can be utilised to obtain pure co-crystals, avoiding solvates, other solid forms or even co-precipitation of pure reactants.[81] Ternary phase diagrams can describe a desired co-crystal's thermodynamically stable regions depending on the solubilities of the components in a given solvent system. Similar solubilities between the two components have been shown to result in a congruent system with a larger solubility difference likely resulting in an incongruent system indicating the importance of the components solubilities on the position/size of the co-crystal's thermodynamically stable region.[82]

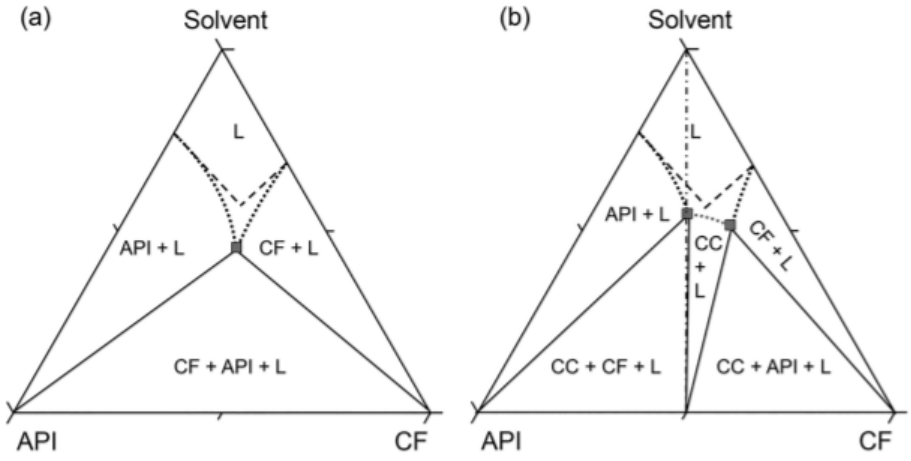

Figure 1.6: Schematic representation of a phase diagram for API, co-former and solvent compositions with no co-crystal formation in a) and with co-crystal formation in b). Adapted from Veith, H., Schleinitz, M., Schauerte, C. & Sadowski, G. Thermodynamic Approach for Co-crystal Screening. Cryst. Growth & Des. ***19****, 3253–3264 (2019).*

1.3.2 Solid State Grinding

In mechanochemical processes, the required energy for the activation of chemical reactions is normally provided by mechanical force and mechanochemical reactions depend on the direct absorption of mechanical energy from reagents, typically solids during the milling process.[83-84] In comparison to manual grinding which is open to the environment, ball milling has the advantage of offering an enclosed solvent-free reaction environment featuring well-defined parameters for optimising the reactivity including medium to sample ratio and frequency, *etc.* Amongst the different types of mills, planetary and shaker mills are the most common. Shaker mills involve the jars moving back and forth with a frequency that determines the intensity of the milling and are commonly used in the screening of pharmaceutical solids. Planetary mills, on the other hand, involve rotating the milling jar around a central axis, whilst spinning around its own axis. This "planetary" motion creates centrifugal forces recreating the effect of gravity on industrial scale roller mills offering a direct route to scale up. Milling jars/balls are usually made of stainless steel, zirconia, polytetrafluoroethylene (Teflon) or tungsten carbide, but poly(methyl)acrylate (PMMA) can also be used for *in situ* monitoring. Stainless steel is the most commonly used material for milling, however, metal contamination can result from lengthy milling with zirconia being a suitable alternative as both materials have similar densities.[85]

Mechanochemical techniques including liquid-assisted grinding (LAG) and polymer assisted grinding (POLAG) have become of great interest in API synthesis as well as solid form discovery due to their short reaction times as well as overcoming issues with thermal degradation/solubility typically encountered with solution based techniques.[86] The simplest type of mechanochemical reaction is that known as neat grinding (NG) or co-grinding with the reaction outcome depending solely on the reaction conditions, *e.g.* mode of treatment and mechanical activator. Liquid-assisted grinding (LAG) which features the addition of catalytic amounts of solvent allows for better control over the solid form obtained through varying the chemical nature and quantity of the liquid, however, although the quantity of liquid added may be minimal, this is still sufficient to promote solvate formation. POLAG avoids solvate formation and controls the polymorph obtained through controlling the microenvironment polarity through the use of different polymers.[87] A salt-assisted mechanochemical technique using sodium chloride has been shown to be a simple and cost effective approach in the preparation of porous metal-organic frameworks (MOFs).[88] Ion liquid-assisted grinding (iLAG) has recently emerged as a new type of LAG concept featuring the addition of a liquid and salt which has been shown to result in dissolution of the solid reagents leading to a homogeneous reaction mixture resulting in an improved efficiency of the milling process.[84] LAG using ionic liquids termed as ionic liquid-assisted grinding (ILAG) has been successful in the isolation

of co-crystals using imidazolium based ionic liquids and has demonstrated the ability to control polymorph through the use of ILAG. The use of ionic liquids in mechanochemistry allows for a promising alternative to conventional LAG as many properties of conventional LAG can be systematically tuned which allows for more tuning compared with polymers/organic solvents.[89] Many factors are known to affect the outcome of mechanochemical reactions including the milling temperature[90], addition of seeds[91], addition of liquid additives[92] and ball to powder ratio.[93]

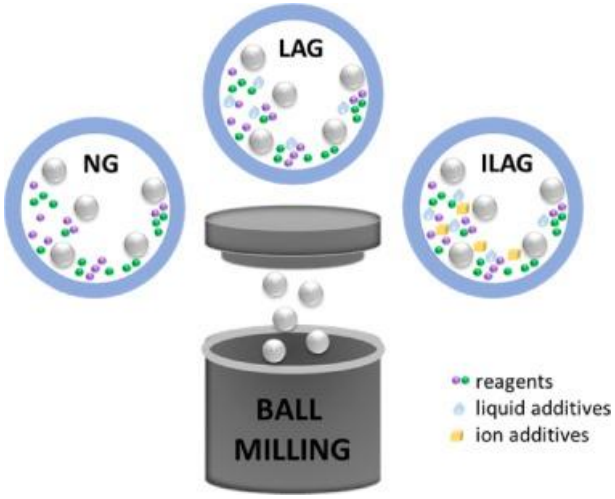

Figure 1.7: Schematic representation of the various mechanochemical reaction types including neat grinding (NG), liquid-assisted grinding (LAG) and ion liquid-assisted grinding (ILAG). Adapted from Głowniak, S., Szczęśniak, B., Choma, J. & Jaroniec, M. Mechanochemistry: Toward green synthesis of metal–organic frameworks. Mater. Today ***46****, 109–124 (2021).*

The monitoring of mechanochemical reactions *in situ* has been explored in recent years by Uzarevic and co-workers using synchrotron X-ray powder diffraction to monitor the formation of zeolitic imidazolate frameworks (ZIFs) in real time which indicated the effect of varying the amount of liquid additive on the reaction outcome.[94] Kulla and co-workers investigated ternary co-crystal formation between isonicotinamide and glutaric acid through *in situ* ball milling which signified the importance of milling parameters to yield the pure ternary phase, *i.e.* frequency as well as catalytic quantities of solvent used on the reaction outcome.[95] Other related *in situ* studies include utilising variable temperature synchrotron X-ray powder diffraction to investigate the effects of temperature on mechanochemical reactions[96] and monitoring pharmaceutical co-crystal formation in real time using resonance acoustic mixing (RAM).[97]

1.3.3 Spray Drying

Typical co-crystallisation methods include slurry conversion, solution crystallisation and grinding are employed in the rapid screening of APIs, however, these techniques present challenges scaling up.[98] Advanced co-crystallisation techniques include twin screw[99], ultrasound assisted[100] and supercritical fluid[101] are more suitable for scale up, but with some optimisation. Spray drying is a preferred technique for particle engineering of pharmaceuticals since it is continuous, fast and a one-step process which involves converting an emulsion, suspension or solution into a fine/dry powder in a single step through passing atomised spray through a high temperature gas-medium.[98,20]

The preparation of co-crystals using spray drying has emerged as a viable option when conventional methods, *e.g.* solution crystallisation or milling are unsuccessful and this approach produces a consistent quality which can be manufactured continuously with a high product efficiency.[102]

1.4 Structure of Human Hair

Human hair consists of approximately 65-95% protein by weight and greater than 15% water, lipid pigments and other components. The hair thread is a cylindrical structure that is highly ordered, produced mostly from keratinised inert cells that follow a design that is very precise and pre-defined. α-Keratin is responsible for giving the hair durability, flexibility, strength and functionality and is also a laminated complex that is formed from different structures. α-Keratin is responsible for the formation of around 80% of human hair with a high sulphur grade coming from cysteine.[103] Hair fibres are keratinised constructs which can vary along its length in shape, size and in the arrangement of their component structures. A hair fibre is organised into three layers: the cortex, the cuticle and the medulla.

The cortex (Figure 1.8) is comprised of cortical cells which are approximately 100 μm in length with a thickness of 1-6 μm. These cortical cells are made up of sub-components known as macrofibrils which feature a diameter of approximately 0.1-0.4 μm. These macrofibrils are composed of intermediate filaments (IFs) at the nanometer scale which are embedded within a matrix featuring a high-sulphide content. A single IF has a diameter of approximately 7.5 nm and is formed from eight protofilaments with each one being composed of four right-handed α-helix chains.[104]

Cuticle cells are formed by amorphous material with each one being divided into four sub-units which have a distinct chemical composition. The outermost layer of the cuticle cell is known as the epicuticle (layer 1) which is hydrophobic, thin (≈2.5 nm) and rich in cysteine (≈12% w/w). The A-layer (layer 2) and the exocuticle (layer 3) are more hydrophobic and reticulated because the cysteine content is greater (≈30% w/w and ≈15% w/w respectively). The most internal layer (layer 4) is known as the endocuticle which is comprised of non-keratinous material (3% w/w cysteine) and is also hydrophilic. The cell membrane complex (CMC) is part of the cuticle structure which has an adhesive function of binding the cuticle cells together. The CMC is comprised of a central δ-layer which is hydrophobic (≈15 nm) and is produced mainly by polysaccharides and proteins sandwiched by two lipid layers (≈5 nm) each known as β-layers. These β-layers are known as monolayer lipids which are attached through covalent bonds to the keratin in the epicuticle and through Van der Waals attractive forces to the δ-layer on the fatty acids hydrophobic end. There are two β-layers: the inner β-layer facing the inner section of an individual cuticle cell which is formed mostly from stearic, palmitic and oleic fatty acids. The second β-layer is known as the outer β-layer which faces the cuticle's outside surface closer to the adjacent cuticle containing 18-methyleicosanoic acid (18-MEA) as the main component.[105] In human hair, the medulla is usually found only in terminal hair and can be continuous, discontinuous or absent.[106]

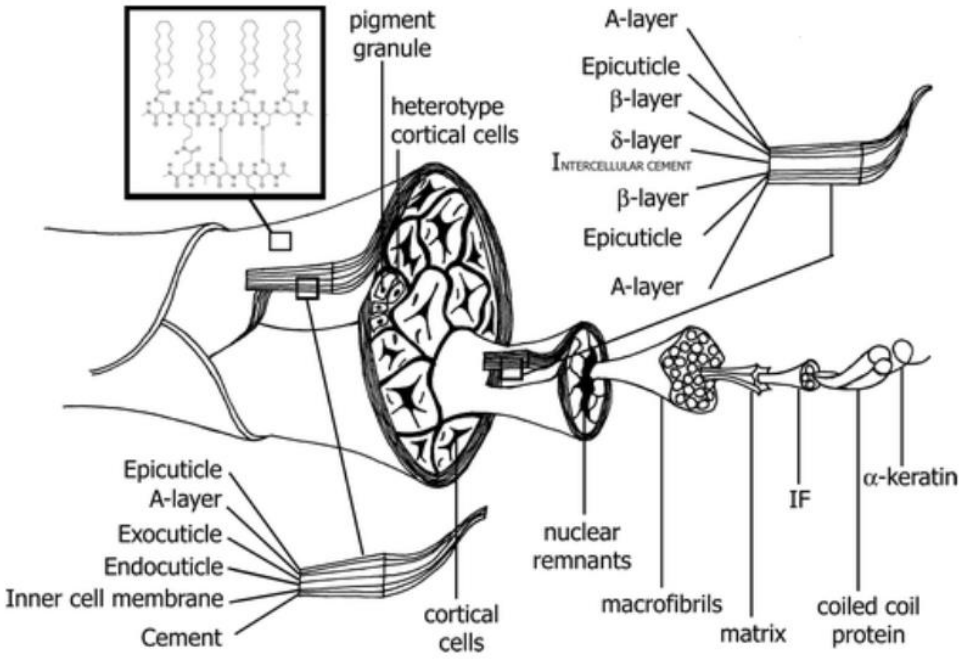

Figure 1.8: The structure of human hair. Adapted from Morel, O. J. X. & Christie, R. M. Current Trends in the Chemistry of Permanent Hair Dyeing. Chem. Rev. 111, 2537-2561 (2011).

1.4.1 Colouration of Human Hair

An individual's natural hair colour commonly reflects their ethnic origin or geographical location. Hair is frequently coloured with synthetic dyes as a fashion statement or to enhance their appearance.[107] Hair dyes can be classified into several categories based on their origin: metallic hair dyes, vegetable hair dyes and synthetic hair dyes which can be further sub-divided into temporary, semi-permanent, demi-permanent and permanent (*i.e.* oxidative hair dyes). Vegetable hair dyes are non-toxic, alter the colour hue and last only a short period of time. Temporary and semi-permanent hair dyes feature coloured molecules in which some may penetrate into the cortex in the case of semi-permanent dyes and in temporary hair dyes, these molecules can be deposited in the cuticle's. In demi-permanent and oxidative hair dyes, the shade is developed through interactions between an oxidising agent and colour precursors and the diffusion of the molecules into the cortex.[108-109]

Oxidative hair dyes contain several different components including coupling agents, a developer and primary intermediates which react with each other to produce the desired colour.[110] Hair dyes are comprised of two parts: a precursor/coupler part and the developer part. In the dye formulation, the primary intermediates (*e.g. p*-phenylenediamine or 1,3-diaminobenzene) are slowly oxidised followed by the reaction with the colouring couplers (*e.g.* resorcinol or *m*-aminophenol). The precursor/coupler part consists of reducing agents, alkalising agents, couplers and primary intermediates. The alkalising agents (*e.g.* monoethanolamine (MEA) or ammonia) neutralise the colouring intermediates and swell the cuticle facilitating penetration of the colour pigments into the

hair. The reducing agents stop the premature oxidation of colouring intermediates, thus stabilising the hair dye until required. The developer part of the hair dyes consists of an oxidant: most commonly hydrogen peroxide (H_2O_2) which oxidises the primary colouring intermediates forming quinonediimine intermediates which subsequently react with the colouring couplers to produce large di-nuclear, tri-nuclear or polymeric structures that get entrapped inside the hair shaft.[111]

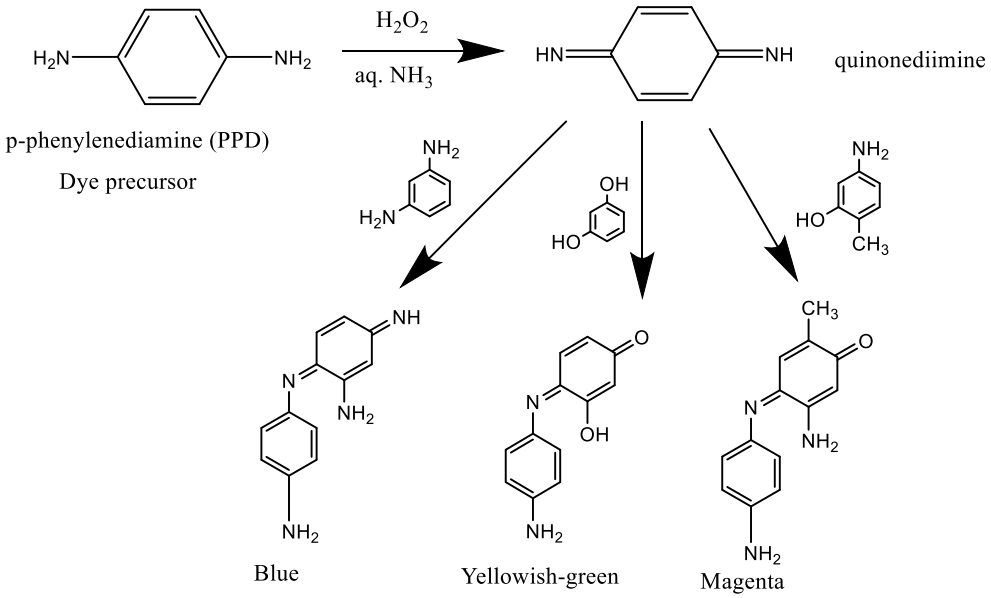

Figure 1.9: Schematic showing the typical reaction scheme of oxidative hair dyes (OHD's). Adapted from Delori, A., Urquhart, A. J. & Oswald, I. D. H. Supramolecular hair dyes: A new application of cocrystallization. CrystEngComm 18, 5360-5364 (2016).

Co-crystallisation presents an opportunity to modify the physical and chemical properties of a material as discussed in Section 1.2.4 and in this thesis co-crystallisation presents an opportunity to develop multi-component forms (*i.e.* salts and co-crystals) of wide ranging colours that could be used to colour hair. The hope is that through changing the co-formers utilised in co-crystallisation reactions that this will allow us to access a wide array of colours.

1.5 Thesis Outline

The main goal of this research is to build on the limited previous work conducted on supramolecular hair dyes exploring the reasons behind the deep coloured nature of the salts of PPD. We have sought to identify possible safer alternatives to PPD, that are still capable of colouring hair as well as expanding the range of available colours.

The main body of this thesis is divided into three experiments: firstly, exploring the reactivity of PPD in solution through the use of spectroscopic and chromatographic techniques as the colour of a PPD solution is shown to change over time. This work will not only investigate the solution reactivity of PPD as well as investigate whether the formation of salts of PPD will help to stabilise PPD. Secondly, the effect of small structural changes to PPD through the use of OPD and MPD will be investigated as well as the effect of ionisation through the formation of ionic co-crystals. Co-crystallisation of OPD and MPD will be attempted using the same co-formers as with PPD to investigate not only the impact of the colour on the materials formed as well as on the reactivity in solution. Finally, alizarin will be explored for the possibility of creating new multi-component materials that will hopefully provide a safer alternative to PPD whilst increasing the range of colours and the hair dyeing ability will be investigated of any new forms.

1.6 References

1. Cinčić, D., Brekalo, I. & Kaitner, B. Solvent-free polymorphism control in a covalent mechanochemical reaction. *Cryst. Growth Des.* **12**, 44–48 (2012).

2. Singh, A., Lee, I. S. & Myerson, A. S. Concomitant crystallization of ROY on patterned substrates: Using a high throughput method to improve the chances of crystallization of different polymorphs. *Cryst. Growth Des.* **9**, 1182–1185 (2009).

3. Censi, R. & Di Martino, P. Polymorph impact on the bioavailability and stability of poorly soluble drugs. *Molecules* **20**, 18759–18776 (2015).

4. Andrews, J. L., Nilsson Lill, S. O., Freitag Pohl, S., Apperley, D. C., Yufit, D. S., Batsanov, A. S., Mulvee, M. T., Edkins, K., McCabe, J. F., Berry, D. J., Probert, M. R & Steed, J. W. Derisking the Polymorph Landscape: The Complex Polymorphism of Mexiletine Hydrochloride. *Cryst. Growth Des.* **21**, 7150–7167 (2021).

5. Gentili, D., Gazzano, M., Melucci, M., Jones, D. & Cavallini, M. Polymorphism as an additional functionality of materials for technological applications at surfaces and interfaces. *Chem. Soc. Rev.* **48**, 2502–2517 (2019).

6. Fabbiani, F. P. A., Allan, D. R., Parsons, S. & Pulham, C. R. An exploration of the polymorphism of piracetam using high pressure. *CrystEngComm* **7**, 179–186 (2005).

7. Prusiner, P. & Sundaralingam, M. The crystal and molecular structures of two polymorphic crystalline forms of virazole (1-*β*- D -ribofuranosyl-1,2,4-triazole-3-carboxamide). A new synthetic broad sprectrum antiviral agent. *Acta Crystallogr. Sect. B Struct. Crystallogr. Cryst. Chem.* **32**, 419–426 (1976).

8. Vishweshwar, P., McMahon, J. A., Oliveira, M., Peterson, M. L. & Zaworotko, M. J. The predictably elusive form II of aspirin. *J. Am. Chem. Soc.* **127**, 16802–16803 (2005).

9. Akune, Y., Gontani, H., Hirosawa, R., Koseki, A. & Matsumoto, S. The effects of molecular flexibility and substituents on conformational polymorphism in a series of 2,5-diamino-3,6-dicyanopyrazine dyes with highly flexible groups. *CrystEngComm* **17**, 5789–5800 (2015).

10. Lévesque, A., Maris, T. & D. Wuest, J. ROY Reclaims Its Crown: New Ways To Increase Polymorphic Diversity. *J. Am. Chem. Soc.* **142**, 11873–11883 (2020).

11. Tan, M., Shtukenberg, A.G., Zhu, S., Xu, W., Dooryhee, E., Nichols, S. M., Ward, M. D., Kahr, B & Zhu, Q. ROY revisited, again: the eighth solved structure. *Faraday Discuss.* **211**, 477–491

(2018).

12. Zeidan, T. A., Trotta, J. T., Tilak, P. A., Oliveira, M. A., Chiarella, R. A., Foxman, B. M., Almarsson, Ö & Hickey, M. B. An unprecedented case of dodecamorphism: The twelfth polymorph of aripiprazole formed by seeding with its active metabolite. *CrystEngComm* **18**, 1486–1488 (2016).

13. López-Mejías, V., Kampf, J. W. & Matzger, A. J. Nonamorphism in flufenamic acid and a new record for a polymorphic compound with solved structures. *J. Am. Chem. Soc.* **134**, 9872–9875 (2012).

14. Bhardwaj, R. M., McMahon, J. A., Nyman, J., Price, L. S., Konar, S., Oswald, I. D. H., Pulham, C. R., Price, S. L & Reutzel-Edens, S. M. A Prolific Solvate Former, Galunisertib, under the Pressure of Crystal Structure Prediction, Produces Ten Diverse Polymorphs. *J. Am. Chem. Soc.* **141**, 13887–13897 (2019).

15. Bis, J. A., Vishweshwar, P., Middleton, R. A. & Zaworotko, M. J. Concomitant and conformational polymorphism, conformational isomorphism, and phase relationships in 4-cyanopyridine·4,4'-biphenol cocrystals. *Cryst. Growth Des.* **6**, 1048–1053 (2006).

16. Brog, J. P., Chanez, C. L., Crochet, A. & Fromm, K. M. Polymorphism, what it is and how to identify it: A systematic review. *RSC Advances* **3**, 16905–16931 (2013).

17. Tang, W., Sima, A. D., Gong, J., Wang, J. & Li, T. Kinetic Difference between Concomitant Polymorphism and Solvent-Mediated Phase Transformation: A Case of Tolfenamic Acid. *Cryst. Growth Des.* **20**, 1779–1788 (2020).

18. Nishio, K. & Lu, A. K. A. Can every substance exist as an amorphous solid? *J. Non. Cryst. Solids* **576**, 121254 (2022).

19. Shah, B., Kakumanu, V. K. & Bansal, A. K. Analytical techniques for quantification of amorphous/crystalline phases in pharmaceutical solids. *J. Pharm. Sci.* **95**, 1641–1665 (2006).

20. Wang, B., Liu, F., Xiang, J., He, Y., Zhang, Z., Cheng, Z., Liu, W & Tan, S. A critical review of spray-dried amorphous pharmaceuticals: Synthesis, analysis and application. *Int. J. Pharm.* **594**, 120165 (2021).

21. Babu, N. J. & Nangia, A. Solubility advantage of amorphous drugs and pharmaceutical cocrystals. *Cryst. Growth Des.* **11**, 2662–2679 (2011).

22. Fan, W., Zhu, W., Zhang, X., Xu, Y. & Di, L. Application of the combination of ball-milling and

hot-melt extrusion in the development of an amorphous solid dispersion of a poorly water-soluble drug with high melting point. *RSC Adv.* **9**, 22263–22273 (2019).

23. Mizoguchi, R., Waraya, H. & Hirakura, Y. Application of Co-Amorphous Technology for Improving the Physicochemical Properties of Amorphous Formulations. *Mol. Pharm.* **16**, 2142–2152 (2019).

24. Samipillai, M., Mirmehrabi, M. & Rohani, S. Co-amorphous solids of dasatinib and olanzapine by saccharin with promising physicochemical properties. *J. Drug Deliv. Sci. Technol.* **66**, 102800 (2021).

25. Silva, J. F. C., Rosado, M. T. S. & Eusébio, M. E. S. Structure and energetics of intermolecular association in two lurasidone co-amorphous drug systems. *J. Mol. Struct.* **1242**, 130709 (2021).

26. Desiraju, G. R. Crystal engineering: From molecule to crystal. *J. Am. Chem. Soc.* **135**, 9952–9967 (2013).

27. Khan, M., Enkelmann, V. & Brunklaus, G. O−H ⋯ N heterosynthon: A robust supramolecular unit for crystal engineering. *Cryst. Growth Des.* **9**, 2354–2362 (2009).

28. Mukherjee, A. Building upon supramolecular synthons: Some aspects of crystal engineering. *Cryst. Growth Des.* **15**, 3076–3085 (2015).

29. Wang, Z., Flores, Q., Guo, H., Trevizo, R., Zhang, X & Wang, S. Crystal engineering construction of caffeic acid derivatives with potential applications in pharmaceuticals and degradable polymeric materials. *CrystEngComm* **22**, 7847–7857 (2020).

30. Long, S., Zhou, P., Parkin, S. & Li, T. From competition to commensuration by two major hydrogen-bonding motifs. *Cryst. Growth Des.* **14**, 27–31 (2014).

31. Desiraju, G. R. Supramolecular Synthons in Crystal Engineering—A New Organic Synthesis. *Angewandte Chemie* **34**, 2311–2327 (1995).

32. Saha, S., Rajput, L., Joseph, S., Mishra, M. K., Ganguly, S & Desiraju, G. R. IR spectroscopy as a probe for C−H···X hydrogen bonded supramolecular synthons. *CrystEngComm* **17**, 1273–1290 (2015).

33. Adalder, T. K., Sankolli, R. & Dastidar, P. Homo- or heterosynthon? A crystallographic study on a series of new cocrystals derived from pyrazinecarboxamide and various carboxylic acids equipped with additional hydrogen bonding sites. *Cryst. Growth Des.* **12**, 2533–2542 (2012).

34. Mukherjee, A., Tothadi, S., Chakraborty, S., Ganguly, S. & Desiraju, G. R. Synthon identification in co-crystals and polymorphs with IR spectroscopy. Primary amides as a case study. *CrystEngComm* **15**, 4640–4654 (2013).

35. Lemmerer, A., Bernstein, J. & Kahlenberg, V. One-pot covalent and supramolecular synthesis of pharmaceutical co-crystals using the API isoniazid: A potential supramolecular reagent. *CrystEngComm* **12**, 2856–2864 (2010).

36. Shattock, T. R., Arora, K. K., Vishweshwar, P. & Zaworotko, M. J. Hierarchy of supramolecular synthons: Persistent carboxylic acid···pyridine hydrogen bonds in cocrystals that also contain a hydroxyl moiety. *Cryst. Growth and Des* **8**, 4533–4545 (2008).

37. Hemamalini, M., Loh, W. S., Quah, C. K. & Fun, H. K. Investigation of supramolecular synthons and structural characterisation of aminopyridine-carboxylic acid derivatives. *Chem. Cent. J.* **8**, (2014).

38. Desiraju, G. R., Vittal, J. J. & Ramanan, A. Crystal Engineering A Textbook. 1–23 (2011).

39. Etter, M. C., MacDonald, J. C. & Bernstein, J. Graph-set analysis of hydrogen-bond patterns in organic crystals. *Acta Crystallogr. Sect. B* **46**, 256–262 (1990).

40. Bernstein, J., Davis, R. E., Shimoni, L. & Chang, N. L. Patterns in Hydrogen Bonding: Functionality and Graph Set Analysis in Crystals. *Angewandte Chemie* 1555–1573 (1995).

41. Riley, K. E. & Hobza, P. The relative roles of electrostatics and dispersion in the stabilization of halogen bonds. *Phys. Chem. Chem. Phys.* **15**, 17742–17751 (2013).

42. Berger, G., Soubhye, J. & Meyer, F. Halogen bonding in polymer science: From crystal engineering to functional supramolecular polymers and materials. *Polym. Chem* 3559–3580 (2015).

43. Pancholi, J. & Beer, P. D. Halogen bonding motifs for anion recognition. *Coord. Chem. Rev.* **416**, 213281 (2020).

44. Turunen, L. & Erdélyi, M. Halogen bonds of halonium ions. *Chem. Soc. Rev.* **49**, 2688–2700 (2020).

45. Dichiarante, V., Kaiho, T., Metrangolo, P., Pilati, T., Resnati, G., Terraneo, G & Ursini, M. The diiodomethyl-sulfonyl moiety: An unexplored halogen bond-donor motif. *Chem. Commun.* **55**, 4234–4237 (2019).

46. Gilday, L. C., Robinson, S. W., Barendt, T. A., Langton, M. J., Mullaney, B. R & Beer, P. D.

Halogen Bonding in Supramolecular Chemistry. *Chem. Rev.* **115**, 7118–7195 (2015).

47. Zheng, J., Suwardi, A., Wong, C. J. E., Loh, X. J. & Li, Z. Halogen bonding regulated functional nanomaterials. *Nanoscale Adv.* **3**, 6342–6357 (2021).

48. Lisac, K. & Cinčić, D. Simple design for metal-based halogen-bonded cocrystals utilizing the MCl···I motif. *CrystEngComm* **20**, 5955–5963 (2018).

49. Timothy Clark, Matthias Hennemann, J. S. M. & P. P. Halogen bonding: the *σ*-hole. *J. Mol. Model.* **13**, 291–296 (2006).

50. Lim, J. Y. C. & Beer, P. D. Sigma-Hole Interactions in Anion Recognition. *Chem* **4**, 731–783 (2018).

51. Politzer, P., Murray, J. S. & Clark, T. Halogen bonding and other *σ*-hole interactions: a perspective. *Chem. Phys.* ***15****, 11178-11189* (2013).

52. Wang, H., Wang, W. & Jin, W. J. *σ*-Hole Bond vs *π*-Hole Bond: A Comparison Based on Halogen Bond. *Chem. Rev.* **116**, 5072–5104 (2016).

53. Chen, T., Li, M. & Liu, J. *π*-*π* Stacking Interaction: A Nondestructive and Facile Means in Material Engineering for Bioapplications. *Cryst. Growth Des.* **18**, 2765–2783 (2018).

54. Zhao, Y., Li, J., Gu, H., Wei, D., Xu, Y. C., Fu, W & Yu, Z. Conformational Preferences of *π*–*π* Stacking Between Ligand and Protein, Analysis Derived from Crystal Structure Data Geometric Preference of *π*–*π* Interaction. *Interdiscip. Sci. Comput. Life Sci.* **7**, 211–220 (2015).

55. Thakuria, R., Nath, N. K. & Saha, B. K. The Nature and Applications of *π*-*π* Interactions: A Perspective. *Cryst. Growth and Des* **19**, 523–528 (2019).

56. Mignon, P., Loverix, S., Steyaert, J. & Geerlings, P. Influence of the *π*-*π* interaction on the hydrogen bonding capacity of stacked DNA/RNA bases. *Nucleic Acids Research* **33**, 1779–1789 (2005).

57. Reillyab, A. M. & Tkatchenko. A. Van der Waals dispersion interactions in molecular materials: Beyond pairwise additivity. *Chem. Sci* ***6****, 3289-3301* (2015).

58. Moondra, S., Maheshwari, R., Taneja, N., Tekade, M. & Tekadle, R. K. Bulk Level Properties and its Role in Formulation Development and Processing. *Dosage Form Design Parameters* **2**, 221–256 (Elsevier, 2018).

59. Dai, X. L., Chen, J. M. & Lu, T. B. Pharmaceutical cocrystallization: An effective approach to

modulate the physicochemical properties of solid-state drugs. *CrystEngComm* **20**, 5292–5316 (2018).

60. Tabassum, N., Varras, P. C., Arshad, F., Choudhary, M. I. & Yousuf, S. Biological activity tuning of antibacterial urotropine: Via co-crystallization: Synthesis, biological activity evaluation and computational insight. *CrystEngComm* **22**, 3439–3450 (2020).

61. Shemchuk, O., Braga, D., Grepioni, F. & Turner, R. J. Co-crystallization of antibacterials with inorganic salts: Paving the way to activity enhancement. *RSC Adv.* **10**, 2146–2149 (2020).

62. Aitipamula, S., Chow, P. S. & Tan, R. B. H. Solvates and polymorphic phase transformations of 2-chloro-4-nitrobenzoic acid. *CrystEngComm* **13**, 1037–1045 (2011).

63. Childs, S. L., Stahly, G. P. & Park, A. The salt-cocrystal continuum: The influence of crystal structure on ionization state. *Mol. Pharm.* **4**, 323–338 (2007).

64. Cruz-Cabeza, A. J. Acid–base crystalline complexes and the p*K*a rule. *CrystEngComm* **14**, 6362–6265 (2012).

65. Sowa, M., Slepokura, K. & Matczak-Jon, E. Improving solubility of fisetin by cocrystallization. *CrystEngComm* **16**, 10592–10601 (2014).

66. Zhao, L., Raval, V., Briggs, N. E. B., Bhardwaj, R. M., McGlone, T., Oswald, I. D. H. & Florence, A. J. From discovery to scale-up: *α*-lipoic acid: Nicotinamide co-crystals in a continuous oscillatory baffled crystalliser. *CrystEngComm* **16**, 5769–5780 (2014).

67. Lee, H. L. & Lee, T. Direct co-crystal assembly from synthesis to co-crystallization. *CrystEngComm* **17**, 9002–9006 (2015).

68. Braga, D., Maini, L. & Grepioni, F. Mechanochemical preparation of co-crystals. *Chem. Soc. Rev.* **42**, 7638–7648 (2013).

69. Devos, C., Van Gerven, T. & Kuhn, S. A Review of Experimental Methods for Nucleation Rate Determination in Large-Volume Batch and Microfluidic Crystallization. *Cryst. Growth Des.* **21**, 2541–2565 (2021).

70. Ramakers, L. A. I., McGinty, J., Beckmann, W., Levilain, G., Lee, M., Wheatcroft, H., Houson, I & Sefcik, J. Investigation of Metastable Zones and Induction Times in Glycine Crystallization across Three Different Antisolvents. *Cryst. Growth Des.* **20**, 4935–4944 (2020).

71. Kadam, S. S., Kramer, H. J. M. & Ter Horst, J. H. Combination of a single primary nucleation event and secondary nucleation in crystallization processes. *Cryst. Growth Des.* **11**, 1271–

1277 (2011).

72. Bhamidi, V., Kenis, P. J. A. & Zukoski, C. F. Probability of Nucleation in a Metastable Zone: Induction Supersaturation and Implications. *Cryst. Growth Des.* **17**, 1132–1145 (2017).

73. Maria Maggioni, G. & Mazzotti, M. Stochasticity in Primary Nucleation: Measuring and Modeling Detection Times. *Cryst. Growth Des. Des.* **17**, 3625–3635 (2017).

74. Pino-García, O. & Rasmuson, Å. C. Primary nucleation of vanillin explored by a novel multicell device. *Ind. Eng. Chem. Res.* **42**, 4899–4909 (2003).

75. Xu, S., Wang, Y., Hou, Z. & Chuai, X. Overview of secondary nucleation: From fundamentals to application. *Ind. Eng. Chem. Res.* **59**, 18335–18356 (2020).

76. Brown, C. J., McGlone, T., Yerdelen, S., Srirambhatla, V., Mabbott, F., Gurung, R., Briuglia, M. L., Ahmed, B., Polyzois, H., McGinty, J., Perciballi, F., Fysikopoulos, D., MacFhionnghaile, P., Siddique, H., Raval, V., Harrington, T. S., Vassileiou, A. D., Robertson, M., Prasad, E., Johnston, A., Johnston, B., Nordon, A., Srai, J. S., Halbert, G., ter Horst, J. H., Price, C. J., Reilly, C. D., Sefcik, J. & Florence, A. J. Enabling precision manufacturing of active pharmaceutical ingredients: workflow for seeded cooling continuous crystallisations. *Mol. Syst. Des. Eng.* **3**, 518–549 (2018).

77. ter Horst, J. H., Schmidt, C. & Ulrich, J. Fundamentals of Industrial Crystallization. *Handbook of Crystal Growth: Bulk Crystal Growth: Second Edition* 1317–1349 (2014).

78. Zhang, X.-X., Yang, Z.-J., Nie, F. & Yan, Q. L. Recent advances on the crystallization engineering of energetic materials. *Energ. Mater. Front.* **1**, 141–156 (2020).

79. Jia, Q., Wang, J., Zhang, S., Zhang, J., Liu, N. & Kou, K. Investigation of the solid-liquid ternary phase diagrams of 2HNIW·HMX cocrystal. *RSC Adv.* **11**, 9542–9549 (2021).

80. Veith, H., Schleinitz, M., Schauerte, C. & Sadowski, G. Thermodynamic Approach for Co-crystal Screening. *Cryst. Growth Des.* **19**, 3253–3264 (2019).

81. Yang, J., Hong, B., Wang, N., Li, X., Huang, X., Bao, Y., Xie, C. & Hao, H. Thermodynamics and molecular mechanism of the formation of the cocrystals of: *p*-hydroxybenzoic acid and glutaric acid. *CrystEngComm* **21**, 6374–6381 (2019).

82. Jia, Q., Zhang, J., Zhang, S., Lei, D., Xu, Y and Kou, K. Investigation of the Phase Behavior of a HNIW·TNT Cocrystal System and Construction of Ternary Phase Diagrams. *Cryst. Growth Des.* **19**, 6370–6376 (2019).

83. Bazedi, G. A. A., Al-Rawajfeh, A. E., Abdel-Fatah, M. A., Alrbaihat, M. R. & AlShamaileh, E. Synthesis of nanomaterials by mechanochemistry. *Handb. Greener Synth. Nanomater. Compd.* 405–418 (2021).

84. Głowniak, S., Szczęśniak, B., Choma, J. & Jaroniec, M. Mechanochemistry: Toward green synthesis of metal–organic frameworks. *Mater. Today* **46**, 109–124 (2021).

85. Do, J.-L. & Friščić, T. Mechanochemistry: A Force of Synthesis. *ACS Cent. Sci.* **3**, 13–19 (2016).

86. Ayoub, G., Strukil, V., Fábián, L., Mottillo, C., Bao, H., Murata, Y., Moores, A., Margetić, D., Eckert-Maksic, M and Friščić, T. Mechanochemistry vs solution growth: striking differences in bench stability of a cimetidine salt based on a synthetic method. *CrystEngComm* (2018).

87. Hasa, D., Carlino, E. & Jones, W. Polymer-Assisted Grinding, a Versatile Method for Polymorph Control of Cocrystallization. *Cryst. Growth Des.* **16**, 1772–1779 (2016).

88. Yang, J., Feng, X., Lu, G., Li, Y., Mao, C., Wen, Z. & Yuan, W. NaCl as a solid solvent to assist the mechanochemical synthesis and post-synthesis of hierarchical porous MOFs with high I2 vapour uptake. *Dalt. Trans.* **47**, 5065–5071 (2018).

89. Mukherjee, A., Rogers, R. D. & Myerson, A. S. Cocrystal formation by ionic liquid-assisted grinding: case study with cocrystals of caffeine. *CrystEngComm* **20**, 3817–3821 (2018).

90. Drebushchak, T. N., Ogienko, A. A. & Boldyreva, E. V. 'Hedvall effect' in cryogrinding of molecular crystals. A case study of a polymorphic transition in chlorpropamide. *CrystEngComm* **13**, 4405–4410 (2011).

91. Fischer, F., Greiser, S., Pfeifer, D., Jager, C., Rademann, K. & Emmerling, F. Mechanochemically Induced Conversion of Crystalline Benzamide Polymorphs by Seeding. *Angew. Chem.* **55**, 14281–14285 (2016).

92. Bouvart, N., Palix, R. M., Arkhipov, S. G., Tumanov, I. A., Michalchuk, A. A. L. & Boldyreva, E. V. Polymorphism of chlorpropamide on liquid-assisted mechanical treatment: Choice of liquid and type of mechanical treatment matter. *CrystEngComm* **20**, 1797–1803 (2018).

93. Kamali, N., Gniado, K., McArdle, P. & Erxleben, A. Application of Ball Milling for Highly Selective Mechanochemical Polymorph Transformations. *Org. Process Res. Dev.* **22**, 796–802 (2018).

94. Užarević, K., Halasz, I. & Friščić, T. Real-Time and In Situ Monitoring of Mechanochemical Reactions: A New Playground for All Chemists. *J. Phys. Chem. Lett.* **6**, 4129–4140 (2015).

95. Kulla, H., Michalchuk, A. A. L. & Emmerling, F. Manipulating the dynamics of mechanochemical ternary cocrystal formation. *Chem. Commun.* **55**, 9793–9796 (2019).

96. Užarević, K., Štrukil, V., Mottillo, C., Julien, P. A., Puškarić, A., Friščić, T. & Halasz, I. Exploring the Effect of Temperature on a Mechanochemical Reaction by in Situ Synchrotron Powder X-ray Diffraction. *Cryst. Growth Des.* **16**, 2342–2347 (2016).

97. Michalchuk, A. A. L., Hope, K. S., Kennedy, S. R., Blanco, M. V., Boldyreva, E. V. & Pulham, C. R. Ball-free mechanochemistry:: In situ real-time monitoring of pharmaceutical co-crystal formation by resonant acoustic mixing. *Chem. Commun.* **54**, 4033–4036 (2018).

98. Patil, S. P., Modi, S. R. & Bansal, A. K. Generation of 1:1 Carbamazepine:Nicotinamide cocrystals by spray drying. *Eur. J. Pharm. Sci.* **62**, 251–257 (2014).

99. Medina, C., Daurio, D., Nagapudi, K. & Alvarez-Nunez, F. Manufacture of pharmaceutical co-crystals using twin screw extrusion: A solvent-less and scalable process. *J. Pharm. Sci.* **99**, 1693–1696 (2010).

100. Aher, S., Dhumal, R., Mahadik, K., Paradkar, A. & York, P. Ultrasound assisted cocrystallization from solution (USSC) containing a non-congruently soluble cocrystal component pair: Caffeine/maleic acid. *Eur. J. Pharm. Sci.* **41**, 597–602 (2010).

101. Padrela, L., Rodrigues, M. A., Velaga, S. P., Matos, H. A. & de Azevedo, E. G. Formation of indomethacin–saccharin cocrystals using supercritical fluid technology. *Eur. J. Pharm. Sci.* **38**, 9–17 (2009).

102. Weng, J., Wong, S. N., Xu, X., Xuan, B., Wang, C., Chen, R., Sun, C. C., Lakerveld, R., Kwok, P. C. L. & Chow, S. F. Cocrystal Engineering of Itraconazole with Suberic Acid via Rotary Evaporation and Spray Drying. *Cryst. Growth Des.* **19**, 2736–2745 (2019).

103. da Gama, R. M., Balogh, T. S., Franca, S., Sá Dias, T. C., Bedin, V., Baby, A. R., do Rosário Matos, J. & Velasco, M. V. R. Thermal analysis of hair treated with oxidative hair dye under influence of conditioners agents. *J. Therm. Anal. Calorim.* **106**, 399–405 (2011).

104. Yu, Y., Yang, W., Wang, B. & Meyers, M. A. Structure and mechanical behavior of human hair. *Mater. Sci. Eng. C-Materials Biol. Appl.* **73**, 152–163 (2017).

105. Richena, M. & Rezende, C. A. Morphological degradation of human hair cuticle due to simulated sunlight irradiation and washing. *J. Photochem. Photobiol. B-Biology* **161**, 430–440 (2016).

106. Dawber, R. Hair: its structure and response to cosmetic preparations. *Clin Dermatol* **14**, 105–112 (1996).

107. Morel, O. J. X. & Christie, R. M. Current Trends in the Chemistry of Permanent Hair Dyeing. *Chem. Rev.* **111**, 2537–2561 (2011).

108. Guerra-Tapia, A. & Gonzalez-Guerra, E. Hair cosmetics: dyes. *Actas Dermosifiliogr* **105**, 833–839 (2014).

109. Gonzalez, V., Wood, R., Lee, J., Taylor, S. & Bussemaker, M. J. Ultrasound-enhanced hair dye application for natural dyeing formulations. *Ultrason. Sonochem.* **52**, 294–304 (2019).

110. Park, H., Hwang, J., Han, J., Lee, B., Kim, Y., Joo, K., Choi, M., Cho, S., Kim, B. & Lim, K. Skin irritation and sensitization potential of oxidative hair dye substances evaluated with in vitro, in chemico and in silico test methods. *Food Chem. Toxicol.* **121**, 360–366 (2018).

111. Seo, J. A., Bae, I. H., Jang, W. H., Kim, J. H., Bak, S. Y., Han, S. H., Park, J. H. & Lim, K. M. Hydrogen peroxide and monoethanolamine are the key causative ingredients for hair dye-induced dermatitis and hair loss. *J. Dermatol. Sci.* **66**, 12–19 (2012).

Chapter Two – Materials & Methods

2 Materials & Methods

This chapter introduces the theory of the characterisation techniques presented in this thesis including X-ray diffraction, thermal analysis and spectroscopic/chromatographic techniques (HPLC, LC-MS, NMR, IR and UV/Vis).

2.1 Generation of X-rays

In laboratories, X-rays are readily available from a conventional X-ray tube where electron kinetic energy is converted to X-rays via interaction with a metal target's core electrons providing particular characteristic wavelengths. In an X-ray tube, electrons are produced in a vacuum through the passing of an electric current through a wire filament which is accelerated to a high velocity via an electric current. The filament is held at a large negative potential with the electrons being attracted to a water-cooled and earthed metal block. The majority of the kinetic energy of the electrons is transferred to heat with a small portion generating X-rays.

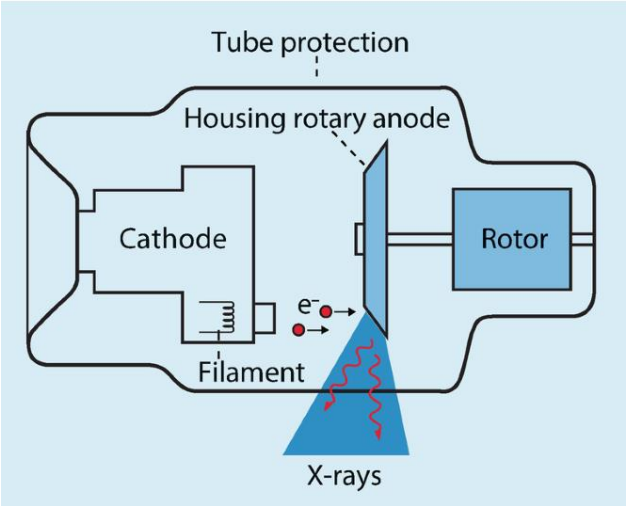

Figure 2.1: Schematic of a conventional X-ray tube. Adapted from Kahl-Scholz, M. & Vockelmann, C. Basic Knowledge of Radiology. Springer, Berlin, Heidelberg.

2.2 X-ray Diffraction

2.2.1 Introduction to Symmetry and Diffraction

A perfectly crystalline material is comprised of an infinitely large number of identical molecules arranged in a precisely regular way which is repeated in all directions resulting in long-range order. Inversion symmetry is present in all three-dimensional lattices, regardless of whether or not the individual unit cell contents are centrosymmetric and as a result, inversion symmetry does not impose any restrictions on the unit cell parameters. The presence of any rotation/reflection symmetry imposes restrictions on the unit cell parameters. The repetition of a single structural unit

in a regular pattern, in an identical orientation is a form of symmetry called translation. Crystalline materials possessing long-range order gives rise to Bragg's diffraction of X-rays resulting in a diffraction pattern with an array of lattice points featuring a range of intensities which yield information about the molecule's orientation.

The lattice shows the structure's repeating nature, but not the actual contents of the structural repeating unit. A translation from one lattice point to another can be shown as a vector which for an arbitrary choice of two lattice points can be comprised through building multiples of three basic unit vectors that between pairs of adjacent lattice points are the shortest three non-coplanar vectors. The three vector lengths are denoted as a, b, c and angles α, β, γ with these three vectors enclosing a shape called the unit-cell being the entire structure's basic building block featuring the equivalent of one lattice point. Unit cells featuring only one lattice point are classified as primitive (P), whereas those featuring multiple lattice points are classed as centred cells. There are different kinds of cell centring possible for the different crystal systems which may feature lattice points: at the centres of one-set of opposite pairs of faces (A, B or C-centred); in the middle of cell-body (body-centring I); or on all faces (face-centred F). The contents of the unit cells can have additional symmetry that allows us to deduce the number of known parameters. The presence of translational symmetry makes other forms of symmetry possible, *e.g.* screw axes and glide planes. The combination of translation and rotation is termed a screw axes with the translational component taking place along the direction of the axis and by an amount which is equal to multiples of 1/n of the repeat lattice in that direction. For example, a two-fold screw which is parallel to the *b*-axis passing through the unit cells origin, this screw axes would consist of a two-fold rotation around the axis of the screw as well as a translation parallel to that axis, *i.e.* a 2_1 screw axes would rotate 180° and translate unit cell. The glide plane is a combination of translation and a mirror plane. In this instance, for a monoclinic system, the mirror is perpendicular to the *b*-axis and the translation of 1/2-unit cell is along the defined direction, *i.e.* a *c*-glide would be a reflection perpendicular to the *b*-axis and then a translation along the *c*-direction.

Table 2.1: List of the seven crystal systems as well as their cell types/restrictions on the unit cell parameters.

Crystal System	Unit Cell Restrictions	Cell Types
Triclinic	None	P
Monoclinic	$\alpha = \gamma = 90°$	P, C (I)
Orthorhombic	$\alpha = \beta = \gamma = 90°$	P, C (A), I, F
Tetragonal	$a = b$; $\alpha = \beta = \gamma = 90°$	P, I
Trigonal	$a = b$; $\alpha = \beta = 90°$, $\gamma = 120°$	P (R)
Hexagonal	$a = b$; $\alpha = \beta = 90°$, $\gamma = 120°$	P
Cubic	$a = b = c$; $\alpha = \beta = \gamma = 90°$	P, I, F

An X-ray diffraction pattern is comprised of a pattern of discrete spots with a range of intensities that yields information regarding the molecules arrangement in the crystal structure. The pattern's symmetry relates to the symmetry of the molecules solid-state arrangement and the intensities provide information about the location of electron density that we can interpret as atom positions in the crystal structure. The structure factor (*F*) (crystal structure) and the electron density (its diffraction pattern) are related in both directions through Fourier transformation and its inverse. For a known structure both phases and amplitude are known and the diffraction pattern can be calculated. From the crystal structure, we can apply the Fourier transform of the diffraction pattern which can be described in terms of the distribution of electron density which is concentrated in atoms. As the scattered X-rays are not capable of being refracted as is done in optical microscopy and cannot be obtained by direct calculation as the waves required relative phases are not known.

2.2.2 Data Collection: The Diffractometer

The crystal has to be mounted on a goniometer head which needs to be fixed in the goniometer centre so the centre remains stationary when the crystal is rotated. A common method of achieving this is by gluing the crystal to the end of a glass fibre which is attached to a metal pin. The ideal glass fibre should be thin so as to minimise the background X-ray scattering contribution, but rigid enough to support the crystal. These frequently have a loop diameter of approximately 100 μm, similar to an incident X-ray beam and viscous oil/glue is used to hold the crystal within the loop. Nowadays, low temperature experiments commonly use an inert mounting oil that secures the crystal and the crystal is easily attached to a nylon loop using the capillary action of the oil and once the oil is frozen, the crystal is held firmly in place. After the experiment, once the crystal has been heated up, it can be removed and the crystal mount can be re-used. There are several advantages to using oil over glue for mounting crystals including moisture/air sensitive crystals during mounting are protected from the atmosphere, the crystal mount can be reused as the attachment is reversible when using oil and the crystals can be manipulated easier on a glass slide when placed in a drop of oil.

When a crystal is bombarded with X-rays of a given wavelength and at specific incident angles, intensely reflected X-rays are generated where the scattered X-rays wavelengths interfere constructively. For constructive interference, the differences in travel path needs to be equal to integer multiples of the wavelength with constructive interference resulting in diffracted beams of X-rays exiting the crystal at an angle which is equal to that of the incident beam. Bragg's law describes diffraction in terms of reflections from crystal planes leading to the very well-known Bragg equation:

$$n\lambda = 2d_{hkl}sin\theta \qquad \text{Equation 2.1}$$

If we consider a crystal featuring crystal lattice planar distances (*d*), the differences in travel path between the paths ABC and A'B'C is integer multiples of the wavelength, for a combination of that incidence angle, the crystal lattice planar spacing and the given wavelength, constructive interference will occur.

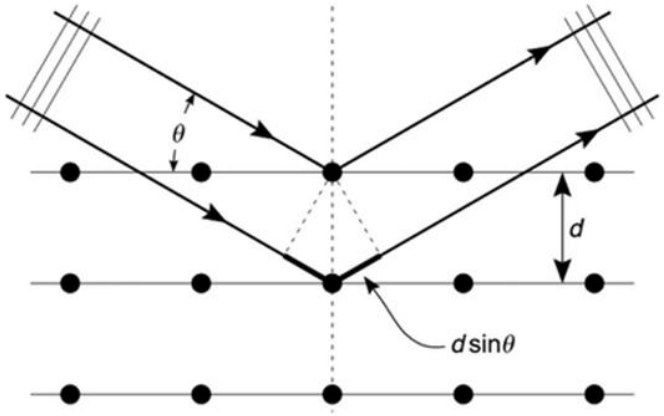

Figure 2.2: Bragg's diffraction of X-rays from a set of crystals planes. Adapted from Terzano, R. et al. Recent advances in analysis of trace elements in environmental samples by X-ray based techniques (IUPAC Technical Report). Pure Appl. Chem. **91**, 1029–1063 (2019).

For describing when sets of lattice planes are in a diffracting position, it is required to know the planes orientation and the interplanar spacing which can be thought of as a vector. Each individual reflection can be linked to a single vector known as its scattering vector or diffraction vector. If we take every scattering vector for all reflections and start these vectors from a single origin point, then this will result in the vector ends being regularly positioned in three dimensions producing the reciprocal lattice. The direct unit cell parameters are usually denoted by a, b, c, α, β, γ and the reciprocal lattice's unit cell parameters by a^*, b^*, c^*, α^*, β^*, γ^*.

The Ewald sphere, also known as the Ewald construction is a geometrical expression of Bragg's law involving a sphere of reflection and the reciprocal lattice. The Ewald sphere features a sphere of radius $1/\lambda$ which is positioned around the crystal, where the wavelengths of X-rays are denoted by λ. A set of planes are arranged so that an angle ϑ is made to the incident beam. The origin of the reciprocal lattice is rotated around the origin until a node in the lattice cuts the sphere, thus providing the diffracting conditions. The diffraction direction can be determined by drawing a line from the crystal to the point of intersection. The boundary between observable and unobservable reflections is defined by the limiting sphere. The radius of the limiting sphere ($2/\lambda$) is double that of the reflecting sphere meaning that the number of reflections that can be collected is dependent on the wavelength. As the wavelength gets shorter, the size of both the limiting and reflecting spheres gets larger with the lattice point separation for a particular crystal remaining constant which explains why for molybdenum, far more reflections can be collected compared to copper.

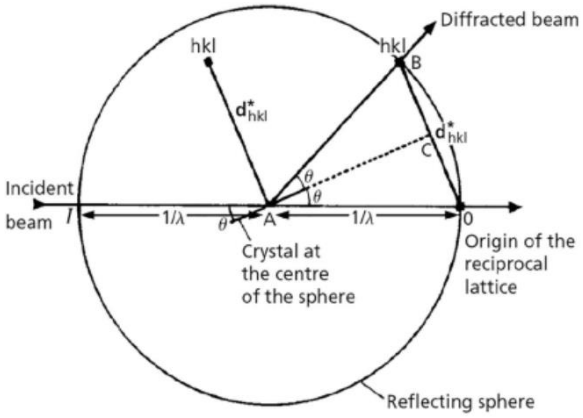

Figure 2.3: The Ewald sphere construction for a set of lattice planes at the appropriate Bragg angle. A sphere is drawn of radius (1/λ) with the crystal at the centre. The reciprocal lattice origin is fixed at O and the reciprocal lattice point (hkl) cuts the sphere at the diffracted beams exit point. Adapted from Ameh, E. S. A review of basic crystallography and x-ray diffraction applications: Int. J. Adv. Manuf. Technol. ***105****, 3289-3302 (2019).*

Modern day diffractometers featuring area detectors normally possess three or four independent motors that can drive the crystal into almost any orientation with respect to the X-rays incident beam. For the motors to be able to dial up a particular reflection *hkl* reflection during a data collection, the diffractometer axes *x*, *y*, *z* that the motors are defined upon have to be related with the axes defining a diffraction pattern for a given crystal, *i.e.* the reciprocal unit cell axes, therefore *hkl* can be calculated. The orientation matrix, which is a 3 × 3 matrix allows this relation:

$$X = A\,h \qquad \text{Equation 2.2}$$

The vectors (*x*, *y*, *z*) and (*h*, *k*, *l*) are represented by x and h respectively, with A being the orientation matrix which is defined by:

$$A = \begin{pmatrix} a_x^* & b_x^* & c_x^* \\ a_y^* & b_y^* & c_y^* \\ a_z^* & b_y^* & c_z^* \end{pmatrix} \qquad \text{Equation 2.3}$$

This matrix's nine elements represent the components of the reciprocal cell axes for each axis (*x*, *y*, *z*). The matrix elements provide information regarding the unit cell (requires six parameters) and the crystals orientation (requires three parameters). The unit cell parameters can therefore be determined using the following equation:

$$(A'A)^{-1} = \begin{pmatrix} a.a & a.b & a.c \\ b.a & b.b & b.c \\ c.a & c.b & c.c \end{pmatrix} \quad \text{Equation 2.4}$$

Where the transpose of the orientation matrix, A is denoted as A'.

The majority of single crystal small molecule studies measure an area of diffraction instead of single reflections from a crystal. Detection up until recently was normally done with a charged coupled device (CCD) or image plate with the former being much more common. For image plates, rather than converting X-rays into visible light, the phosphor present in these devices retains the image as a trapped electron colour centre. These are then read via stimulation from visible laser light and erased using strong visible light before again being exposed to X-rays. Some of the main advantages of image plates are that they are relatively inexpensive, have a high spatial resolution and high receding efficiency, however, the main disadvantage is that they require a separate read-out process requiring minutes instead of seconds.

CCD detectors consist of a semi-conductor chip containing a square array of pixels/light-detecting cells and the X-rays have to be converted into light to work which is achieved using a phosphor. The phosphor which produces the light is protected by a beryllium window with beryllium used as its relatively strong and its low atomic weight allows for the transmission of X-rays to the phosphor. The type/thickness of the phosphor normally depends on the wavelength that will most commonly be used. Once the light has been generated, it has to be detected by the CCD chip which can be done directly or via a fibre optic taper. The taper is a funnel of drawn out glass bundles which reduces the size of the pattern of light on the phosphor for it to be measured on a smaller chip. Use of the CCD chip can be split into two phases: exposure of the CCD chip to light and readout of the result. The first phase involves the CCD passively collecting incoming photons: the creation of electron-hole pairs and the electrons are stored in the potential wells which are the pixels. CCD's are analogue devices (*i.e.* each cell has an associated voltage) and the second phase involves the conversion of information from each pixel to a digital format.

Hybrid photon counting (HPC) detectors have significantly improved X-ray detection for a range of applications and over a wide energy spectrum with their success being attributed to the accurate determination of the scattered photon's intensities over a high dynamic range whilst ensuring single photon sensitivity. The main reasons for their superiority over other detectors are the accurate determination of diffraction/scattering intensities over a very high dynamic range as well as the direct detection of individual photons. HPC detectors were firstly utilised in macromolecular crystallography, revolutionising data collection and have also been employed for coherent scattering, small angle scattering, increase high energy applications, spectroscopy and powder X-ray diffraction.

The electron density can be defined as a smoothly varying continuous function with units of electrons per cubic Angstrom (e $Å^{-3}$) at every point in the crystal structure. It is more convenient to describe the structure in terms of the displacements and positions of the individual atoms, with their individual electron-density distribution. The atoms are taken to be spherical in most cases when stationary and their individual X-ray scattering contribution is known as atomic scattering factors. The atoms X-ray scattering effects are altered by atomic displacements causing the at-rest electron density to be spread out over a greater volume and normally unequally in different directions (anisotropic) and given a set of anisotropic displacement parameters (adps) for every atom, this effect can be described by the following equation:

$$F\ (hkl) = \sum_{j=1}^{N} f_j \exp\left[2\pi i\left(hx_j + ky_j + lz_j\right)\right]. \qquad \text{Equation 2.5}$$

The structure factor, *F* (*hkl*) of any reflection is the quantity which expresses both the phase and amplitude of that reflection playing a pivotal role in the refinement and solution of crystal structures. This is because it represents the quantity related to the reflection's intensity which in turn depends on the structure giving rise to that reflection and is independent of the conditions and methods of observation of that reflection. The set of structure factors for all reflections are the primary quantities required for derivation of the 3D electron-density distribution which is the image of the crystal structure, determined using Fourier methods. The way in which the diffracted X-rays are combined forming an image depends on three factors: the phase, amplitude and direction. The diffracted beams are observed separately and their intensities are measured as the blackness of spots by direct quantum counting on a diffractometer. Through identifying the miller indices of the crystal planes giving rise to each diffracted beam, the beams direction can be specified. The amplitude can be readily deduced from the beams measured directly. Unfortunately, there is no available method for observing the phase of each diffracted beam which is the last piece of information required for mathematical recombination for an image of the structure to be possible which is known as the phase problem.

The crystal structure solution consists of applying some technique to obtain the approximate phases for at least some of the reflections and the structure refinement process involves extending the knowledge of the phases for all reflections which is made as accurate as possible for all reflections. Except from direct methods, the refinement/solution processes depend on the ability to determine the structure factors for an approximate arrangement of some of the atoms in the crystal structure. It's possible to simultaneously calculate both the phase and amplitude for each beam which would be diffracted by the proposed structure, but as the phases cannot be compared with observable quantities, the proposed structure's validity may be tested by comparing the calculated values of the

amplitudes of the structure factor (F_c) with the observed amplitudes (F_0). This is done by calculating an *R* factor shown using the following equation:

$$R = \frac{\sum ||F_0| - |F_c||}{\sum |F_0|},$$ Equation 2.6

Where the summation is taken over all reflections providing significant intensities. Due to random errors in the structure factors amplitude of the observed structure (F_0) and approximations made on the model of which the calculated structure factors are based, it's not possible to obtain a set of F_c which reproduce the observe structure factors exactly, so the structure refinement never reduces the *R* factor to zero. The structure factor represents the X-ray scattering power for the whole crystal structure, however, due to the large number of unit cells which scatter in phase with each other, the overall scattering power is determined for the contents of only a single unit cell. The structure factor represents the resulting phase and amplitude of scattering all the electron-density from an isolated electron with the phase determined relative to a phase of zero by a point at the unit cells origin for hypothetical scattering.

2.3 Thermal Analysis

Thermal Analysis are a well-known class of techniques for obtaining quantitative and qualitative information regarding the effects heat has on materials including polymers, pharmaceuticals, alloys, new chemical compounds, *etc.* In the pharmaceutical industry, the most common thermal analysis techniques are undoubtedly differential scanning calorimetry (DSC) and thermogravimetric analysis (TGA) as these techniques not only allow for solid-state transitions, melting, sublimation and crystallisation to be observed, they can also be quantified. These techniques measure a materials physical property as a function of temperature when the sample is exposed to a controlled temperature.

2.3.1 Differential Scanning Calorimetry (DSC)

Differential Scanning Calorimetry (DSC) is the thermal analysis technique of choice due to its ability to provide information regarding a material's physical and energetic properties which in most cases cannot be determined as quickly/accurately using another technique. DSC has found applications in ceramics, pharmaceuticals, life science materials and polymers. The underlying concept of DSC is to obtain information regarding thermal changes to a sample by heating/cooling along with an inert reference. The instrument provides quantitative information regarding endothermic, exothermic and changes in heat capacity as a function of time and temperature including purity, glass transition temperature and melting. The variation of energy allows for the discovery and analysis of thermal transitions that a sample undergoes quantitatively and to characterise the material for different thermal events including melting, transitions, crystallisation, *etc.*

2.3.2 Thermogravimetric Analysis (TGA)

Thermogravimetric analysis (TGA) is classed as a thermal analysis technique which measures the sample mass as a function of temperature whilst the sample is subjected to a controlled temperature program. This technique can yield information regarding the physical phenomena associated with a mass change, *e.g.* adsorption, desorption, absorption, sublimation, *etc.* TGA is a complimentary technique to DSC which can help satisfy the user regarding a material's thermal behaviour. Information regarding chemical transformations can be obtained from TGA, *e.g.* decomposition, dehydration, polymer degradation, *etc.*

2.4 Analytical Techniques

2.4.1 UV-Vis Spectroscopy

Most functional groups and organic molecules are transparent in the regions of the electromagnetic spectrum we call the visible and ultraviolet regions with wavelengths ranging from 190-800 nm. When continuous radiation passes through a material which is transparent, a portion of the radiation can be absorbed. The residual radiation when passed through a prism results in a spectrum known as an absorption spectrum. Atoms/molecules pass from a low energy state (*i.e.* the ground state) to a higher energy state (*i.e.* an excited state) due to energy absorption. The absorbed electromagnetic radiation has an energy which is equal to the difference in energy between the ground and excited states. In UV/Visible spectroscopy, the transitions which result in the absorption of electromagnetic radiation in this region of the spectrum are transitions between electronic energy levels. An electron is promoted from an occupied orbital to an unoccupied orbital of higher potential energy as a molecule absorbs energy, with the most probable transition generally being from the highest occupied molecular orbital (HOMO) to the lowest unoccupied molecular orbital (LUMO). The lowest energy occupied molecular orbitals for most molecules are the σ orbitals with the π orbitals lying at higher energy levels. Orbitals holding unshared pairs, *i.e.* non-bonding orbitals lie at higher energy with the unoccupied anti-bonding orbitals (σ* and π*) are the highest energy levels.

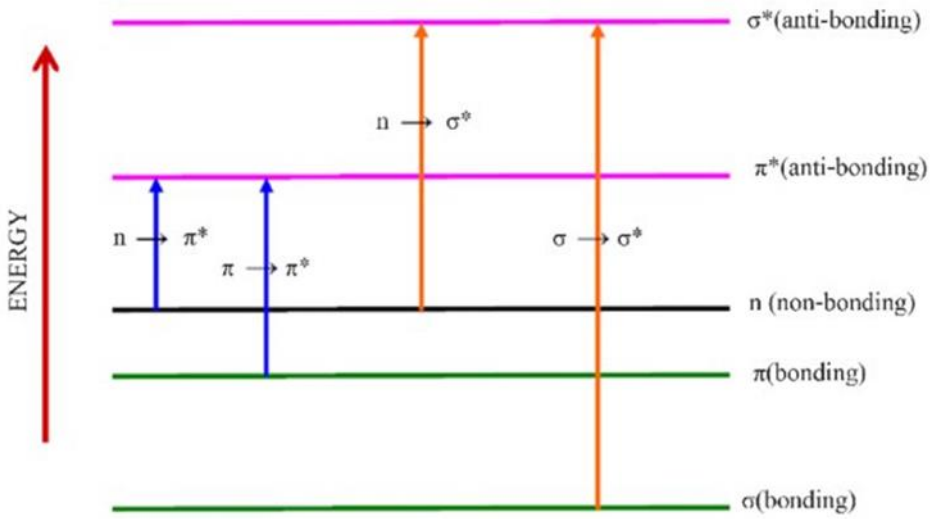

Figure 2.4: Schematic representation of the electronic transitions observed in UV/Vis spectroscopy. Adapted from Sagadevan, S. & Murugasen, P. Studies on Optical, Mechanical and Electrical Properties of Organic Nonlinear Optical p-Toluidine p-Toluenesulfonate Single Crystal. J. Cryst. Process Technol. 04, 99-110 (2014).

At a given wavelength, the higher the number of molecules capable of absorbing light, the larger the extent of light absorption.

UV/Visible spectrophotometers are comprised of a monochromator, light source and a detector. The light source is normally a deuterium lamp which emits electromagnetic radiation in the UV region and a tungsten lamp is used for wavelengths in the visible region. The monochromator is a diffraction grating and its function is to separate the beams of light into its component wavelengths. The desired wavelength is then focused onto the sample cell using a system of slits. The light passing through the sample cell reaches the detector which records the transmitted light's intensity (*I*). The detector is usually a photomultiplier tube, but some modern instruments use photodiodes. In a typical double-beam instrument, the light coming from the source is divided into two beams: the sample and reference beams. The detected light is equal to the intensity of light entering the sample when the reference beam contains no sample cell. The sample cell needs to be constructed of a material transparent to the electromagnetic radiation being used. For spectra in the UV region, cells made of quartz must be used as they don't absorb radiation in this region and in the visible region, cells comprised of plastic and glass are suitable.

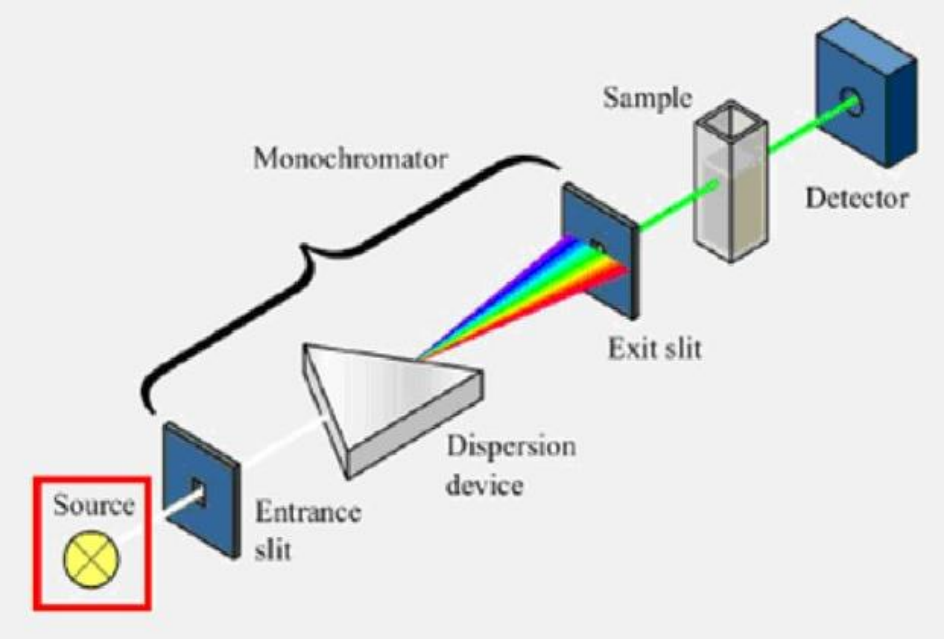

Figure 2.5: Schematic representation of a typical UV/Vis spectrometer. Adapted from Gohain, N. Studies on the structure and function of phenazine modifying enzymes PhzM and PhzS involved in the biosynthesis of pyocyanin. Phd Thesis (2008).

2.4.2 High Performance Liquid Chromatography

High Performance Liquid Chromatography (HPLC) is the advanced version of traditional chromatographic techniques such as thin layer chromatography (TLC), paper chromatography, *etc.* HPLC is extensively used in the pharmaceutical industry and can only analyse samples which are in solution with the technique separating compounds which are dissolved in a solution allowing for quantitative and qualitative analysis of the components and the quantities of each component dissolved.

HPLC employs high pressure to push the mobile phase through the column/stationary phase which consists of small particles densely packed inside a column. The column is comprised of a cylindrical tube filled with small spherical particles (normally 1.5-5 μm in diameter) which is usually porous silica with an individual pore. The individual pore is covered with the stationary phase, commonly C_{18} groups attached to the silica particle with the particle formed via aggregating small, spherical, sub particles. The pores are created by the spaces between the sub particles with almost all of the particle surface contained within the pores. Any mixture which is passed through the column, different types of physical and chemical interactions occur between the compound of interest and the column packing with the higher affinity components moving through the column slower, whereas the lower affinity components travel faster through the column. As each component has a different affinity, they are separated/eluted from the column at different times. The HPLC mobile phase composition is dependent on the nature of the compound as well as the stationary phase and a combination of two or more solvents are commonly used as the mobile phase with the proportions of the different solvents acting to adjust the mobile phase polarity. The detector is positioned at the column outlet and the mobile phase carrying the separated analytes is passed through the detector and then is converted to an electrical signal.

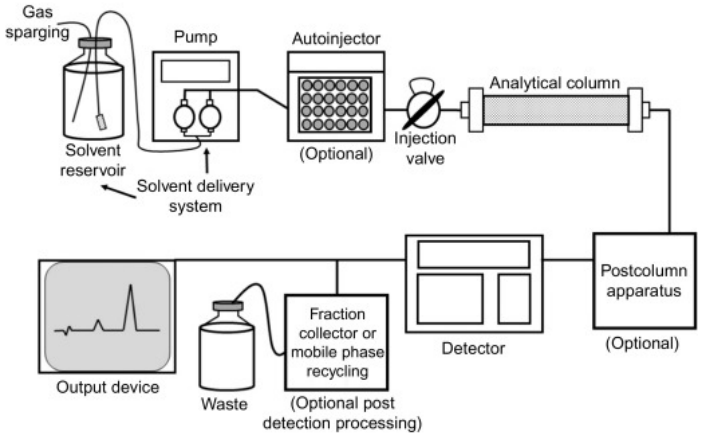

Figure 2.6: Schematic representation of a typical HPLC instrument. Adapted from LaCourse, M. E. & LaCourse, W. R. General Instrumentation in HPLC. Liquide Chromatography: Fundamentals and Instrumentation: Second Edition 1, 417-429 (Elsevier, 2017).

The two most common HPLC separation modes are normal phase chromatography and reversed phase chromatography. In normal phase, a polar column is used (*e.g.* un-bonded silica) in combination with less polar organic solvents with this separation mode commonly used for water-insoluble samples, the separation of isomers and preparative HPLC. Reversed phase (RPC) features a non-polar column and the mobile phase composition is a mixture of water and an organic solvent, *e.g.* acetonitrile with RPC being the most widely used separation mode. Other common separation modes include size exclusion chromatography, ion-pair chromatography and hydrophilic interaction chromatography (HILIC). In ion-pair chromatography, the same conditions are used as in reversed phase, except for an ion-pairing reagent being added to the mobile phase for interaction with ions of the opposite charge. In size-exclusion chromatography (SEC), an inert column is employed with an organic or aqueous mobile phase with SEC providing separation based on molecular weight which is commonly used for synthetic polymers or large biomolecules. In hydrophilic interaction chromatography (HILIC), a polar column is used in combination with a mobile phase consisting of a mixture of organic solvent plus water. HILIC is commonly used to separate samples which are highly polar and as a result are poorly retained in RPC.

2.4.3 Liquid Chromatography Mass Spectrometry (LC-MS)

Mass Spectrometry (MS) is a very powerful analytical technique used in the identification and quantification of both known/unknown compounds as well as to elucidate the chemical properties and structure of molecules. Mass spectrometry is based on the formation of the positive ion of a molecule. The technique involves firstly converting the sample into gaseous ions (containing an even or odd number of electrons) with the ions featuring different chemical properties. The positively charged ion is known as the molecular ion (M+) or parent ion and these molecular ions because of their high instability, break down further into single/multiple daughter ions. The ions are then separated according to their mass-to-charge ratio (*m*/*z*) and detected by a detector resulting in a spectrum of ions of varying intensities. The ions intensities are directly proportional to the molecule's abundance in the mixture and the ions also provide information on the structure and nature of the molecule. Mass spectrometers operate under high vacuum to allow for the facile movement of ions to the detector avoiding any inelastic/elastic collisions since they not only influence the ions trajectory as well as making them lose their energy.

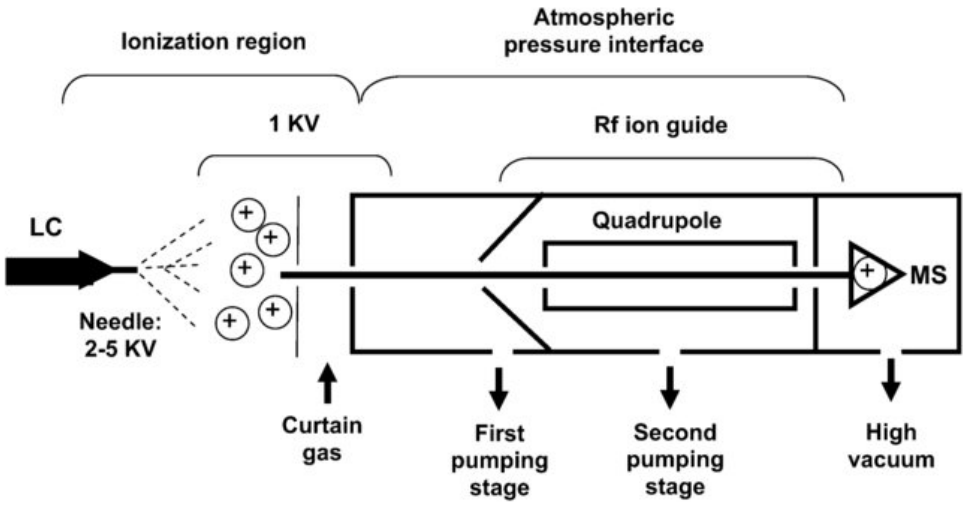

*Figure 2.7: Schematic of a typical LC-MS system. Adapted from Brima, E. I., Jenkins, R. O. & Haris, P. I. Understanding arsenic metabolism through spectroscopic determination of arsenic in human urine. Spectroscopy **20**, 125-151, 2006.*

Electrospray Ionisation (ESI) is the most common method of ionisation for transitioning molecules from the solution state to individual ions with this technique being popular when used in combination with LC. ESI allows for a very high sensitivity and is also easily coupled to HPLC or capillary electrophoresis. ESI is produced through the application of a strong electric field under atmospheric pressure to a liquid which passes through a capillary. The electric field is produced through the application of a potential difference of 3-6 kV between the counter-electrode and the capillary. The electric field forms a charge accumulation at the liquid surface positioned at the end of the capillary which will break forming highly charged droplets. The droplets are passed through a

curtain of heated inert gas, commonly nitrogen or through a heated capillary to remove the remaining solvent molecules. Under the strong electric field, deformation of the droplet takes place. Under the force, the droplet elongates resulting in a new taylor cone which releases 20 smaller droplets. Ions are generated as a result of the electrochemical process and the accumulation of the charge within the droplets.

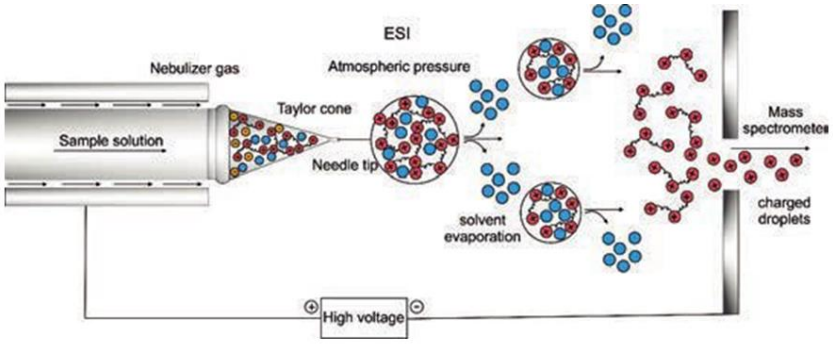

Figure 2.8: Schematic representation of the electrospray ionisation process with positive ions (red circles), negative ions (orange circles) and solvent molecules (blue circles). Adapted from Thangaraj, S. K. Applications of high-resolution mass spectrometry to structure-function studies of proteins. PhD diss. (Itä-Suomen yliopisto, 2019).

After ionisation of the analyte occurs in the ion source, the mass analyser resolves the ions based on their mass-to-charge ratio (*m*/*z*). The most common mass analysers include the quadrupole, time-of-flight, ion trap and Fourier transform analysers (*i.e.* orbitrap and ion cyclotron) with the choice of mass analyser depending on a number of factors/experimental considerations including mass of analyte, desired *m*/*z* range, required limit of detection, mass analyser's required resolving power and the mass analyser's ability to interface with the ion source.

The quadrupole mass analyser is one of the most commonly used mass analysers which is essentially a mass filter because of its ability to filter ions of different *m*/*z*. Quadrupoles are comprised of four cylindrical/hyperbolic rods parallel to each other with the rods opposite each other connected together electrically and a radio frequency (RF) is applied. A direct current potential (DC) is superimposed over the RF potential with the combination of RF/DC potentials causing the oscillation of ions as they pass through the quadrupole in the *z*-direction. Depending on the frequency of the RF field and the DC potential, only ions of a particular *m*/*z* will have stable trajectories and the ions with unstable trajectories colliding with rods and being filtered out. Ions of differing *m*/*z* can be filtered/scanned out through the quadrupoles by varying the DC/RF potentials. A quadrupole or multipole can also function in 'RF-only', whereby the DC potential is reduced and only an RF potential is applied to the rods which allows the ions to pass through the multipole, thus transforming the quadrupole mass analyser into a transmission device where ions can be transmitted from one section of the MS to another.

Ion trap mass analysers are a modification of the quadrupole mass analyser. Until the twenty-first century, the most common ion traps were the 3D trap, more recently the 2D ion trap has increased in popularity due to advantages compared to 3D traps. 3D traps are comprised of two hyperbolic electrode plates which face each other with a hyperbolic ring electrode placed in between. By means of an oscillating RF field and a superimposed DC electric field, similar to in quadrupoles, trapping of ions between the electrodes occurs. To function as a mass analyser, ions of different *m*/*z* are selectively ejected from the ion trap through varying the RF potential and then the ejected ions are registered at the detector.

Fourier Transform Ion Cyclotron (FT-ICR) analysers determine *m*/*z* through measurement of the ions cyclotron frequency in a mixed magnetic field. Firstly, ions are introduced into a Penning trap, a device which is similar to a 3D trap, but which uses a magnetic field rather than an electric field to trap the ions. The ions are injected as a "packet" from the source into the magnetic field with the ions then experiencing a Lorentz force causing them to assume a circular motion which is in a plane perpendicular to the magnetic field. As the ions are not in phase when first introduced into the trap and normally have very small orbits, it's impossible to detect them. For the ions to be detected, they need to be coherently excited to a larger radius within their plane of motion which can be achieved through exciting the ions using a limited frequency sweep loop of a broadband RF field. This excitation places the ions in a higher cyclotron orbit allowing them to be detected. As the ions are detected by the receiver plates over time, their signal intensity is digitised with respect to time and using a Fourier transform is converted to a frequency spectrum.

The Orbitrap which is similar to the FT-ICR, also utilises the Fourier transform to convert a signal, produced by oscillating ions in a trap from the time domain to a frequency domain. Orbitrap mass analysers utilise an electric field to induce these oscillations in the ions, in comparison to FT-ICR analysers which use a magnetic field. The Orbitrap is comprised of three main parts, an inner spindle electrode which is covered by two hollow outer concave electrodes facing each other with the outer electrodes separated by a thin ring of dielectric material. A voltage potential is applied between the outer and inner electrodes forming a linear electric field between them. Ions are tangentially introduced into the orbitrap as a "packet" between the outer and inner electrodes via a hole machined into one of the outer electrodes. As a result of the electric field between the outer and inner electrodes, the ion packet is bent towards the inner electrode whilst the ions tangential velocity creates an opposing centrifugal forces. At a certain potential between the outer/inner electrodes, the ions remain in a spiral path around the inner electrode, however, as a result of the electrodes conical shape, a harmonic axial oscillation in the ion is induced. The outer electrodes act

as receiver plates which detect the ions back and forth axial harmonic motion with this signal image then digitised and converted from the time to frequency domain.

2.4.4 Nuclear Magnetic Resonance Spectroscopy (NMR)

Nuclear Magnetic Resonance (NMR) is the most widely used and powerful spectroscopic technique used in the determination of molecular structures both as pure liquids and in the solution state. In most cases, it yields information regarding the symmetry/shape with greater certainty than is possible from other spectroscopic techniques such as Raman or IR spectroscopy. It can also provide information regarding the nature/rate, for example in the interchange of ligands in fluxional molecules as well as being capable of following reactions in mechanistic detail. However, NMR studies of molecules in the solution state cannot determine accurate bond distances/angles, although it can provide information on internuclear separations. NMR sensitivity depends on various factors including the size of its nuclear magnetic moment and the isotope's abundance.

NMR spectrometers consist of three components: a probe, superconducting magnet and complex electronic system known as the console. The superconducting magnet is responsible for producing a strong magnetic field which aligns the nuclear spins of atoms in the sample. Magnets commonly used nowadays are based on superconducting materials which require very low temperatures to operate (*i.e.* 4 K). As a result, NMR spectrometers contain a cooling system comprised of an inner jacket which is filled with liquid helium that is refrigerated using an additional jacket containing liquid nitrogen and many layers of thermal isolating materials. The superconducting magnet surrounds a cylindrical chamber referred to as the "probe" which is an essential part of the instrument. The sample is introduced into the probe and placed under the magnetic fields influence and additionally the probe features a series of magnetic coils located around the sample. The coils have multiple roles including irradiating the radiofrequency pulses, detecting/collecting the signal emitted from the sample as well as enabling the control of the homogeneity of the magnetic field and application of pulse gradients. The spectrometer's electronic system controls the experimental conditions and allows the set up/modification of each NMR parameter through the workstation. This system is also responsible for data collection as well as mathematical transformation into the NMR spectrum.

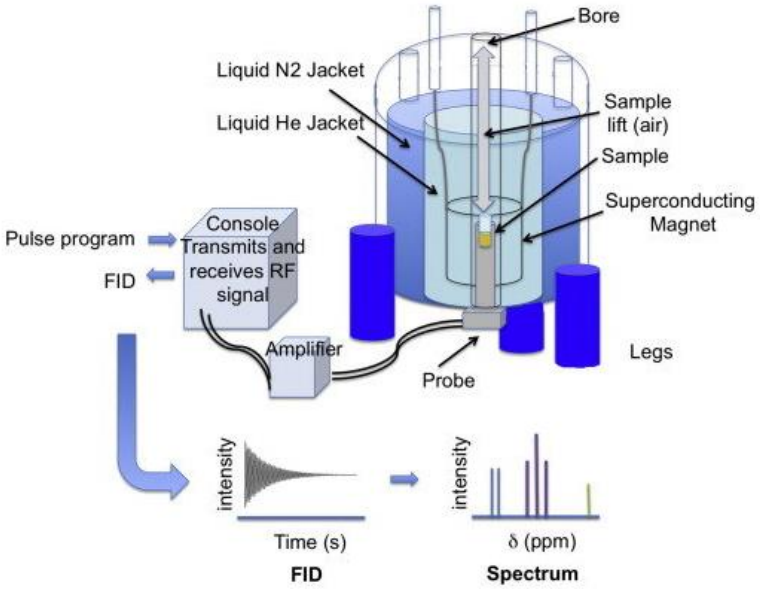

*Figure 2.9: Schematic of a typical NMR spectrometer. Adapted from Rankin, N. J., Preiss, D., Welsh, P., Burgess, K. E. V., Nelson, S. M., Lawlor, D. A. & Sattar, N. The emergence of proton nuclear magnetic resonance metabolomics in the cardiovascular arena as viewed from a clinical perspective. Atherosclerosis **237**, 287-300 (2-14).*

A nucleus with spin *I* can take up to 2*I* + 1 orientations with respect to the applied magnetic fields direction with each orientation having a different energy, the most highly populated being the lowest level. The NMR sensitivity is low, however, this can be increased through using a stronger magnetic field that increases the population difference, the energy difference and signal intensity. Originally, spectra were obtained using a continuous wave mode where the sample is subjected to a radiofrequency which is constant and the encountered resonances are recorded as the field is increased or the radiofrequency is swept and the field is constant. In contemporary spectrometers, energy separations are identified through exciting nuclei in the sample using a sequence of radiofrequency pulses and observing the nuclear magnetization return to equilibrium. An NMR transitions frequency depends on the local magnetic field which is experienced by the nucleus and can be expressed in terms of the chemical shift, δ, which is the difference between the nuclei's resonance frequency in the sample and that of a compound reference which is commonly tetramethylsilane $Si(CH_3)_4$ (TMS) for ^{1}H, ^{13}C and ^{29}Si. The nucleus is said to be shielded when the chemical shift is less than zero and de-shielded when the chemical shift is greater than zero relative to the standard. Spin-spin coupling results when the orientation of a spin of a nearby nucleus effects the energy of another nucleus leading to small changes in the location of that nucleus's response. The spin-spin coupling constant, *J*, decreases rapidly through chemical bonds with distance and is normally greatest when the atoms are directly bonded. The coupling constant sizes are related to a molecule's geometry through noting empirical trends. A signals integrated intensity resulting from a group of chemically equivalent nuclei will be equivalent to the number of nuclei in that group.

2.4.5 Infrared Spectroscopy (IR)

Almost any organic/inorganic compound with covalent bonds absorbs several frequencies of electromagnetic radiation in the electromagnetic spectrum's infrared region. When molecules absorb infrared radiation, they are excited to a higher energy state which like other absorption processes is a quantized process. Absorption of infrared radiation corresponds to changes in energy of the order of 8-40 kJ/mole with the radiation in this energy range encompassing the bending and stretching vibration frequencies of the bonds in most covalent molecules. In the absorption process, frequencies of infrared radiation matching the natural vibration frequency of the molecule are absorbed. Not all bonds in a molecule can absorb infrared radiation, only those which have a dipole moment which changes as a function of time can absorb infrared radiation.

There are two types of IR spectrometers commonly used: Fourier transform and dispersive instruments. A dispersive IR spectrometer generates a beam of infrared radiation from a hot wire and by use of a mirror, the infrared radiation is divided into parallel beams of equal-intensity radiation. The sample is placed in one of the beams and the other beam is used for the reference with the beams then passed into the monochromator which disperses the beams into a continuous spectrum of frequencies of infrared light. The monochromator is comprised of a rapidly rotating sector which passes the two beams alternately to a diffraction grating with the slowly rotating diffraction grating varying the wavelength/frequency of radiation which reaches the thermocouple detector. The detector senses the ratio between the sample and reference beams intensities and determines which frequencies have been absorbed by the sample. Most modern IR spectrometers operate on a different principle with the design of the optical pathway producing a pattern known as an interferogram. The interferogram is a complex signal with its wave-like pattern containing all the frequencies making up the IR spectrum which is essentially a plot of intensity against time. Fourier transform (FT) which is a mathematical operation separates the individual absorption frequencies from the interferogram which produces a virtually identical spectrum to that which is produced from a dispersive instrument. An FT-IR instrument has the advantage of acquiring the interferogram in under a second and when a FT is performed on the sum of the accumulated interferograms, the resulting spectrum has a better signal-to-noise ratio. Therefore, an FT-IR instrument is capable of greater sensitivity and speed in comparison to a dispersive instrument.

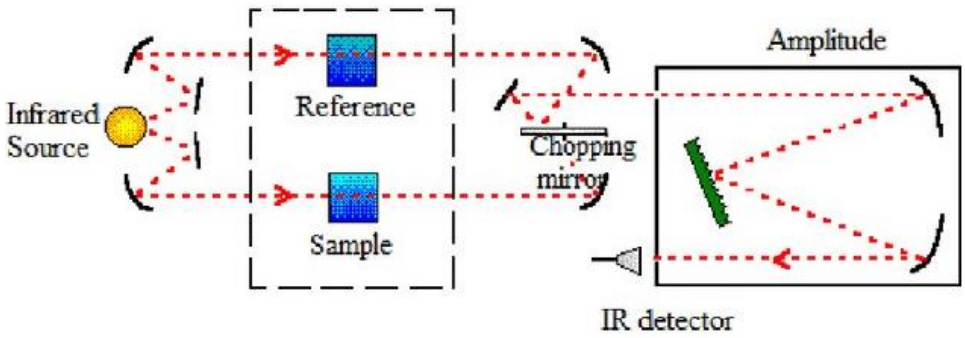

Figure 2.10: Schematic representation of a typical dispersive IR spectrometer. Adapted from Smith, B. C. Introduction to Infrared Spectroscopy. Fundamentals of Fourier Transform Infrared Spectroscopy 15-32 (CRC Press, 2011).

Chapter Three – Reactivity of PPD

3 Reactivity of PPD

The main goals/objectives of this chapter are firstly to investigate the colour change observed in the case of PPD as well as the salt forms of PPD. The investigation of the colour will be investigated through exploring the solution reactivity using various chromatographic and spectroscopic techniques for not only PPD, but also for the salt forms. In addition, we want to understand whether salt formation helps to aid in stabilising PPD in solution.

3.1 Introduction

p-Phenylenediamine (PPD) is an aromatic amine which is commonly used in permanent hair colouring products as a primary intermediate and also for skin colour in black henna dyes which can cause the human body to experience mutagenic, anaphylactic and carcinogenic effects.[1-2] Except from its use in hair products, PPD and its derivatives are used in antioxidants, pharmaceuticals and tattoo colours.[3]

Literature available on the chemistry of PPD has shown that it undergoes oxidation resulting in the formation of dimeric, trimeric and polymeric derivatives via oxidative coupling of at least two PPD molecules. Many attempts have been made to characterise the oxidation products over the last forty years, but modern analytical techniques were not taken advantage of. An HPLC-UV method in reversed phase mode (RPLC) in combination with electrospray ionisation mass spectrometry was used to characterise the oxidative transformation products of PPD.[4]

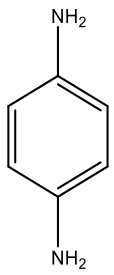

Figure 3.1: Chemical structure of PPD.

PPD, as well as its oxidation products, are of environmental and toxicological concern and are classed as toxic, carcinogenic and mutagenic in vitro.[5] PPD is one of the most commonly used chemicals in permanent hair dyes and as a result, there are several health effects associated with exposure to PPD.[6] In the context of occupational health, the use of PPD in tattoo and hair dye formulations is subject to several regulations.[5] Several studies have indicated that PPD is a human allergen and exposure to allergens like PPD can lead to allergic contact dermatitis with sensitisation to PPD in the long run resulting in a sensitivity to all materials that contain PPD.[7-8]

Exposure to PPD via the hair colouring process is thought to be less sensitising than via other processes, *e.g.* labile temporary tattooing. In hair dye formulations, several ingredients in particular hydrogen peroxide reduces the sensitising potential of PPD through accelerating the speed of oxidation.[9] Previous work in our group has investigated the co-crystallisation of PPD which resulted in the formation of three coloured salts which showed intense colour. These salts were used to dye hairs and were shown to retain their colour after extensive washing. These supramolecular hair dyes are thought to be safer than current oxidative hair dyes.[10]

Hydrophilic Interaction Chromatography (HILIC) will be introduced as whilst it's still a relatively new separation mode, it's suited to more polar compounds and could be beneficial in the separation of PPD. HILIC is a variant of normal phase chromatography (NPC) which utilises water in a water miscible organic solvent as the eluent in conjunction with a stationary phase that is hydrophilic. Over the last few years, HILIC has been gradually gaining interest and has emerged as an alternative to reversed phase chromatography (RPLC) for several applications related to hydrophilic and polar compounds.[11] The mechanism of retention in HILIC has not been completely elucidated even though it has been extensively studied in recent years. The retention mechanism is thought to involve the partitioning of hydrophilic substances between an aqueous layer that is stagnant imposed on the hydrophilic stationary phase and an organic phase that is more hydrophobic. It has been suggested that other interactions including ionic interactions, hydrogen bonding and even Van der Waals effects may contribute to the retention. All interactions in HILIC have been observed to be dependent on the solute, type of stationary phase, presence of additives and the amount of organic in the eluent.[12]

We have set about to investigate the stability of PPD in both pure and salt forms based on the reported reactivity and the advantages of HILIC and other modern analytical techniques.

3.2 Materials & Methods

3.2.1 Materials

p-Phenylenediamine (PPD, purity ≥99%, Lot No: WXBB8077V), sebacic acid (SebA, purity 99%, Lot No: MKBR472V), trimesic acid (TMA, purity 95%, Lot No: 10507TE) and lawsone (L, purity 97%, Lot No: STBD5846V) were obtained from Sigma-Aldrich and were used as received without any further purification.

3.2.2 Liquid Assisted Grinding (LAG) Experiments

LAG experiments were carried out using a Retsch MM400 mechanical mill equipped with 10 mL stainless steel grinding jars and two 7 mm steel balls per jar. A small quantity of methanol (approx. 50 μL) was added and the milling process was carried out at a frequency of 30 Hz for 30 minutes.

Table 3.1: List of weights of each component used in LAG experiments.

	Weight of PPD (mg; mmol)	Weight of Co-Former (mg; mmol)
PPD-SebA	221.5; 2.048	224.0; 1.108
PPD-TMA	114.3; 1.057	229.7; 1.093
PPD-L	113.8; 1.052	312.7; 1.796

3.2.3 Powder X-ray Diffraction (PXRD)

The materials obtained from LAG experiments were analysed by PXRD. PXRD was carried out using a flat-plate transmission geometry multi-well Bruker D8 Advance II powder diffractometer using Cu-Kα radiation (λ = 1.5406 Å) at approximately 21 °C-24 °C. Data was collected between a 2ϑ of 4-35°, a step size of 0.017° and S_1/step.

3.2.4 UV/Visible Spectroscopy (UV/Vis)

UV/Vis measurements were recorded using a Thermo Fisher Thermo Spectronic HELIOS alpha spectrophotometer in the scan range of 190-800 nm. Stock solutions of approximately 2% w/v were prepared in methanol before being sufficiently diluted to yield an absorbance value of 0.5-1.5. Fixed wavelength scans were recorded using a bandwidth of 2 nm, a data interval of 1 nm and an integration time of 10 s.

3.2.5 High Performance Liquid Chromatography (HPLC)

HPLC analysis was carried out using an Agilent 1100 series LC equipped with variable wavelength UV detection (VWD) operating at 254 nm. Stock solutions were prepared at a concentration of approximately 1 mg/mL before being sufficiently diluted by a factor of 10 to reach the required sample concentration of 0.1 mg/mL.

Table 3.2: HILIC HPLC Conditions.

Flow Rate (mL/min)	1
UV Detection (nm)	254
Mobile Phase Composition	A: 20 mM Ammonium Formate, 95% H_2O: 5% MeCN B: 20 mM Ammonium Formate, 5% H_2O: 95% MeCN Isocratic 100% B
Column	HiChrom ACE 5 SIL, 150 x 4.6 mm i.d

3.2.6 Liquid Chromatography Mass Spectrometry (LC-MS)

LC-MS was carried out using a Thermo Fisher Scientific Linear Trap Quadrupole (LTQ) Orbitrap mass spectrometer operating in electrospray ionisation (ESI) positive ion mode. The samples were prepared in exactly the same manner as described above in 3.2.5.

Table 3.3: LC-MS operating conditions.

Flow Rate (mL/min)	0.3
Injection Volume (µl)	10
Mobile Phase Composition	A: 20 mM Ammonium Formate, 95% H_2O: 5% MeCN B: 20 mM Ammonium Formate, 5% H_2O: 95% MeCN Isocratic 100% B
Method of Ion Generation	Electrospray

3.2.7 Nuclear Magnetic Resonance (NMR) Spectroscopy

NMR experiments were carried out using a two channel Bruker AVANCE III 500MHz spectrometer equipped with a 9.4 T Bruker UltraShield magnet and a PA BBO 500S2 smart probe operating under Top Spin 3.6.1. Samples were prepared by dissolving approximately 10 mg in 0.75 mL of methanol-d_4.

3.3 Results and Discussion

Previous work in this group has shown that the colour of PPD appears to become darker over time. In an attempt to quantify the change in colour, UV/Vis spectroscopy was used to monitor the absorbance over a period of 16 weeks. This study monitored three different PPD samples of varying concentrations as the concentrations required to yield the required absorbance value was not known (Figure 3.2). The main trend that can be observed is that the absorbance values continually increase over the first twelve weeks, before starting to level off for the remainder of the time. Care was taken to ensure that evaporation from the volumetric flask did not occur by stoppering and sealing with parafilm. This increase in absorbance suggests that over the course of the first twelve weeks, PPD was reacting with itself which contributed to the evolution of the colour over time. After twelve weeks, the absorbance plateaued which indicated that the levels of reaction product had reached equilibrium. A major caveat to our observations was that after six-twelve weeks, the absorbance values were outside the required range (0.5-1.5) for UV/Vis analysis. This was done on purpose to limit the number of experimental variables as dilution may have affected the rate of reaction in our system. Whilst we are not able to reliably gain any properties of the molecule, *e.g.* A_1^1, concentration, *etc.*, the changes in absorbance warranted further investigation using other analytical techniques.

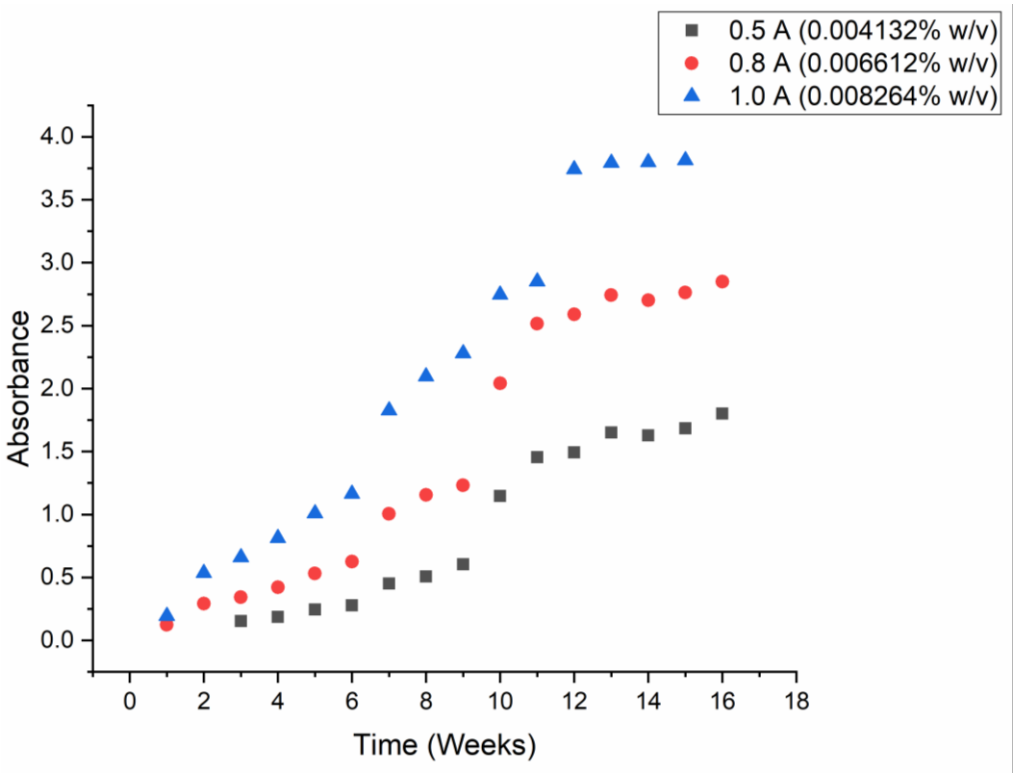

Figure 3.2: Change in the UV/Vis absorbance of three different concentrations of PPD in methanol monitored over sixteen weeks.

3.3.1 HPLC Method Development

We chose High Performance Liquid Chromatography (HPLC) to investigate the stability of PPD and the salt forms. HPLC has been the chromatographic technique of choice for the separation of dye intermediates used in commercial hair products due to its high sensitivity, specificity and precision.[13] The majority of reported PPD HPLC methods have utilised reversed phase HPLC to separate PPD in permanent hair colouring products.[14] Other methods, such as LC-MS have been shown to be an effective method to study the reactivity and oxidative transformation of PPD.[5,8] One separation mode that has not been used in the investigation of PPD is HILIC. HILIC has great potential for use in this system due to its polar nature, hence the separation of more polar molecules, *e.g.* peptides, nucleic acids and carbohydrates.[12] HILIC has never been previously used to separate PPD hence we needed to develop a method that would be applicable to PPD.

HPLC method development was carried out to determine if our separation was deemed acceptable for stability studies. To begin with, we decided to start with a gradient method to ascertain the retention time of PPD. After preliminary results were obtained and the approximate retention times of the peaks were known, we moved onto an isocratic method as there was no benefit of continuing with a gradient method since both peaks had eluted within 3 minutes with very little change in the mobile phase at this point, so it made sense to keep the mobile phase composition unchanged, *i.e.* an isocratic separation. From a visual inspection of the chromatogram, it can be observed that both peaks appear to be well separated and have good peak shape. In method development, one of the main goals is the selection of separation conditions which provide a good separation for the chosen sample. This can be described in terms of resolution with a value greater than or equal to two being required for baseline separation.[15] The resolution for our separation was calculated using equation 3.1 and was determined to be 2.78, this is above the required value of two indicating that we have adequate separation of both peaks.

The column efficiency given by the plate number (N) is another important factor in method development. The larger the value of N, the narrower the peaks and the better the separation. The values of N were calculated to be 5667 plates and 6926 plates respectively using equation 3.2 with the recommended value being around 12,000-15,000 plates based on our column dimensions. Reasons for lower plate numbers could be down to extra column peak broadening which is something that could be investigated through varying the column conditions, *e.g.* particle size, flow rate and column length.[15]

$$Rs = \frac{2[t_{R(j)} - t_{R(i)}]}{W_i + W_j} \quad \text{Eqn. 3.1}$$

$$N = 5.54\left(\frac{t_R}{W_{1/2}}\right)^2 \quad \text{Eqn. 3.2}$$

The values for both the retention times and peak widths in minutes were taken from the fresh chromatogram shown below in Figure 3.3. The obtained values indicated that our first attempts at producing an adequate separation were successful, although the efficiency of the chromatographic system may not be high as we would have liked.

3.3.2 HPLC/LC-MS/NMR Analysis

The results from our HPLC-UV studies are shown below in Figure 3.3 and show how PPD changes over a period of time. The HPLC reveals that a freshly prepared sample of PPD (less than 10 minutes from preparation) shows two peaks eluting at 1.92 minutes and 2.48 minutes. This indicates that either the solid that was used to create the solutions was not pure or that the reactivity of PPD is extremely high. We have confirmed from PXRD and NMR analysis that the solid from the bottle was pure albeit that the solid did have a pink hue indicating that there had been some oxidation. After fourteen days, two observations can be made. Firstly, there is a significant shift to longer retention times of both peaks. Secondly, there is a new peak at approximately 2.28 minutes. The shift of the retention times could be due to two factors: i) a change in the mobile phase composition-or, ii) a change in the chemistry of the column. For each of the measurements, a fresh mobile phase was used using the same batch of acetonitrile hence we have tried to reduce the experimental errors through this route. As far as the lifetime of the column is concerned, it has been reported that 500-2000 injections is considered satisfactory.[16] The column that was used for this study has had fewer injections (max 200-250), so this is unlikely to be the cause. Using the HPLC-UV method, we had no indication as to the identities of these peaks apart from the assumption that one of them was that of PPD and that the peak at 1.92 minutes (fresh) and 2.09 minutes (14 days) were the same product.

To enable us to characterise the compounds eluting at 1.92 and 2.48 minutes, LC-MS was chosen as mass spectrometry has been reported as a method to characterise the oxidation products of PPD.[4]

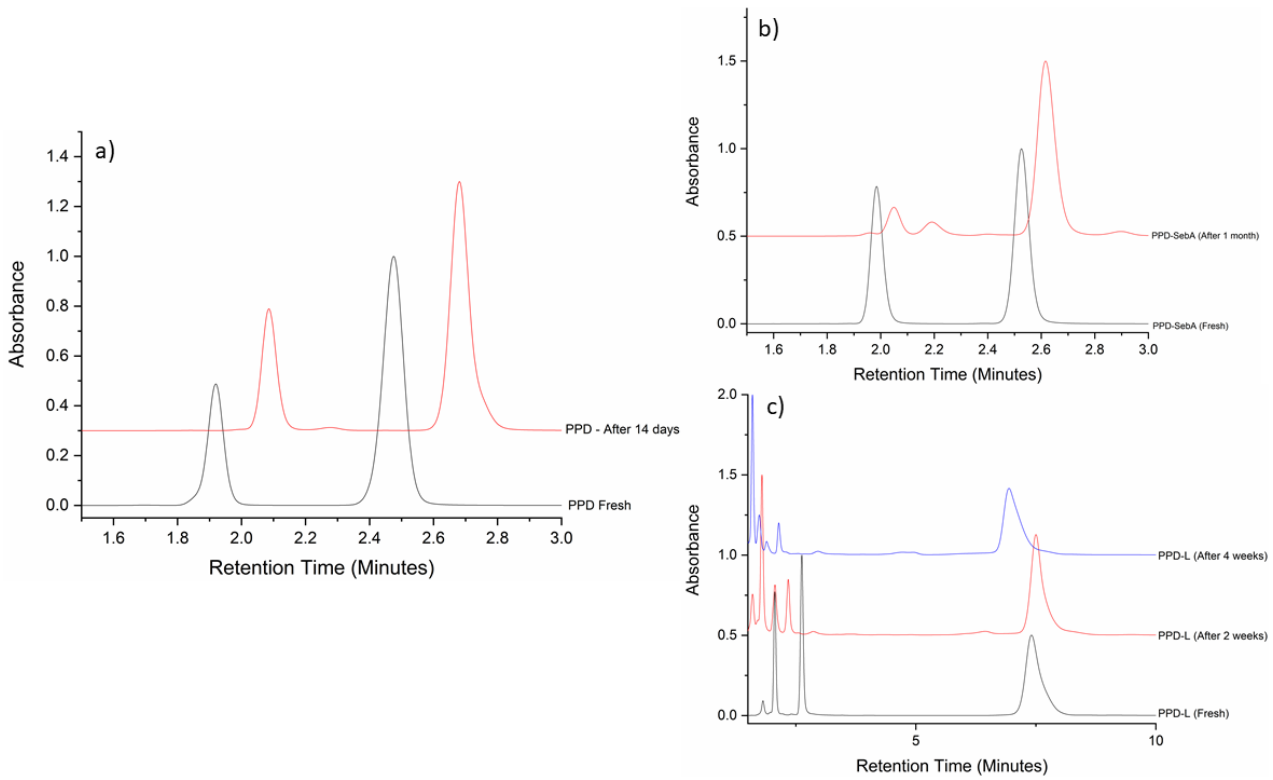

Figure 3.3: a) The HPLC-UV chromatograms of PPD monitored over 14 days; b) and c) the HPLC-UV chromatograms of PPD-SebA and PPD-L monitored over 4 weeks.

For the LC-MS experiment, two samples of PPD (80:20 MeCN: H_2O v/v, 0.1 mg/mL) were prepared, one fresh and one after 24 hours. Due to a lower flow rate being used in the MS, the retention times for the main peaks occur at longer retention times of 6.35 minutes and 6.26 minutes respectively compared to the HPLC results. The LC-MS chromatograms of the peaks eluting at 6.35 minutes and 6.26 minutes shows that these peaks correspond to the ions in the MS spectrum at approx. 213 mass units which is thought to be the formation of a dimer as its been reported that PPD undergoes oxidation reactions leading to the generation of dimeric, trimeric and polymeric derivatives.[1,4] It can also be observed that in addition to the peak at 213 mass units, the peak at a *m/z* of 133.08 is present in both samples which has not been previously reported in the literature and with 25 mass units greater than PPD which could potentially be *p*-toluenediamine (PTD) with an additional methyl group. In the fresh sample, there is a peak at a *m/z* of 320.15 which has been suggested to be a trimer of PPD with an additional OH group. The fact that PPD does not appear to be present in its pure form and also the presence of several ions of high molecular weight indicates that PPD has undergone oxidation.[1] The ions observed only in the sample after 24 hours at a *m/z* of 283 and 431 do not correspond with any of the known oxidation products of PPD making it very difficult to determine what these products are as we know that PPD reacted with itself in the MS.

Table 3.4: The suspected oxidation products of PPD with the mass units listed above for the p-toluenediamine (PTD) derivative (m/z 133.08), suspected dimer of PPD (m/z 213.11) and suspected trimer of PPD (m/z 320.15)

m/z 133.08	*m/z* 213.11
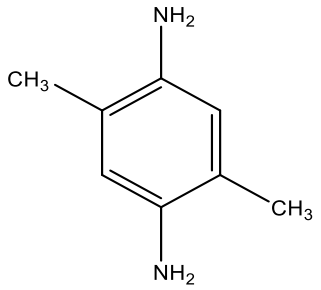	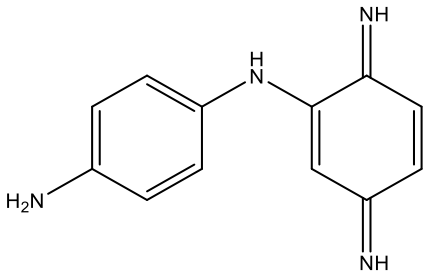
m/z 320.15	
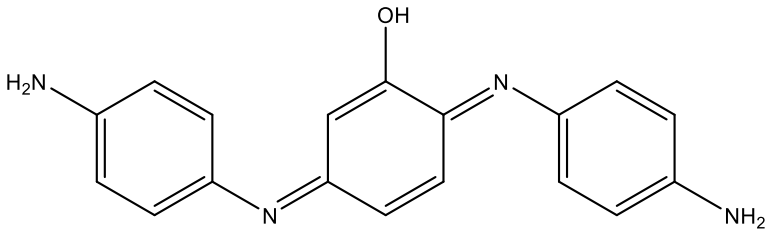	

Figure 3.4: a) The LC-MS chromatogram of a fresh sample of PPD with the corresponding mass spectrum for the peak eluting at 6.35 minutes; b) the LC-MS chromatogram of a PPD sample after 24 hours with the corresponding mass spectrum for the peak eluting at 6.26 minutes.

^{1}H NMR was investigated in an attempt to gain more information on the degradants of PPD. The fresh ^{1}H NMR spectrum of PPD (Figure 3.5) shows two peaks at 3.33 ppm and 4.86 ppm respectively which corresponds to the solvent in this case methanol-d_4. There is only one signal observed in the aromatic region of the spectrum (approx. 6.5-8.0 ppm) which is what we would expect to see as the molecule is symmetrical meaning that all of the aromatic protons are equivalent resulting in one signal. This result, unlike the HPLC and LC-MS data indicates that the material is in fact pure and it should be noted that this spectrum was acquired within 30 minutes of preparation of the sample.

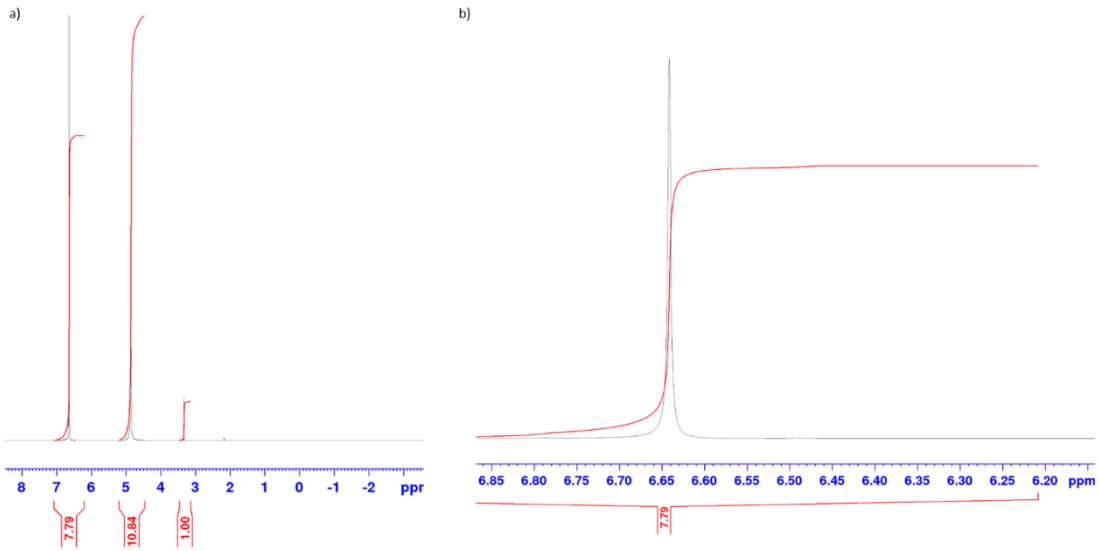

Figure 3.5: a) The ^{1}H NMR spectrum of a fresh sample of PPD acquired in methanol-d_4; b) an enlarged view of the aromatic region of the spectrum.

From a visual inspection of the fresh sample (bottom trace) (Figure 3.6) with the subsequent spectrums, it is clear that the sample is undergoing substantial changes. In an attempt to better understand the nature of PPD's reactivity in solution, simulated ^{1}H NMR's were generated for the suspected oxidation products identified in Table 3.4. From the simulated NMR's, the majority of the peaks are in the region of 5-10 ppm, so we will focus on this range, although there is a peak at approx. 4.2 ppm which is not in the fresh sample most likely due to the amine group of the dimer which isn't normally observed experimentally. The peaks for the suspected dimer/trimer in the simulated NMR's between 9-11 ppm are not observed experimentally, most likely as these peaks correspond to the NH groups in the dimer and the OH groups in the trimer. The sharp signal observed at approx. 5.80 ppm is thought to be attributed to the suspected dimer and is not shifted downfield as a result of neighbouring functional groups. The intense signal observed at approx. 7.6 ppm is not present in any of the suspected oxidants, unless it is the peak at approx. 7.3 ppm which has been shifted further downfield than calculated. From the experimental NMR data and

comparison with the simulated NMR's, it is very difficult to determine what peaks are attributed to what compound.

The PPD-SebA and PPD-L salt forms will be discussed in terms of their reactivity in solution by HPLC and NMR and compared with the results to that of pure PPD to ascertain whether the salt forms help stabilise PPD.

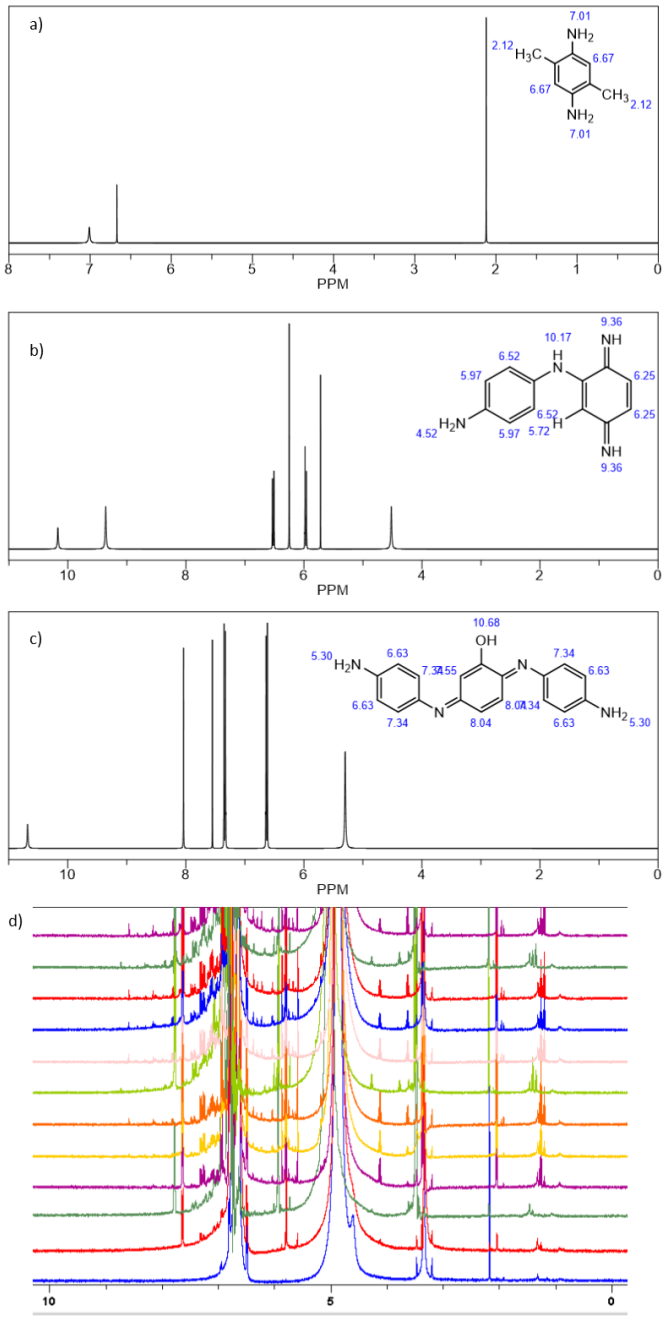

Figure 3.6: a), b) and c) The simulated NMR spectrums of the suspected oxidation products with a *m/z* of 133.08, 213.11 and 320.15 respectively; d) stacked ^{1}H NMR of PPD monitored over 12 weeks with the spectrum at the bottom being a freshly prepared sample, the red spectrum (after one week), the green spectrum (after four weeks) and each subsequent spectrum being collected every two weeks up to 12 weeks (top spectrum)

From HPLC analysis of the salt forms (Figure *3.3*), it is clear that there is significant peak shifting as well as the appearance of new peaks, similar to that observed with pure PPD. Unfortunately, we do not have LC-MS data for the salt forms to help us identify the potential degradants. HPLC analysis shows very similar behaviour to PPD and so we would expect the NMR of the salt forms to be very similar in terms of reactivity to that of PPD. The NMR of the sebacate salt (Figure *3.7*) shows significant changes in the aromatic region including a singlet at approx. 8.5 ppm, a cluster of peaks at approx. 8 ppm and another cluster of peaks at approx. 6 ppm. Comparison of the sebacate salt with pure PPD after approx. 12 weeks which is the top spectrum in Figure *3.7*, shows that the singlet at approx. 8.5 ppm and the cluster of peaks at approx. 8 ppm are also present in the spectrum of PPD after approx. 12 weeks. This data suggests that the sebacate salt follows the same reaction pathway as PPD. The NMR of the PPD-L (1:2) salt (Figure 3.8) appears to be more stable over time and does not show as much change in the aromatic region as the sebacate salt and pure PPD indicating in this case that salt formation may help stabilise PPD.

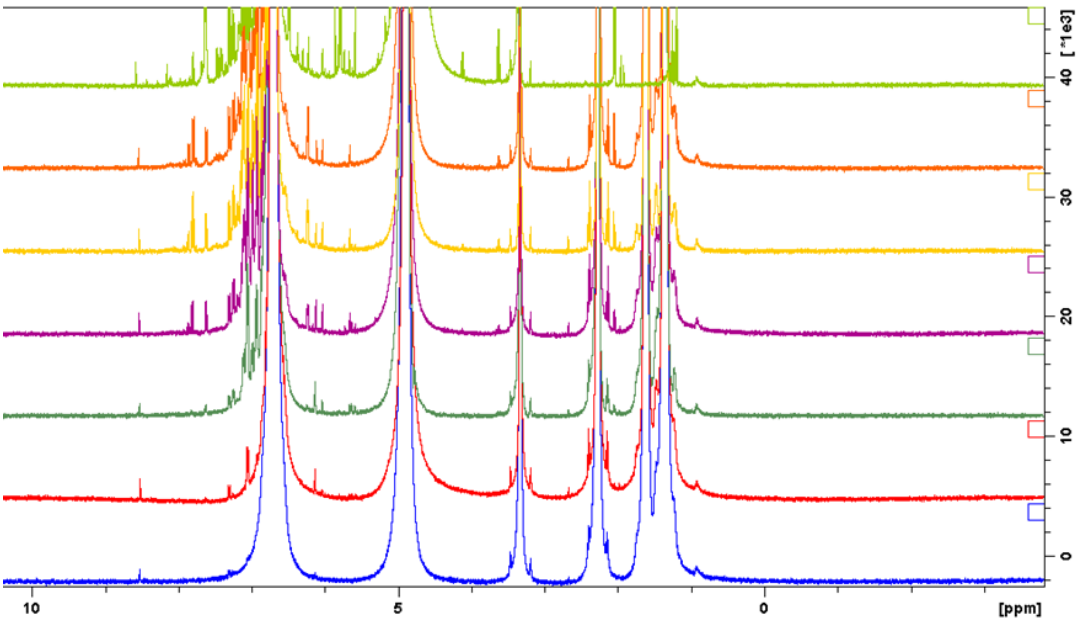

Figure 3.7: Stacked ^{1}H NMR of PPD-SebA (2:1) monitored over four weeks with the spectrum at the bottom being a freshly prepared sample, the red spectrum (after 24 hrs), the green spectrum (after 7 days) and each subsequent spectrum being collected weekly with the top spectrum being PPD after approx. 12 weeks for comparison.

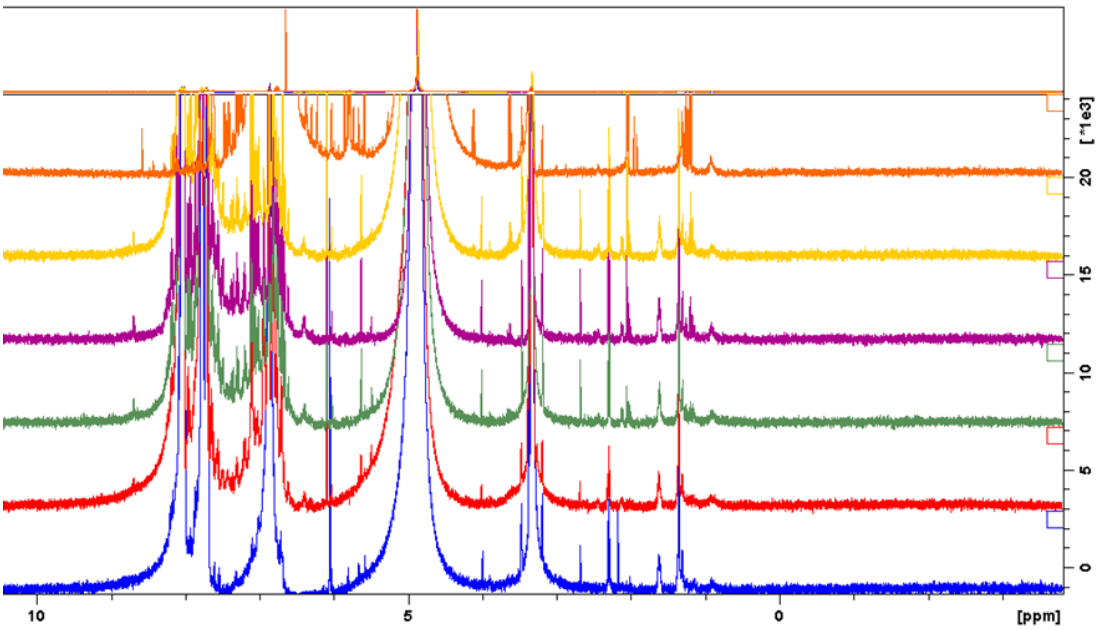

Figure 3.8: Stacked ^{1}H NMR of PPD-L (1:2) monitored over four weeks with the spectrum at the bottom being a freshly prepared sample, the red spectrum (after 7 days) and each subsequent spectrum being *collected weekly with the top spectrum being PPD after approx. 12 weeks for comparison.*

3.4 Conclusions

This work has studied the reactivity of both PPD and its salt forms in solution. We have seen how the colour of a pure PPD solution changes over time as a result of oxidation which resulted in the formation of suspected dimers/trimers through HPLC-UV/LC-MS and NMR analysis. The change in colour over time is a result of the reactions PPD undergoes with itself resulting in dimer/trimer formation which features more conjugation in turn increasing the complexity of the NMR's. The main aim of this work was to investigate whether the formation of a salt form of PPD would help stabilise PPD over PPD in its pure form. Our results suggest that for PPD-SebA (2:1), this salt shows significant changes over time, much like PPD with the NMR indicating that the degradants formed are similar to PPD. In comparison, the PPD-L (1:2) salt shows far less reactivity by NMR and suggests that salt formation may help stabilise PPD in this case, however, the mechanism is still unknown.

3.5 References

1. Zanoni, T. B., Hudari, F., Munnani, A., Peluso, M., Godschalk, R. W., Zanoni, M. V. B., Den Hartog, G. J. M., Bast, A., Barros, S. B. M., Maria-Engler, S. S., Hageman, G. J & De Oliveira, D. P. The oxidation of *p*-phenylenediamine, an ingredient used for permanent hair dyeing purposes, leads to the formation of hydroxyl radicals: Oxidative stress and DNA damage in human immortalized keratinocytes. *Toxicol. Lett.* **239**, 194–204 (2015).

2. He, J., Sunarso, J., Miao, J., Sun, H., Dai, J., Zhang, C, Zhou, W & Shao, Z. A highly sensitive perovskite oxide sensor for detection of *p*-phenylenediamine in hair dyes. *J. Hazard. Mater.* **369**, 699–706 (2019).

3. Meyer, A., Blomeke, B. & Fischer, K. Determination of *p*-phenylenediamine and its metabolites MAPPD and DAPPD in biological samples using HPLC-DAD and amperometric detection. *J. Chromatogr. B-Analytical Technol. Biomed. Life Sci.* **877**, 1627–1633 (2009).

4. Fischer, K., Hoffler, S., Wacht, M. & Meyer, A. Hplc Separation of Aryldiamine Transformation Products Using a Polar-Modified Rp-C-18 Column. *Anal. Lett.* **46**, 2673–2689 (2013).

5. Meyer, A. & Fischer, K. Oxidative transformation processes and products of para-phenylenediamine (PPD) and para-toluenediamine (PTD)-a review. *Environ. Sci. Eur.* **27**, (2015).

6. Kim, K. H., Kabir, E. & Jahan, S. A. The use of personal hair dye and its implications for human health. *Environ. Int.* **89**–**90**, 222–227 (2016).

7. Aeby, P., Sieber, T., Beck, H., Gerberick, G. F. & Goebel, C. Skin Sensitization to *p*-phenylenediamine: The Diverging Roles of Oxidation and N-Acetylation for Dendritic Cell Activation and the Immune Response. *J. Invest. Dermatol.* **129**, 99–109 (2009).

8. Jahn, S., Faber, H., Zazzeroni, R. & Karst, U. Electrochemistry/mass spectrometry as a tool in the investigation of the potent skin sensitizer *p*-phenylenediamine and its reactivity toward nucleophiles. *Rapid Commun. Mass Spectrom.* **26**, 1453–1464 (2012).

9. Marcoux, D., Couture-Trudel, P. M., Riboulet-Delmas, G. & Sasseville, D. Sensitization to para-phenylenediamine from a streetside temporary tattoo. *Pediatr. Dermatol.* **19**, 498–502 (2002).

10. Delori, A., Urquhart, A. J. & Oswald, I. D. H. Supramolecular hair dyes: A new application of cocrystallization. *CrystEngComm* **18**, 5360-5364 (2016).

11. Hemstrom, P. & Irgum, K. Hydrophilic interaction chromatography. *J. Sep. Sci.* **29**, 1784–1821 (2006).

12. Janvier, S. , De Sutter, E., Wynendaele, E., De Spiegeleer, B., Vanhee, C & Deconinck, E. Analysis of illegal peptide drugs via HILIC-DAD-MS. *Talanta* **174**, 562–571 (2017).

13. Ghosh, P. & Sinha, A. Hair Colors: Classification, Chemistry and a Review of Chromatographic and Electrophoretic Methods for Analysis. *Anal. Lett.* **41**, 2291–2321 (2008).

14. Narita, M., Murakami, K. & Kauffmann, J. M. Determination of dye precursors in hair coloring products by liquid chromatography with electrochemical detection. *Anal. Chim. Acta* **588**, 316–320 (2007).

15. Snyder Kirkland, J and Dolan, W, L. *Introduction to Modern Liquid Chromatography*. (John Wiley & Sons, 2010).

16. Moldoveanu, S. C. & David, V. General Aspects Regarding the HPLC Analytical Column. in *Selection of the HPLC Method in Chemical Analysis* 231–277 (Elsevier, 2017).

Chapter Four – Structural Changes and Ionisation of PPD

4 Structural Changes and Ionisation of PPD

The aims/goals of this chapter are to expand on the work done on PPD in Chapter 3 by investigating the effect that small structural changes will have on the resultant colour which will be investigated using co-crystallisation of *o*-phenylenediamine, *m*-phenylenediamine and 4-iodoaniline. Based on the PPD reactivity, *o*-phenylenediamine and *m*-phenylenediamine will also be investigated for their reactivity. The use of ionic co-crystals of PPD will be investigated to determine how ionisation effects the colour and reactivity of PPD.

4.1 Introduction

Diaminobenzenes, also referred to as phenylenediamines (PDs) are aromatic amines which are an important family of compounds with interest in biological and materials science with PDs being the main components in permanent hair dyes.[1-2] *o*-Phenylenediamine (OPD), *m*-phenylenediamine (MPD) and *p*-phenylenedamine (PPD) are isomers which are used as precursors or chemical intermediates in the production of plastics, industrial dyes and photosensitive materials.[3] When in contact with air or oxidising agents, *i.e.* peroxides, PDs are known to transform into mixtures of monomeric, dimeric and polymeric oxidation products.[4] In Chapter 3 and in previous literature, we observed that co-crystallisation of PPD caused a change in the colour of solution and we were able to use the colour swatches of hair. In this chapter, we will investigate the impact small structural changes to PPD would have on the resultant colour of the solution. This has been enabled by the use of isomers of PPD in the co-crystallisation experiments, but also through the exploration of other methods, *e.g.* use of ionic co-crystals. The use of different methods and components was an attempt to probe the underlying requirements to observe the deep coloured solution so that future studies could be directed towards successful outcomes.

Co-crystallisation, also referred to as multi-component crystallisation is the approach of combining two or more distinct molecules in the crystal structure forming a salt or molecular complex.[5] This approach has gained interest from industry and academics as it allows for the physiochemical properties of active pharmaceutical ingredients (APIs) to be altered including hygroscopic stability, solubility and bioavailability, intrinsic dissolution rate, thermal properties, compressibility, *etc.*[6] This enhancement of the physiochemical properties can be achieved through the formation of multi-component molecular complexes, *i.e.* co-crystals or through polymorphic forms of an API.[7] Co-crystals can be classed as multi-component crystals comprised of two or more neutral building blocks present in a definite stoichiometric ratio held together through non-covalent interactions and which are solids at ambient conditions.[8-9] An important sub-group within the co-crystal family is that of ionic co-crystals (ICCs) which are defined as multi-component solid forms comprised of neutral

organic molecules and salts in a definite stoichiometric ratio.[10-11] The use of pharmaceutically acceptable inorganic salts as co-formers, *e.g.* alkaline and alkali earth halides, provides additional routes of modifying the APIs physical and chemical properties through the formation of ionic co-crystals.[12] When the co-former is that of an inorganic salt, the interaction formed between the metal cations in the inorganic-organic ICCs is the type seen in solvated crystalline materials.[13] There are many solid-state properties which can be altered through co-crystallisation of organic APIs and inorganic co-formers including the preparation of co-crystals using the inorganic salts, $MgCl_2$ and $CaCl_2$ which has been shown to improve the hygroscopicity, crystal morphology and thermal stability in comparison to the pure drugs.[14]

The three components that were used to investigate changes to structure were the isomers *o*-phenylenediamine (OPD) and *m*-phenylenediamine (MPD) as well as 4-iodoaniline (4IODAN). The isomers were included to investigate the impact on the ability for resonance stabilisation of the ring system whilst 4-iodoaniline was chosen to alter the electronic properties of the amine component. Previous studies of *o*-phenylenediamine (OPD) has two reported polymorphic forms[15], as well as a range of multi-component forms including salts[16], co-crystals[17] and co-crystal hydrates.[18] OPD was first reported by Stalhandske in 1981, however, there are no details as to the preparation of this form in the literature. A second polymorph has been reported more recently which was discovered during attempted co-crystallisation experiments with phenazine via slow evaporation of a methanol-diethyl ether (1:1 v/v) solution. This polymorph was observed concomitantly with a new phenazine co-crystal and this new polymorph was only observed on one occasion.[15] *m*-Phenylenediamine (MPD) has only one reported crystal form along with a series of inorganic salts.[19-20] 4-iodoaniline (4IODAN) has only one reported crystal form with several co-crystals/salts reported which also includes solvated forms with these materials which exhibit molecular disorder favouring layered, coloured crystals, whereas proton transfer results in completely colourless ionic species.[21–23] OPD/MPD were chosen for co-crystallisation experiments as previous work in our group had investigated salt formation of *p*-phenylenediamine (PPD) which resulted in a series of deeply coloured complexes.[24]

In this study, the main aims were to investigate the impact small structural changes to PPD would have on the resultant colour. Firstly, the impact of creating ionic co-crystals will be surveyed. Secondly, the effect of position of substitution will be analysed through the use of isomers. Lastly, the effect of altering the electronic withdrawing power on the system will be investigated using 4-iodoaniline. In each case, solution and mechanochemcal preparation routes will be used and the results investigated using X-ray diffraction and thermal techniques.

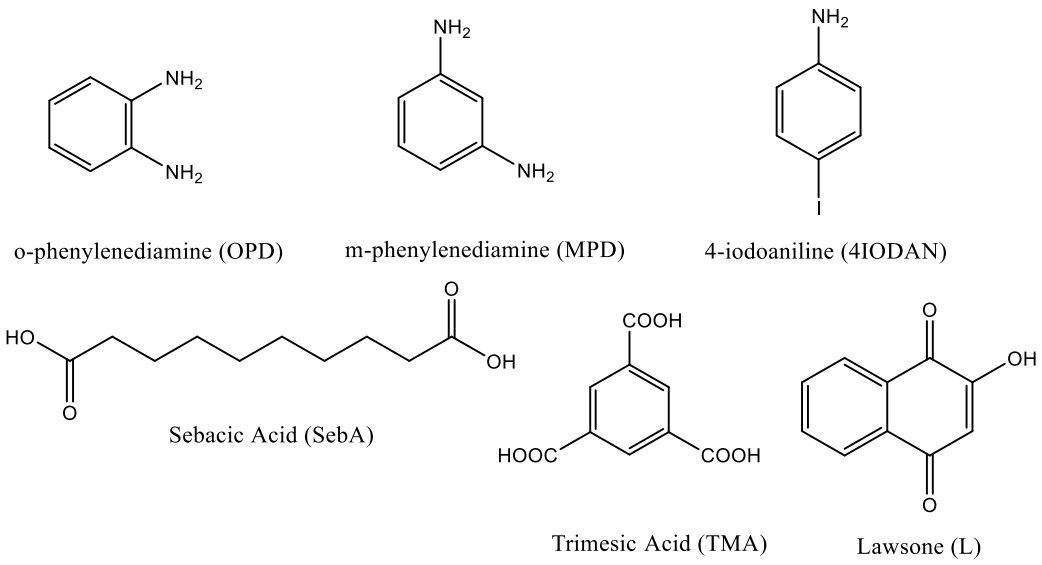

Scheme 4.1: Chemical structures of the APIs used in co-crystallisation experiments with the co-formers SebA, TMA and L.

4.2 Materials & Methods

4.2.1 Materials

o-Phenylenediamine (OPD, purity ≥98%, Lot No: SLBB0408V), *m*-phenylenediamine (MPD, purity 99%, Lot No: WXBC7196V), 4-iodoaniline (4IODAN, purity 98%, Lot No: STBF1093V), sebacic acid (SebA, purity 99%, Lot No: MKBR6472V) and lawsone (L, purity 97%, Lot No: STBD5846V) were obtained from Sigma-Aldrich. Trimesic acid (TMA, purity 98%, Lot No: 10219393) was obtained from Alfa Aesar. Methanol (Anala NORMAPUR, purity ≥99.8%) was obtained from VWR Chemicals. All materials were used as received without any further purification.

4.2.2 Liquid Assisted Grinding (LAG) Experiments

LAG experiments were carried out using a Retsch MM400 mechanical mill equipped with 10 mL stainless steel grinding jars and two 7 mm steel balls per jar. A small quantity of solvent (approx. 50 μL) was added and the milling process was carried out at a frequency of 30 Hz for 30 minutes (except for the ionic co-crystals which were additionally milled for 45 and 60 minutes). For the 4IODAN series, a few drops of solvent was added to the reaction mixture and ground for 15 minutes in a mortar and pestle.

Table 4.1: List of weights of each component used in co-crystallisation experiments of OPD/MPD.

	Weight of API (mg; mmol)	Weight of Co-Former (mg; mmol)
OPD-SebA	111.4; 1.030	201.5; 0.996
OPD-TMA	113.1; 1.046	216.1; 1.028
OPD-L	112.4; 1.039	178.8; 1.027
MPD-S	110.9; 1.026	214.7; 1.062
MPD-TMA	111.5; 1.031	212.7; 1.012
MPD-L	115.1; 1.064	178.8; 1.027
4IODAN-SebA	221.7; 1.012	201.4; 0.996
4IODAN-TMA	221.0; 1.009	218.1; 1.038
4IODAN-L	229.6; 1.048	174.4; 1.001
PPD2HCl-SebA	183.2; 1.012	104.7; 0.518
PPD2HCl-TMA	188.5; 1.041	109.3; 0.520

4.2.3 Cooling Crystallisation

OPD-TMA (LAG): Approximately 50 mg of ball milled powder created by procedure in 4.2.2 was dissolved in 0.5 mL of methanol. The solution was heated from 15 °C to 50 °C at a rate of 0.5 °C/min followed by cooling to 15 °C at a rate of 0.2 °C/min. The sample crystallised as greyish blocks of suitable quality for single crystal X-ray diffraction.

MPD-TMA (LAG): Approximately 50 mg of ball milled powder created by procedure in 4.2.2 was dissolved in 0.5 mL of methanol. The solution was heated from 15 °C to 50 °C at a rate of 0.3 °C/min, held at constant temperature (50 °C) for 60 minutes and cooled to 15 °C at a rate of 0.3 °C/min. The sample crystallised as greyish plates of suitable quality for single crystal X-ray diffraction.

MPD-L (LAG): Approximately 50 mg of ball milled powder created by procedure in 4.2.2 was dissolved in 0.5 mL of methanol. The solution was heated from 15 °C to 50 °C at a rate of 0.3 °C/min followed by cooling to 15 °C at a rate of 0.3 °C/min. The crystal habit/size were not recorded, however the crystals obtained were suitable for single crystal X-ray diffraction.

4.2.4 Evaporative Crystallisation

OPD-SebA: Roughly equimolar quantities of OPD (12.1 mg, 0.112 mmol) and SebA (23.0 mg, 0.114 mmol) were dissolved in 5 mL of isopropyl alcohol and left to slowly evaporate at 23 °C. The sample crystallised after approximately four weeks as brown plates of suitable quality for single crystal X-ray diffraction.

OPD-L: Roughly equimolar quantities of OPD (16.6 mg, 0.154 mmol) and L (29.4 mg, 0.169 mmol) were dissolved in 5 mL of methanol and left to slowly evaporate at 23 °C. The sample crystallised after several hours as red needles of suitable quality for single crystal X-ray diffraction.

4IODAN-TMA: Roughly equimolar quantities of 4IODAN (26.0 mg, 0.119 mmol) and TMA (21.3 mg, 0.101 mmol) were dissolved in 5 mL of methanol and left to slowly evaporate in a darkened cupboard at approximately 19 °C. The sample crystallised after approximately four weeks as greyish plates of suitable quality for single crystal X-ray diffraction.

4IODAN-L: Roughly 2:1 molar quantities of 4IODAN (56.4 mg, 0.258 mmol) and L (24.2 mg, 0.139 mmol) were dissolved in 5 mL of methanol and slowly evaporated in a darkened cupboard at 19 °C. The sample crystallised after approximately one week as dark red needles of suitable quality for single crystal X-ray diffraction.

PPD-HCl: An amount of PPD (20.9 mg, 0.193 mmol) was dissolved in 5 mL of 1 M hydrohloric acid and slowly evaporated in the fume cupboard at approximately 19 °C - 22 °C. The sample crystallised after approximately two weeks as colourless blocks of suitable quality for single crystal X-ray diffraction.

4.2.5 Single Crystal X-ray Diffraction (SCXRD)

Single crystals were selected using a Leica M165 CX microscope and silicone oil was used as an adhesive to aid in mounting the single crystals. Diffraction data was collected on a Bruker Kappa Apex II Duo using Mo-Kα radiation (λ = 0.71073 Å) and a Bruker D8 Venture using Cu-Kα radiation (λ = 1.5406 Å). Both instruments were equipped with an Oxford cryosystems low temperature device operating at −173.13 °C.[25] Data reduction was performed using Bruker SAINT[26] and a multi-scan absorption correction was applied using SADABS[27]. The crystal structures were solved in Olex2[28] using SHELXT[29] and the model refined by full-matrix least squares against F^2 using all data (SHELXL[30]). All non-hydrogen atoms were refined anisotropically and the hydrogen atoms attached to carbon, oxygen and nitrogen were placed geometrically.

Table 4.2: Crystallographic data and structure refinement parameters for the PPD HCl Salt.

	ppd_hcl_01_0m
Chemical formula	$2(Cl)\cdot C_6H_{10}N_2$
M_r	181.06
Crystal system, space group	Triclinic, $P\bar{1}$
Temperature (°C)	23.85
a, *b*, *c* (Å)	4.3369(8), 5.8407(12), 8.6145(16)
α, *β*, *γ* (°)	70.763(7), 77.093(7), 80.326(8)
V (Å^3)	199.76(7)
Z	1
Radiation type	Cu-*Kα*
μ (mm^{-1})	6.69
Crystal size (mm)	0.26 × 0.12 × 0.04
Diffractometer	Bruker D8 Venture
Absorption correction	Multi-scan *SADABS2016*/2 (Bruker,2016/2) was used for absorption correction. w*R*2(int) was 0.0938 before and 0.0469 after correction. The Ratio of minimum to maximum transmission is 0.6782. The *λ*/2 correction factor is Not present.
T_{min}, T_{max}	0.511, 0.753
No. of measured, independent and observed [$I > 2\sigma(I)$] reflections	1505, 678, 671
R_{int}	0.031
$(\sin \vartheta/\lambda)_{max}$ (Å^{-1})	0.610
$R[F^2 > 2\sigma(F^2)]$, $wR(F^2)$, S	0.052, 0.132, 1.17
No. of reflections	678
No. of parameters	47
H-atom treatment	H-atom parameters constrained
$\Delta\rho_{max}$, $\Delta\rho_{min}$ (e Å^{-3})	0.49, −0.63

Table 4.3: Selected hydrogen bond parameters for the PPD HCl Salt.

D—H···*A*	*D*—H (Å)	H···*A* (Å)	*D*···*A* (Å)	*D*—H···*A* (°)
N1—H1A···Cl1^{i}	0.89	2.30	3.174 (2)	165.8
N1—H1B···Cl1^{ii}	0.89	2.35	3.194 (2)	159.1
N1—H1C···Cl1	0.89	2.36	3.247 (2)	172.0

Table 4.4: Crystallographic data and structure refinement parameters for the OPD series.

	mo_opd_seba_01_0m	opd_tma_bm_100k_120919_0m	opd_l_100k_200919_0m
Chemical formula	$C_{10}H_{16}O_4 \cdot 2(C_6H_9N_2)$	$C_9H_3O_6 \cdot C_6H_9N_2$	$C_{16}H_{10}N_2O$
M_r	418.53	316.27	246.26
Crystal system, space group	Triclinic, $P\bar{1}$	Monoclinic, $C2/c$	Monoclinic, $P2_1/c$
Temperature (°C)	22.85	−173.13	−173.13
a, b, c (Å)	6.2966(12), 8.2640(14), 22.360(4)	29.583(10), 15.224(4), 6.881(2)	13.6526(11), 4.7020(4), 17.9786(15)
α, β, γ (°)	87.599(6), 85.992(7), 88.700(7)	90, 93.880(12), 90	90, 100.167(5), 90
V (Å^3)	1159.4(4)	3091.8(16)	1136.00(16)
Z	2	8	4
Radiation type	Mo-$K\alpha$	Mo-$K\alpha$	Mo-$K\alpha$
μ (mm^{-1})	0.08	0.11	0.09
Crystal size (mm)	0.28 × 0.11 × 0.06	0.28 × 0.15 × 0.06	0.31 × 0.02 × 0.02
Diffractometer	Bruker *APEX*-II CCD	Bruker *APEX*-II CCD	Bruker *APEX*-II CCD
Absorption correction	Multi-scan *SADABS2016*/2 (Bruker,2016/2) was used for absorption correction. w$R2$(int) was 0.1534 before and 0.0981 after correction. The Ratio of minimum to maximum transmission is 0.4291. The $\lambda/2$ correction factor is Not present.	Multi-scan *SADABS2016*/2 (Bruker,2016/2) was used for absorption correction. w$R2$(int) was 0.0992 before and 0.0699 after correction. The Ratio of minimum to maximum transmission is 0.8123. The $\lambda/2$ correction factor is Not present.	Multi-scan *SADABS2016*/2 (Bruker,2016/2) was used for absorption correction. w$R2$(int) was 0.1514 before and 0.0636 after correction. The Ratio of minimum to maximum transmission is 0.8109. The $\lambda/2$ correction factor is Not present.
T_{min}, T_{max}	0.320, 0.745	0.605, 0.745	0.604, 0.745
No. of measured, independent and observed [$I > 2\sigma(I)$] reflections	13872, 5342, 3693	10432, 2773, 2017	13906, 2018, 1445
R_{int}	0.061	0.043	0.064
$(\sin \vartheta/\lambda)_{max}$ (Å^{-1})	0.684	0.609	0.596
$R[F^2 > 2\sigma(F^2)]$, $wR(F^2)$, S	0.141, 0.406, 1.06	0.052, 0.162, 1.06	0.037, 0.099, 1.04
No. of reflections	5342	2773	2018
No. of parameters	275	210	173
H-atom treatment	H-atom parameters constrained	H-atom parameters constrained	H-atom parameters constrained
$\Delta\rho_{max}$, $\Delta\rho_{min}$ (e Å^{-3})	0.37, −0.48	0.52, −0.39	0.18, −0.17

Table 4.5: Crystallographic data and structure refinement parameters for the MPD series.

	mpd_tma_bm_100k_0m	mo_mpd_l_bm_01_0m
Chemical formula	$C_9H_5O_6 \cdot C_6H_9N_2$	$C_{10}H_5O_3 \cdot C_6H_9N_2$
M_r	318.28	282.29
Crystal system, space group	Triclinic, $P\bar{1}$	Monoclinic, $P2_1/c$
Temperature (°C)	−173.13	24.85
a, b, c (Å)	7.0861(19), 9.011(2), 11.212(3)	13.626(7), 4.103(2), 26.103(15)
α, β, γ (°)	80.101(7), 84.700(7), 82.952(7)	90, 100.53(3), 90
V (Å^3)	698.0(3)	1434.7(14)
Z	2	4
Radiation type	Mo-$K\alpha$	Mo-$K\alpha$
μ (mm^{-1})	0.12	0.09
Crystal size (mm)	0.28 × 0.08 × 0.04	N/A
Diffractometer	Bruker *APEX*-II CCD	Bruker *APEX*-II CCD
Absorption correction	Multi-scan *SADABS2016*/2 (Bruker,2016/2) was used for absorption correction. wR2(int) was 0.1026 before and 0.0430 after correction. The Ratio of minimum to maximum transmission is 0.8912. The $\lambda/2$ correction factor is Not present.	Multi-scan *SADABS2016*/2 (Bruker,2016/2) was used for absorption correction. wR2(int) was 0.0998 before and 0.0359 after correction. The Ratio of minimum to maximum transmission is 0.8268. The $\lambda/2$ correction factor is Not present.
T_{min}, T_{max}	0.664, 0.745	0.615, 0.744
No. of measured, independent and observed [$I > 2\sigma(I)$] reflections	8129, 2817, 2619	941, 651, 437
R_{int}	0.027	0.034
ϑ_{max} (°)	N/A	17.8
(sin $\vartheta/\lambda)_{max}$ (Å^{-1})	0.625	0.430
$R[F^2 > 2\sigma F^2)]$, $wR(F^2)$, S	0.073, 0.219, 1.24	0.090, 0.256, 1.05
No. of reflections	2817	651
No. of parameters	211	87
H-atom treatment	H-atom parameters constrained	H-atom parameters constrained
$\Delta\rho_{max}$, $\Delta\rho_{min}$ (e Å^{-3})	0.61, −0.48	0.24, −0.25

Table 4.6: Crystallographic data and structure refinement parameters for the 4IODAN series.

	4iodan_tma_100k_200919_0m	4iodan_l_100k
Chemical formula	$C_6H_7IN \cdot C_9H_5O_6 \cdot H_2O$	$C_{16}H_{10}INO_2$
M_r	447.17	375.15
Crystal system, space group	Monoclinic, $P2_1/c$	Orthorhombic, *Fdd*2
Temperature (°C)	−173.13	−172.13
a, b, c (Å)	3.9082(1), 32.0292(11), 12.7657(4)	23.3781(7), 56.2755(16), 3.9648(1)
α, β, γ (°)	90, 95.263(2), 90	90, 90, 90
V (Å^3)	1591.23(8)	5216.1(3)
Z	4	16
Radiation type	Mo-$K\alpha$	Cu-$K\alpha$
μ (mm^{-1})	2.05	19.30
Crystal size (mm)	0.18 × 0.04 × 0.02	0.22 × 0.02 × 0.02
Diffractometer	Bruker *APEX*-II CCD	Bruker D8 Venture
Absorption correction	Multi-scan *SADABS2016*/2 (Bruker,2016/2) was used for absorption correction. wR2(int) was 0.0568 before and 0.0318 after correction. The Ratio of minimum to maximum transmission is 0.8134. The $\lambda/2$ correction factor is Not present.	Multi-scan *SADABS2016*/2 (Bruker,2016/2) was used for absorption correction. wR2(int) was 0.1560 before and 0.0981 after correction. The Ratio of minimum to maximum transmission is 0.4621. The $\lambda/2$ correction factor is Not present.
T_{min}, T_{max}	0.607, 0.746	0.348, 0.753
No. of measured, independent and observed [$I > 2\sigma(I)$] reflections	18283, 4833, 4392	7896, 2156, 2139
R_{int}	0.018	0.052
$(\sin \vartheta/\lambda)_{max}$ (Å^{-1})	0.716	0.610
$R[F^2 > 2\sigma(F^2)]$, $wR(F^2)$, S	0.040, 0.067, 1.32	0.043, 0.124, 1.09
No. of reflections	4833	2156
No. of parameters	222	181
No. of restraints	0	1
H-atom treatment	H-atom parameters constrained	H-atom parameters constrained
$\Delta\rho_{max}$, $\Delta\rho_{min}$ (e Å^{-3})	0.66, −0.76	1.08, −1.14
Absolute structure	-	Flack x determined using 711 quotients [(I+)-(I-)]/[(I+)+(I-)] (Parsons, Flack and Wagner, Acta Cryst. B69 (2013) 249-259).
Absolute structure parameter	-	0.236(10)

4.2.6 Powder X-ray Diffraction (PXRD)

Materials obtained from LAG experiments were analysed by PXRD. PXRD was carried out using a flat-plate transmission geometry multi-well Bruker D8 Advance II powder diffractometer using Cu-Kα radiation (λ = 1.5406 Å) at 21 °C-24 °C. Data was collected between a 2ϑ of 4-35°, a step size of 0.017° and S_1/step.

4.2.7 Differential Scanning Calorimetry (DSC)

DSC was carried out using a Mettler Toledo DSC822e equipped with auto-sampler (TSO801RO). Approximately 2-4 mg of sample was loaded into a 40 μL aluminium crucible with a pierced aluminium lid before being crimped and loaded onto the calorimeter. The SebA, L and TMA samples were heated at a rate of 10 °C/min from 10 °C to 150 °C, 25 °C to 250 °C and 25 °C to 400 °C under a constant N_2 gas flow.

4.2.8 Thermogravimetric Analysis (TGA)

TGA was carried out using a Netszch STA 449 F1 Jupiter. Approximately 2-3 mg of sample was loaded into a 25 μL aluminium crucible with a pierced aluminium lid before being crimped and loaded onto the carousel. Samples were heated from 20 °C to 150 °C at a rate of 10 °C/min.

4.2.9 Ultraviolet/Visible Spectroscopy (UV/Vis)

UV/Vis was carried out using a Cary 50 spectrophotometer with scans being acquired between 325-800 nm. Stock solutions of approximately 0.1% w/v were prepared in methanol before being sufficiently diluted by a factor of 50 to yield an absorbance value of approximately 1.0.

4.2.10 Liquid Chromatography Mass Spectrometry (LC-MS)

LC-MS analysis was carried out using a Thermo Fisher Exactive Accela 600 LC system with the LC connected to the mass spectrometer through an electrospray ionisation (ESI) interface. An ACE 3 C18 reversed phase column (150 x 3 mm, 3 μm particle size) with a mobile phase consisting of MeCN: H_2O (5:95) in 0.1% Formic acid with an injection volume of 100 μL and a flow rate of 0.3 mL/min.

4.2.11 Nuclear Magnetic Resonance Spectroscopy (NMR)

NMR experiments were carried out on a two channel Bruker AVANCE III 500MHz spectrometer equipped with a 9.4 T Bruker UltraShield magnet and a PA BBO 500S2 smart probe operating under Top Spin 3.6.1. Samples were prepared by dissolving approximately 10 mg in 0.75 mL of methanol-d_4.

4.3 Results & Discussion

4.3.1 Ionisation of PPD

4.3.1.1 Recrystallisation of PPD

To enable us to investigate the creation of ionic co-crystals, we verified the formation of the PPD hydrochloride salt through recrystallization of PPD from a hydrochloric acid solution.[31] The HCl salt crystallises in the triclinic space group $P\bar{1}$ with one Cl atom and half a molecule of PPD in the asymmetric unit as PPD is located on a crystallographic inversion centre. The PPD molecules are doubly deprotonated forming a Cl···N (3.174(2) Å) hydrogen bond which is the dominant interaction, although π-π stacking interactions are also observed. The Cl···N hydrogen bond results in the formation of these hydrogen bonded tapes (*Figure 4.1*) which are composed of the interaction between two protonated ammonium groups and two chlorine atoms forming $R_4^2 8$ and $C_4^2 18$ graph set motifs.

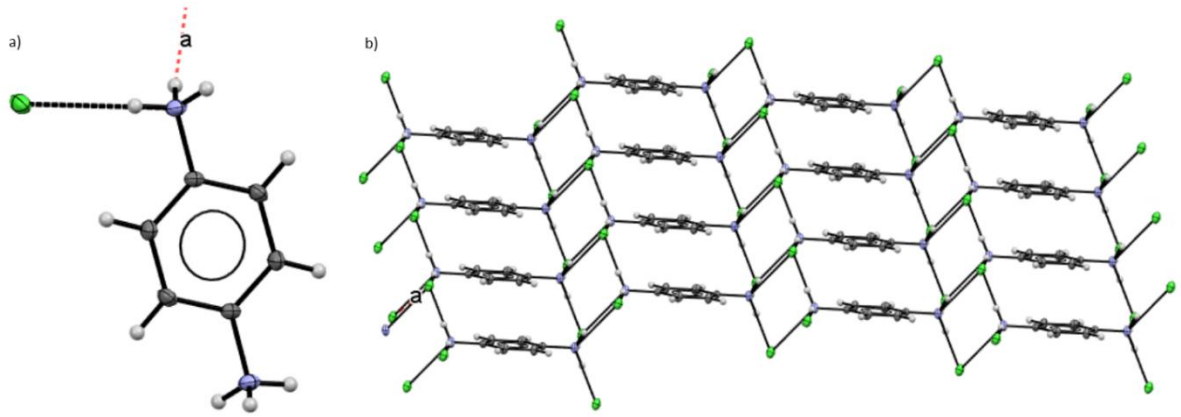

Figure 4.1: a) The crystal structure of the PPD HCl salt determined at 21.85 °C and b) the packing down the crystallographic *b*-axis of the HCl salt showing the interactions formed between the two components respectively with the thermal ellipsoids shown at the 50% probability level.

The creation of the solid allowed us to move forward with our investigation of ICCs, but we did note that the resulting solution from this crystallisation was a light purple colour, although the crystals obtained were colourless. It should be noted that this was solely an observation and no analysis was performed on this solution. From the previous PPD work, we have seen how the colour of a neutral PPD solution changes over several months when exposed to air, so this experiment would indicate that the colour has been altered through acidifying PPD. Another potential approach to altering the colour is via multi-component crystallisation of *p*-phenylenediamine dihydrochloride which may alter the colour as a result of ionic co-crystal formation.

4.3.1.2 *Ionic Co-crystals of PPD*

As the *p*-phenylenediamine dihydrochloride salt was obtained through recrystallisation, further experiments would investigate whether the formation of an ionic co-crystal of PPD with sebacic or trimesic acids would also alter the resultant colour. These two co-formers were previously used to create salts of PPD and with that a deeply coloured solution. By using the hydrochloride salt in this way, we would prevent the ionisation of the co-former, but the PPD would be ionised.

The LAG experiments were performed in various different ratios, grinding times and different solvents, however, the powder patterns (*Figure 4.2*) for both sebacic and trimesic acids resulted in physical mixtures of the two components. In the case of TMA, the ball-milled samples are predominantly α-TMA with a small amount of unreacted hydrochloride salt present. The experiments performed in the search of an ionic co-crystal of PPD exhausted all avenues and with these systems ionic co-crystal formation was not successful through either milling or solution crystallisation.

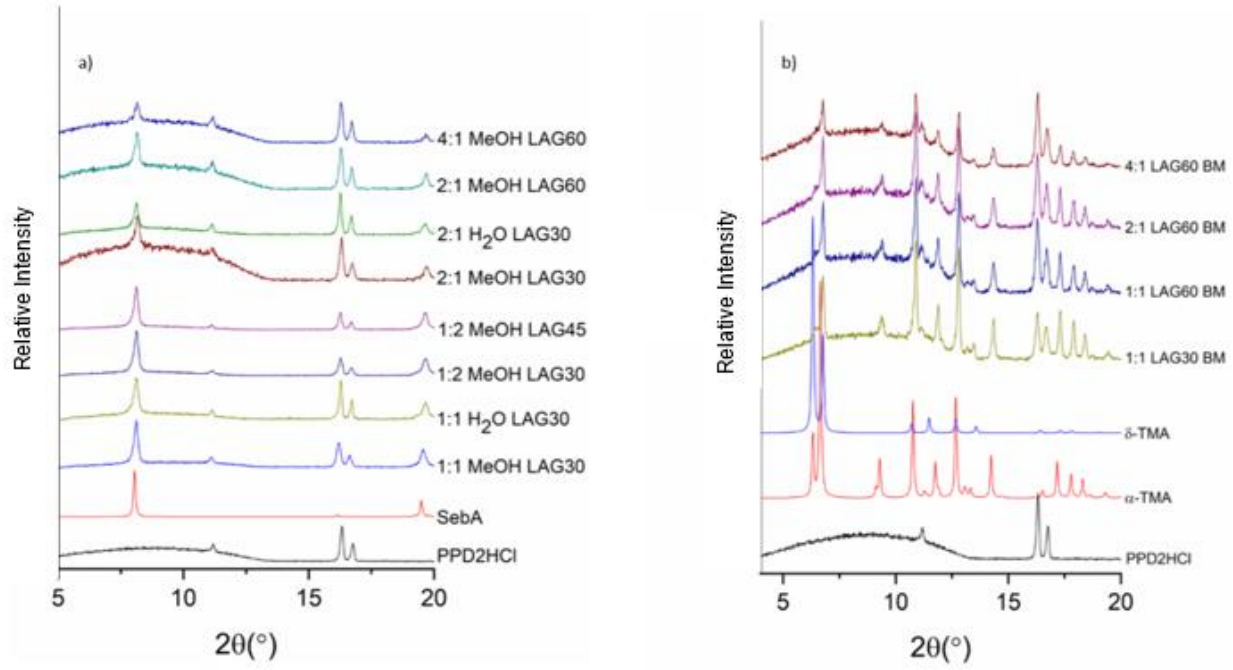

Figure 4.2: a) The PXRD patterns of PPD2HCl-SebA obtained from ball-milling experiments compared with the simulated patterns for PPD2HCl and SebA; b) the PXRD patterns of PPD2HCl-TMA obtained from ball-milling experiments in methanol compared with the simulated patterns for PPD2HCl, α-TMA and δ-TMA.

4.3.2 Co-crystallisation of OPD/MPD

4.3.2.1 o-Phenylenediamine: Sebacic Acid

Mechanochemical treatment of organic materials is known to initiate a change in polymorphs hence it is important to understand the polymorphic behaviour of the components under study. In this case, there has only been one reported crystal form of sebacic acid to date hence this simplifies the interpretation of the data to some extent.[32] We have previously ball-milled the pure components by themselves in the work on alizarin co-crystals in the next chapter and observed no change in polymorph over the treatment. The powder from ball-milling experiments (*Figure 4.3*) reveals the presence of a new crystalline form which does not match either OPD Form I or SebA, although the peak observed at approx. 8° 2ϑ is also present in the pattern of SebA. The DSC trace of the ball-milled powder (*Figure 4.3*) features a single endothermic event with an onset temperature of 93.9 °C corresponding to the melt of this material indicating that the phase is pure and that a new crystal form has been obtained. The TGA trace (*Figure 4.3*) shows no significant weight loss before the onset of degradation confirming that this crystalline material is a new anhydrous crystalline form.

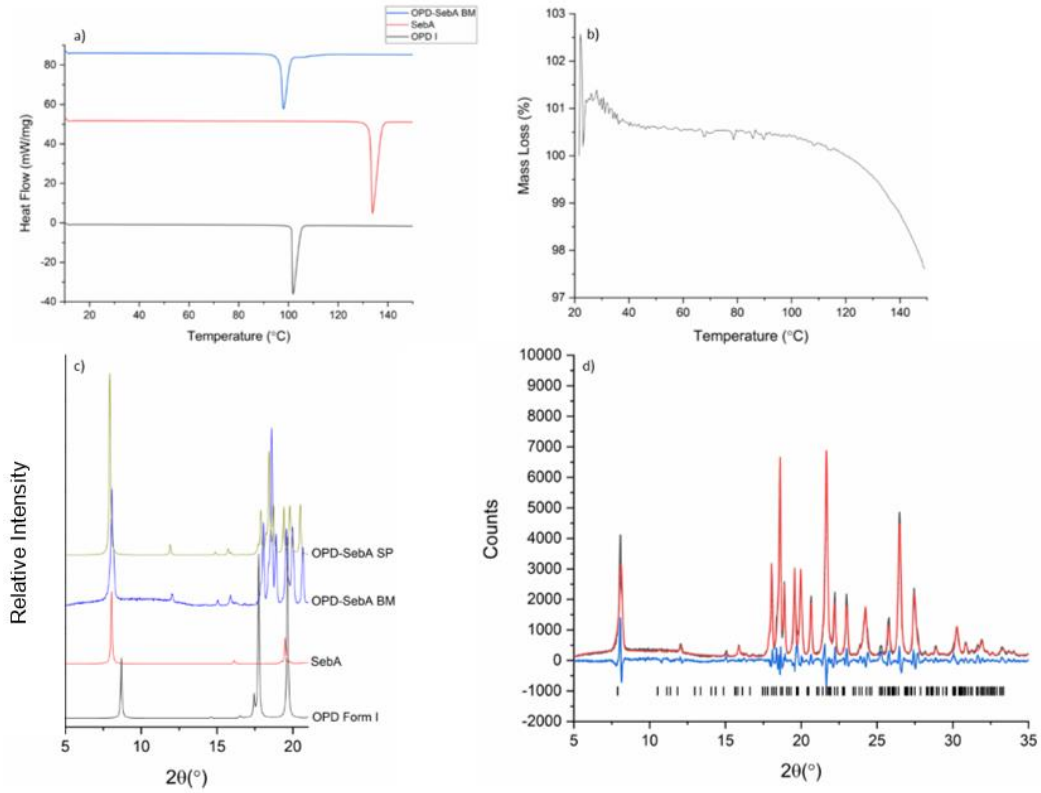

Figure 4.3: a) The DSC trace of the ball-milled powder compared with the traces for OPD Form I and SebA; b) the TGA trace of OPD-SebA BM; c) the PXRD pattern of OPD-SebA from methanol compared with the simulated patterns for OPD Form I, SebA and OPD-SebA from the single crystal experiment; d) the Pawley fit of the ball-milled pattern with the unit cell parameters from the single crystal data.

Evaporative crystallisation of OPD and SebA from an IPA solution resulted in the formation of a 2:1 salt co-crystallising in $P\bar{1}$ with the asymmetric unit containing two molecules of *o*-phenylenediamine and one molecule of sebacic acid. Salt formation results in a doubly deprotonated sebacic acid molecule as a result of proton transfer to one of the amine moieties on each phenylenediamine molecule. The intermolecular interaction observed between OPD and SebA results in the formation of strong hydrogen bonds (2.71-2.77 Å) between the amine/ammonium groups and the carboxylate of the sebacic acid. The sebacic acid interacts with each of the OPD molecules using an $R_2^2 9$ hydrogen-bonded ring where all the protons are located on the OPD. The 2:1 OPD-SebA units are connected together through hydrogen bonding from the two other protons attached to the ammonium group; the second hydrogen on the amine is redundant and is involved in an N−H…π interaction of the neighbouring ring. The 2:1 units hydrogen bond into tapes (Figure 4.4a) through a $C_2^2 6$ graph set which forms $R_4^4 30$ graph set motifs with the tapes interacting through the third proton of the ammonium group to form layers (Figure 4.4b). Large thermal ellipsoids on the aromatic rings particularly the outer carbons which show greater libration attributed to a looser interaction between the layers (Figure 4.4c).

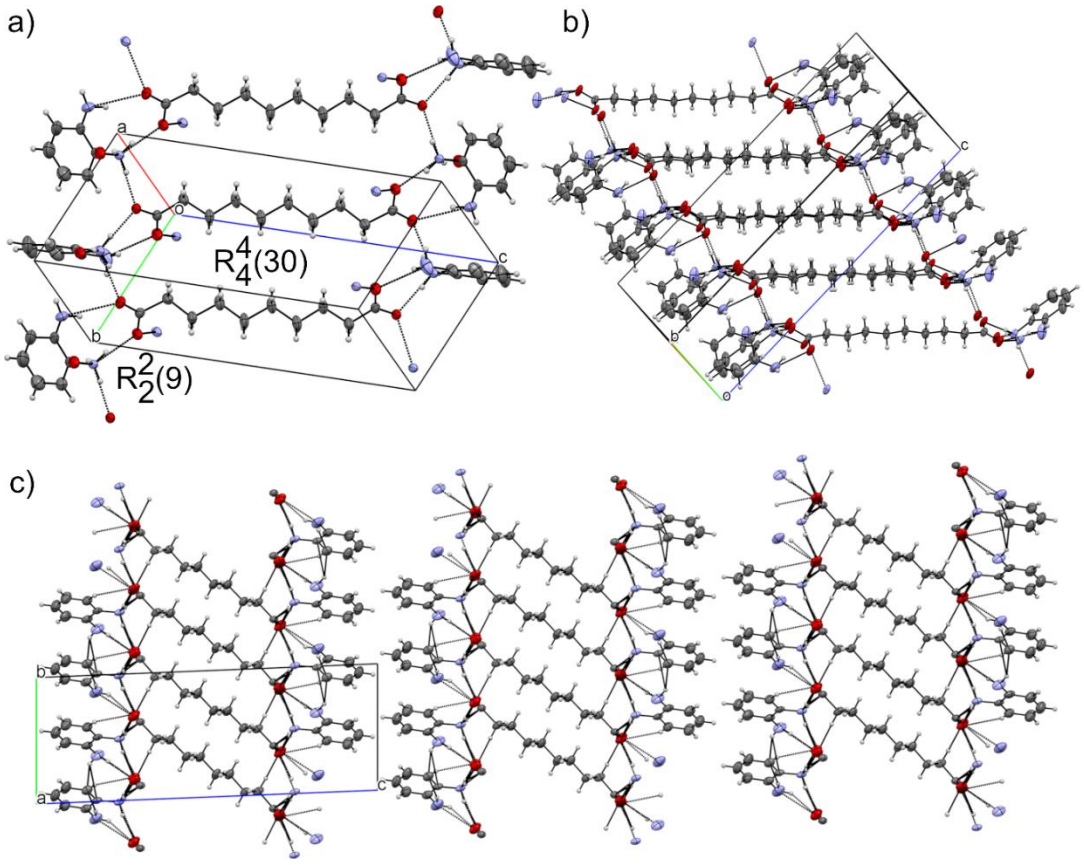

Figure 4.4: a) and b) The hydrogen bonding network of the OPD-SebA (2:1) salt showing the hydrogen-bonded tapes; c) the extended structure of OPD-SebA showing the thermal ellipsoids at the 50% probability level.

4.3.2.2 o-Phenylenediamine: Trimesic Acid

4.3.2.2.1 Polymorphism of Trimesic Acid

Trimesic acid (TMA) has a far richer behaviour than sebacic acid hence a more in depth discussion of its phase behaviour is required. It has four known polymorphic forms with the structure of *α*-TMA being determined by Duchamp in 1969 and since then three additional forms have been identified.[33] TMA has also been shown to readily form hydrates/solvates with most common organic solvents including pyridine, methanol, acetic acid, DMSO, *n*-pentanol, *n*-butanol, *etc.*[34–37] Ward *et al.* have recently identified two new solvates of TMA from dimethylfomamide and ethanol as well as the previously identified IPA solvate which they have shown to undergo a temperature-induced phase transition.[38] *α*-TMA has been reported to undergo a phase transformation at high temperature to a polycrystalline *β*-phase at approx. 270 °C which subsequently melts at 330 °C.[39] Cui *et al.* have recently reported the formation of *δ*-TMA by creating solvates with various solvents (*e.g.* water, cyclohexane) that have the hexagonal TMA structure that had been predicted through crystal structure prediction (CSP) and which was observed experimentally via a high throughput (HT) crystallisation screen using more than 250 crystallisation conditions. They were able to exchange the solvent in the pores with pentane before and evacuating the pores under vacuum to leave the *δ*-form via a single crystal to single crystal phase transformation from the pentane solvated form to anhydrous *δ*-TMA.[40] The hexagonal structure of TMA molecules matched those structures predicted. The δ-phase has been shown by PXRD to be thermally stable up to 110 °C, but which converts to *α*-TMA at 130 °C after six hours under vacuum at RT, indicating that the *δ*-phase is a metastable form. During our milling experiments, the *α*-form is the form most likely to be observed, however, for solution crystallisation experiments there is a good chance that hydrated/and or solvated forms of TMA may be observed in addition to multi-component that we are wanting.

4.3.2.2.2 Characterisation of *o*-Phenylenediamine: Trimesate Salt

The PXRD pattern from ball-milling experiments (*Figure 4.5*) confirms the presence of a new crystalline phase with peaks occurring at 2*ϑ* values of approx. 6°, 14.5°, 16° and 18.5° that are not present in OPD Form I, *α*-TMA or *δ*-TMA. There is a peak at approx. 12° 2*ϑ* which is also present in *α*-TMA. The DSC trace (*Figure 4.5*) of supplied *α*-TMA features two endothermic events, firstly a broad endotherm with an onset temperature of 301.5 °C indicative of a phase transformation between the *α* and *β*-forms followed by the main endothermic event which has an onset temperature of 353.3 °C corresponding to the melting of this phase. The DSC trace of the ball-milled powder shows multiple endothermic events, firstly a broad endotherm with an onset temperature of 186.7 °C which could indicate a transition between two solid forms. The second thermal event

features a small broad endotherm which is also present in α-TMA with an onset temperature of 304.1 °C and corresponds to a phase transition in the unreacted TMA. It should be noted that the samples used in the DSC and PXRD are different with the DSC being more sensitive to small amounts of material compared to PXRD.

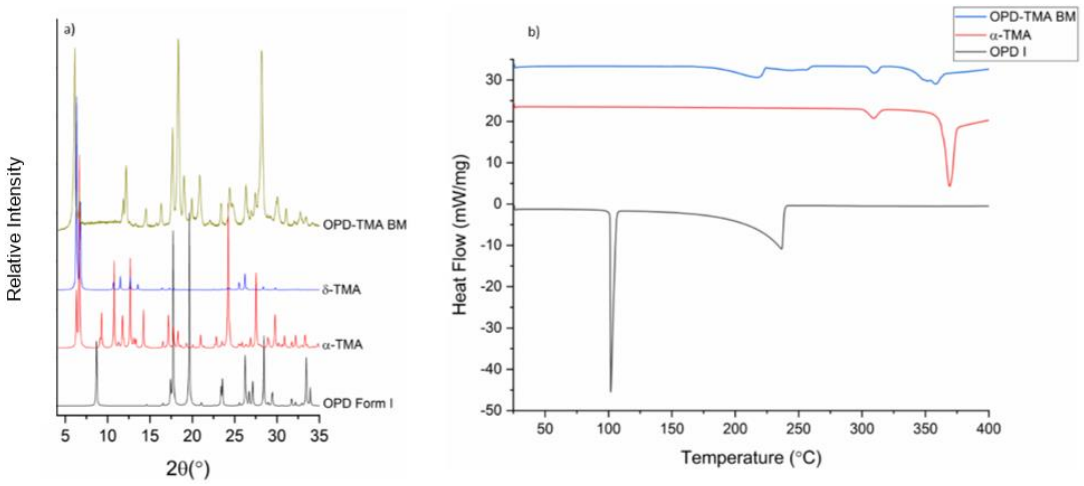

Figure 4.5: a) The PXRD pattern of OPD-TMA BM from methanol compared with the simulated patterns for OPD Form I, α-TMA and δ-TMA; b) the DSC trace of OPD-TMA BM compared with the traces of OPD Form I and α-TMA.

A new 1:1 salt form of OPD-TMA was obtained through cooling crystallisation of the ball-milled powder in methanol. The molecules co-crystallise in the space group *C*2/*c* with one molecule of *o*-phenylenediamine and one molecule of trimesic acid in the asymmetric unit. An ammonium to carboxylic acid (2.794(5) Å) hydrogen bond is observed between the two molecules that forms a $D_2^1 8$ graph set (vertical direction in *Figure 4.6*a). A second hydrogen bond from the amine to the carboxylate group of the TMA completes a two-point contact between the TMA network and the OPD. The TMA molecules interact via the $R_2^2 8$ dimer with the electron density map (and C−O bond lengths) showing the rotational disorder of the carboxylic acid group. The TMA also interacts with other TMA molecules through an acid to carboxylate interaction that provides a network of TMA molecules that host the OPD in the hydrogen bonded rings. The previous interactions between the OPD and TMA are formal hydrogen bonds that involves the hydrogen of the ammonium group, however the orientation of the OPD molecules enables close contact of the amine and ammonium groups with the carboxylic acid and carboxylate groups of neighbouring TMA molecules. The OPD molecules possess larger thermal ellipsoids on the phenylenediamine ring which is a consequence of libration indicating that the OPD molecules have some freedom of movement. The hydrogen-bonded layers are flat (*Figure 4.6*c) and they stack together using the third hydrogen of the ammonium group. The layers are offset with respect to each other (**Error! Reference source not found.**b) but do provide a channel where the OPD sits in the TMA framework. This three-

dimensional hydrogen bonded network in contrast with the sebacic acid salt where there were loser interactions between the layers.

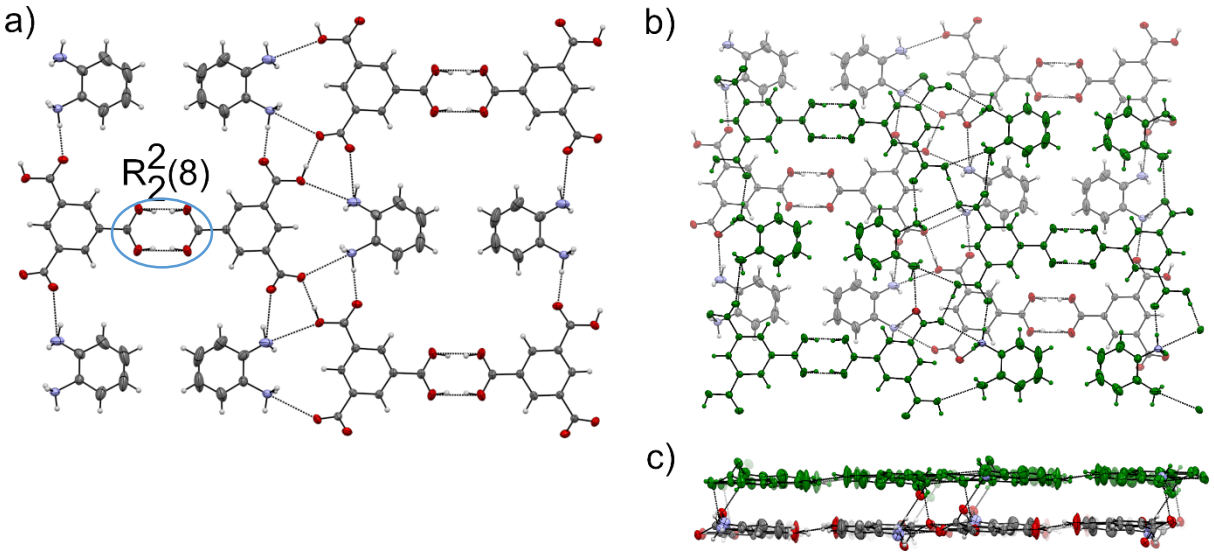

Figure 4.6: a) The hydrogen-bonded network observed between the OPD and TMA molecules viewed down the crystallographic *c*-axis also showing the short contact interactions formed; b) another view of the hydrogen-bonded network of OPD-TMA showing the layers offset in green; c) The packing of OPD-TMA molecules showing the π-π stacking between the rings with the thermal ellipsoids shown at the 50% probability level.

4.3.2.3 o-Phenylenediamine: Lawsone

4.3.2.3.1 Polymorphism of Lawsone

2-hydroxy-1,4-napthoquinone (lawsone) has three known polymorphic forms denoted as the triclinic, monoclinic and orthorhombic forms with the monoclinic/orthorhombic polymorphs reported to be a case of solvent induced polymorphism whereby different crystallisation solvents yield different polymorphic forms due to differences in the solvents intermolecular interactions. Crystallisation from acetonitrile yields the triclinic polymorph, whereas crystallisation from methanol and acetone results in the monoclinic and orthorhombic forms respectively.[41-42] As all of our co-crystallisation experiments involving lawsone were carried out from methanol, the monoclinic polymorph was the form most likely to be observed.

4.3.2.3.2 Characterisation of New Form

Our initial solution crystallisation experiments carried out from methanol resulted in the material precipitating out as fine red needles after approximately 60 minutes. From the characterisation of the red needles, we observed that a condensation reaction between OPD and lawsone had occurred through the reaction of the amine of OPD and the carbonyl and hydroxyl group of lawsone (*Figure 4.7*). The needles crystallised in the monoclinic space group $P2_1/c$ with one molecule in the asymmetric unit lying in general positions. There are strong O–H···N (2.762 Å) hydrogen bonds linking these two molecules together forming discrete chains through $C_1^1 6$ hydrogen bond motifs packing in a head-to-toe arrangement. The molecules are arranged so that they lie at 87.31° with respect to each other along the hydrogen-bonded chain. The hydrogen-bonded chains are stacked in the *a*- and *c*-direction and have only van der Waals interactions between them. The chains in along the *a*-direction have the aromatic nitrogen and aromatic ring in close proximity (C–X and C–Y···N–Z) whilst the chains in the *c*-direction show perpendicular C–H···π interactions.

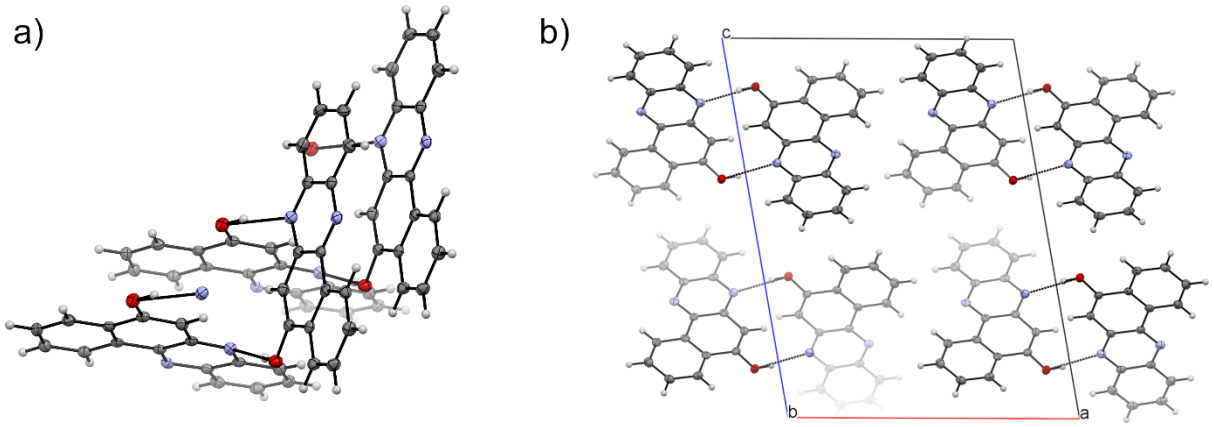

Figure 4.7: a); b) The arrangement of the molecules in the unit cell showing the O–H···N hydrogen bonds with the thermal ellipsoids shown at the 50% probability level.

To investigate the reactivity of these two materials, we performed ball-milling experiments on this system using LAG. The powder from LAG experiments (*Figure 4.8*) yields the same diffraction pattern as the simulated pattern obtained from solution crystallisation which confirmed that both ball-milling and solution crystallisation yielded the same phase and that the chemical reaction proceeded under both of these conditions. The DSC trace of the ball-milled powder (*Figure 4.8*) after 30 minutes of milling shows a very clean DSC with a single endothermic event which has an onset temperature of 327.6 °C corresponding to the melt of this material. In terms of milling time, other reactions in the literature carried out through mechanochemical methods have reported milling times ranging from 8 minutes up to 2 hours depending on the frequency and type of mill, *i.e.* ball-mill, planetary mill, *etc.*[43]

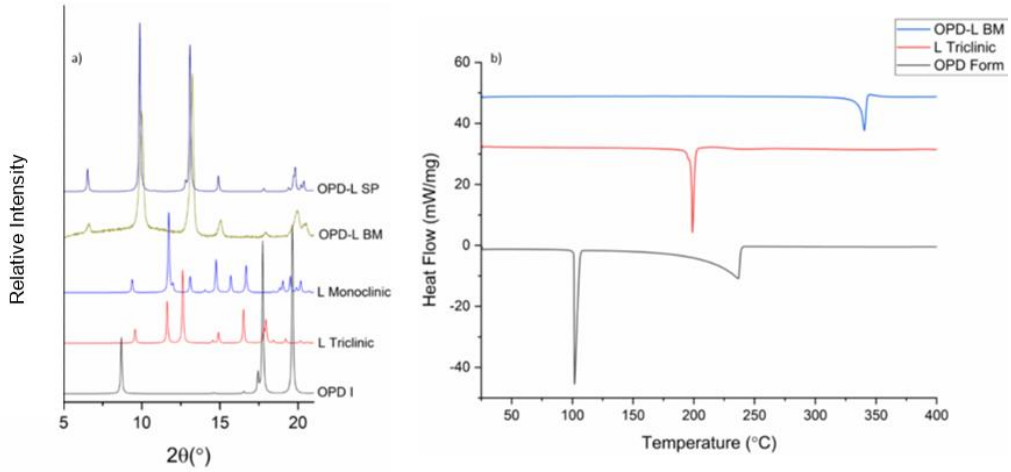

Figure 4.8: a) The PXRD pattern of OPD-L BM from methanol compared with the simulated patterns for OPD Form I, Lawsone triclinic and L monoclinic; b) the DSC trace of OPD-L BM compared with the traces of OPD Form I and L triclinic.

4.3.2.4 Reactivity of OPD

From our results during the OPD-L experiment, the solution reactivity of OPD was monitored over a period of several months using both LC-MS and NMR spectroscopy to probe the stability of OPD and identify the resulting oxidation products. The reason for this was due to OPD being shown to undergo oxidation using hydrogen peroxide or molecular oxygen in the presence of metal ions resulting in the formation of the main oxidation product 2,3-diaminophenazine (DAP).[44] Unfortunately, the solution reactivity of OPD-L was never investigated.

The LC-MS chromatogram of the fresh sample of OPD (MeCN:H_2O (1:1 v/v), 0.1 mg/mL) (Figure 4.9) has a retention time of 2.81 minutes with the corresponding spectrum from the MS analysis indicating that the ion at a *m/z* of 109 mass units corresponds to pure OPD. The LC-MS chromatograms shown below in Figure 4.9 b) and c) represents two OPD samples analysed after

approximately six-weeks which were prepared one day apart. Firstly, the LC-MS chromatograms of the peak eluting at 2.97 minutes shows that this peak corresponds to the ion in the MS spectrum at approx. 211 mass units which is thought to be the formation of a dimer as previously observed during the PPD work. However, a review of the literature indicates the main oxidation product to be 2,3-diaminophenazine (DAP) which would correlate with the peak at 211 mass units.[44] Secondly, the LC-MS chromatogram of the peak eluting at 2.94 minutes indicates that this peak corresponds to the ion at approx. 125 mass units with no presence of OPD which is an additional 16 mass units compared to pure OPD suggesting the possible formation of an N-oxide (Table 4.7). In contrast, there is still the presence of trace amounts of OPD shown by the ion at 109 mass units in b) which is very surprising as the samples were prepared in exactly the same way using the same solvent and the solid was from the same batch.

Table 4.7: The suspected chemical structure of the N-oxide and 2,3-diaminophenazine (DAP)[44] respectively.

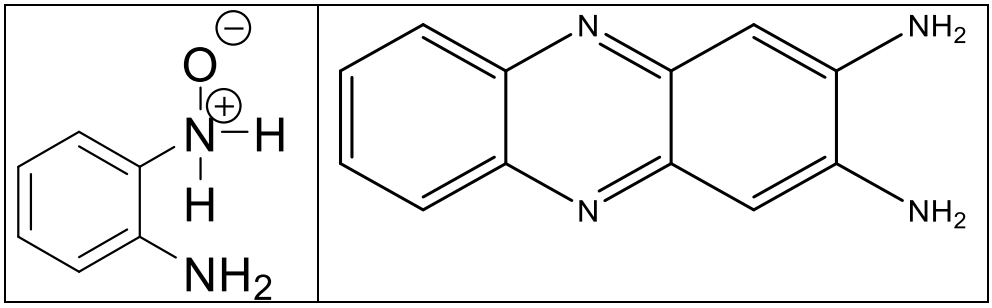

Over the course of the experiment (six weeks), there was a substantial change in the colour of the solution. The fresh sample was colourless, but after six-weeks the two samples changed to have a yellow tinge. This colour change has been observed to occur after 24 hours during evaporative crystallisations from ethanol and 1-butanol, but not from ethyl acetate. This colour change was also observed in the solutions of the salt forms of OPD and is most likely to be due to oxidation. Further work would look to investigate these two products in more depth and whether oxidation is indeed the reason for the colour change.

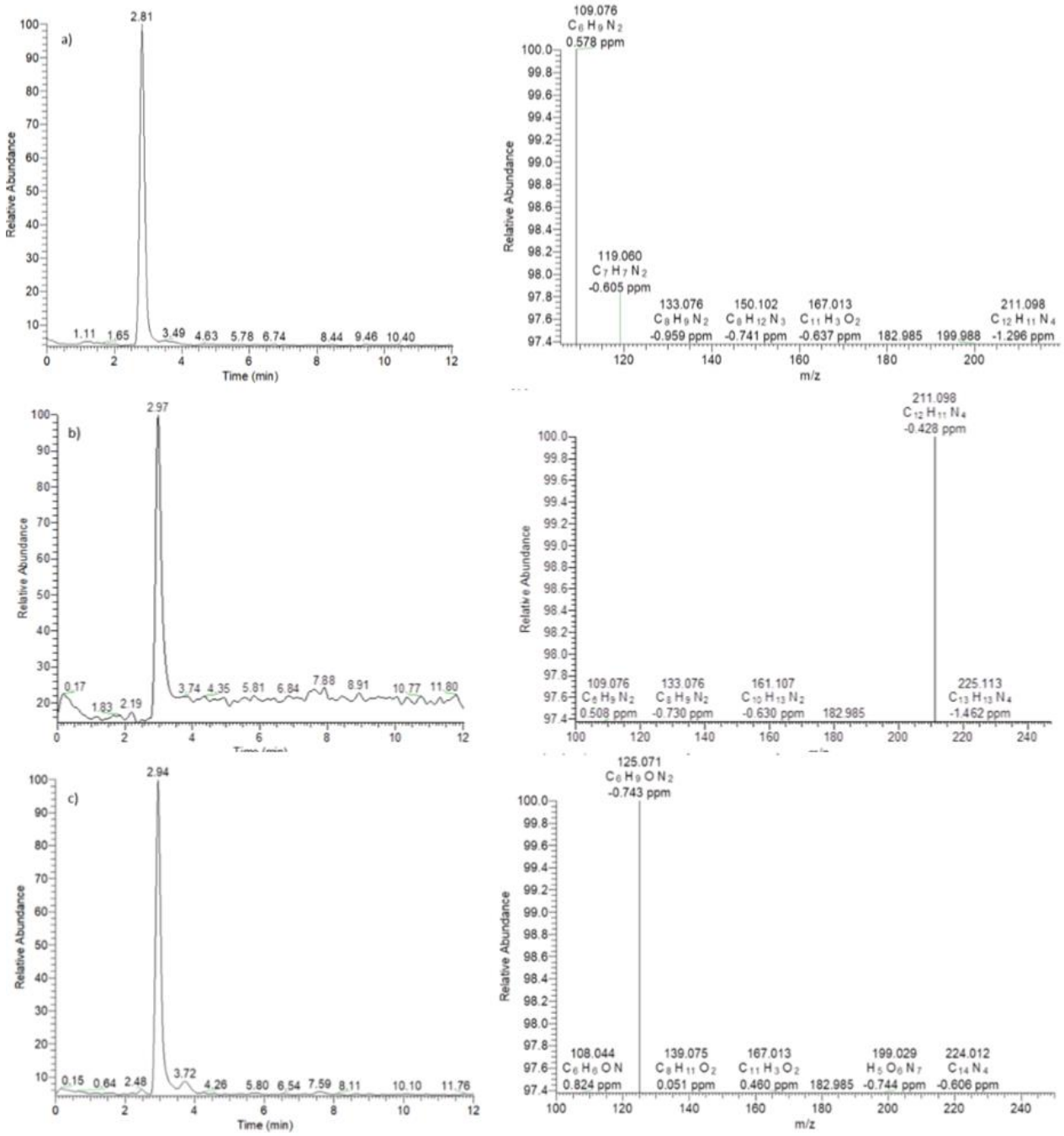

Figure 4.9: a) The LC-MS chromatogram of a fresh sample of OPD with the corresponding mass spec for the peak eluting at 2.81 minutes; b) and c) The LC-MS chromatograms for two samples one day apart both six weeks-old with the corresponding mass spec's for the peaks eluting at 2.97 minutes and 2.94 minutes respectively.

To support the LC-MS work, we performed NMR spectroscopy of the samples prepared via the same method. The fresh ^{1}H NMR spectrum of OPD (Figure 4.10) shows four signals, two of which are attributed to the solvent in this case methanol-d_4 occurring at 3.33 ppm and 4.86 ppm. There is no observed signal for the amine protons which would be expected to occur between 0.5-5.0 ppm which is not commonly observed as a result of proton exchange. The chemical shifts in the aromatic region of the spectrum (approx. 6.5-8.0 ppm) shows two signals split into a doublet of doublets at approx. 6.66 ppm and 6.67 ppm.

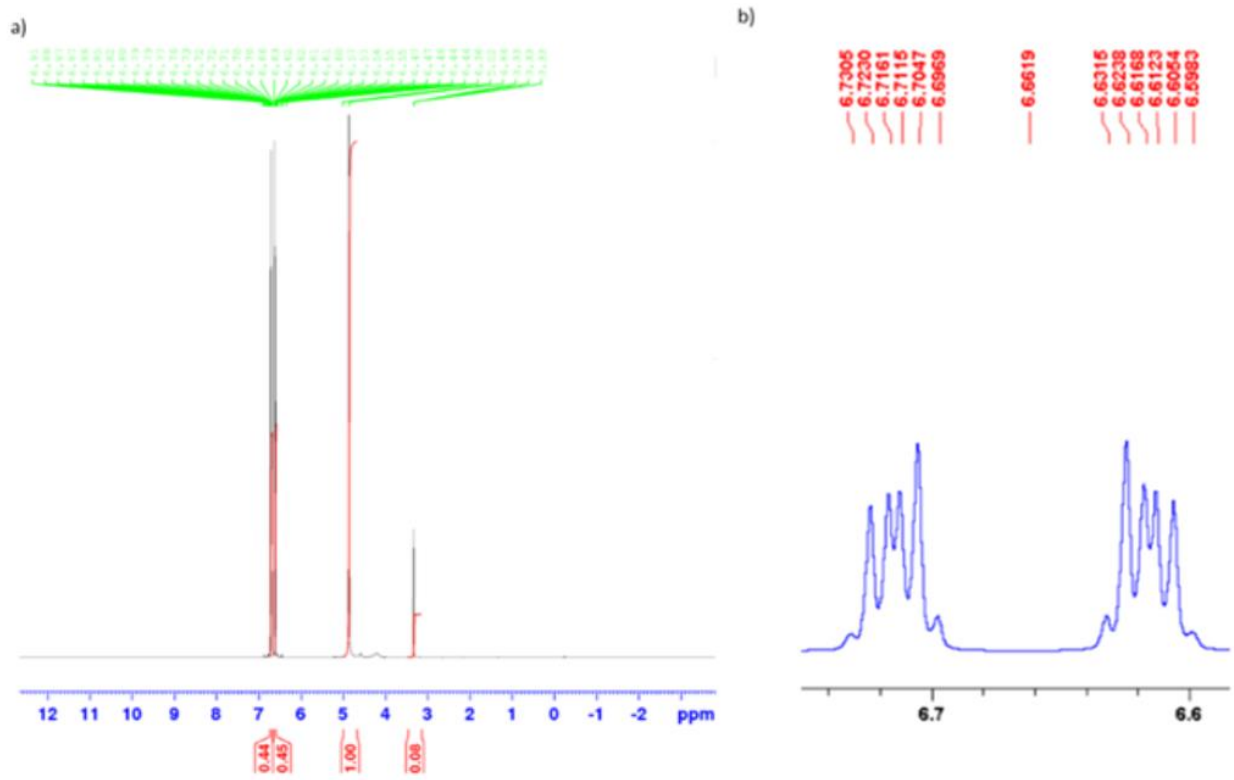

Figure 4.10: a) The ^{1}H NMR spectrum of OPD in methanol-d_4; b) an enlarged view of the aromatic region of the spectrum.

Using the knowledge obtained from the LC-MS analysis, simulated ^{1}H NMR spectrums of the two suspected oxidants should help us identify the peaks attributing to these degradants and which peaks can be possible impurities. Our NMR experiments performed over a four-month time period starting with the bottom blue trace (fresh sample) and the top red trace (after four-months) clearly show significant differences, partiularly in the aromatic region. It should be noted that we have zoomed into the baseline (Figure 4.11) to aid our understanding of the oxidation reaction pathway. In the aromatic region of the spectrum, there are peaks at approx. 7.80 ppm and 7.60 ppm which correspond to 2,6-diaminophenazine (DAP) and a peak at approx. 7.10 ppm which does not appear to correlate with the simulated spectrums of either oxidant. However, the two protons attached to nitrogen of the N-oxide has a predicted chemical shift of *ca.* 7.2 ppm, so it could possibly be

attributed to this. The signal observed at *ca.* 6 ppm is only evident after approx. 12 weeks and from the intensity, it appears to be noise rather than a true peak. The same can also be said for the three signals observed between 1-2 ppm as there are no predicted signals in this region for either of the two degradants/oxidants or even the starting material for that matter. The NMR analysis performed largely confirms that the experimental data backs up the LC-MS data, although the NMR data is rather complex to interpret given the reactivity of OPD.

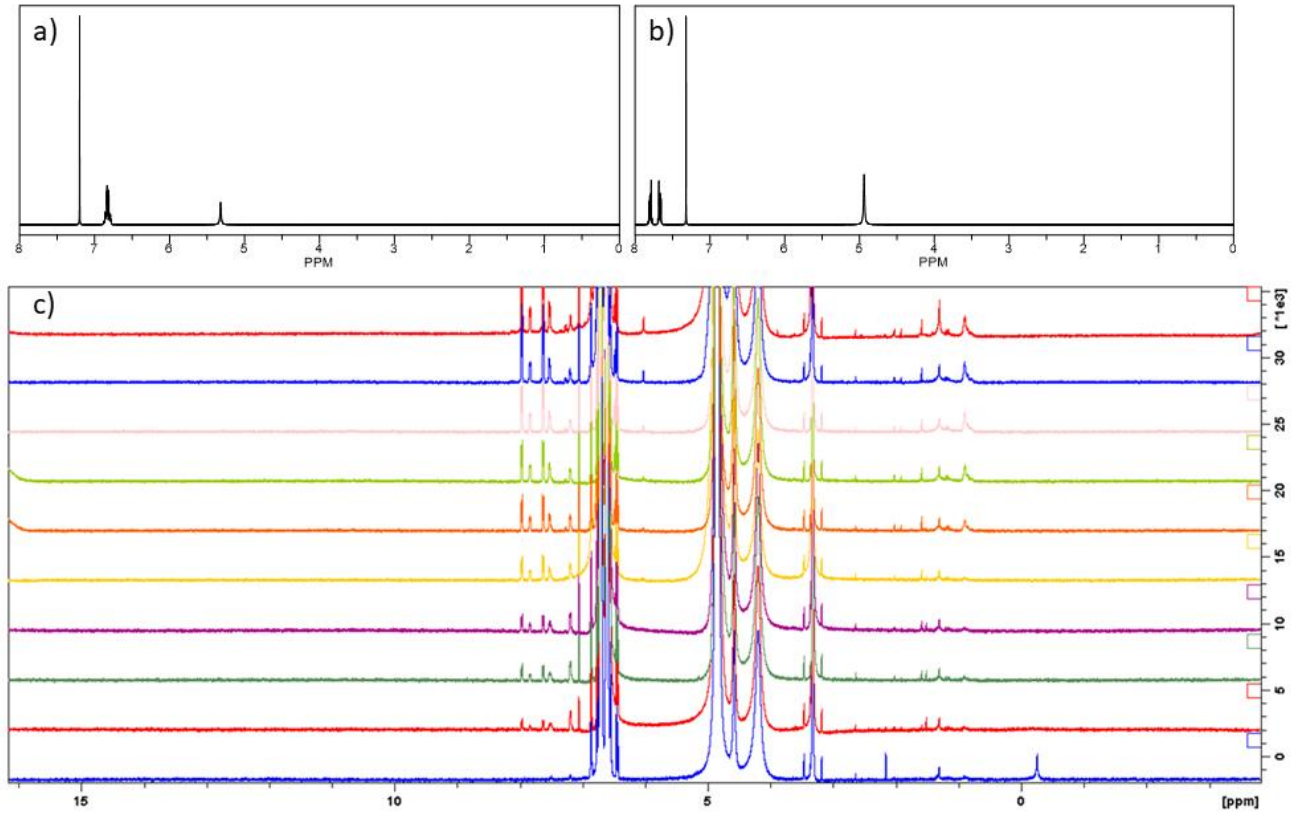

Figure 4.11: a) and b) The simulated ^{1}H NMR spectrums in DMSO for the N-oxide and 2,3-diaminophenazine (DAP) respectively; c) the ^{1}H NMR spectrum monitored over a four-month period with the fresh sample (bottom spectrum in blue) and the subsequent six spectrums being acquired on a weekly basis with the pink spectrum (after 8 weeks), blue top (after 12 weeks) and red top (after 16 weeks).

4.3.3 Co-crystallisation of MPD

4.3.3.1 m-Phenylenediamine: Sebacic Acid

Our next investigation was of meta-phenylenediamine. LAG experiments between MPD and SebA were performed in methanol, ethanol, acetonitrile and ethyl acetate for 30 minutes however, solid was only recovered from acetonitrile and ethyl acetate as the solid was consumed during the process in the cases of methanol and ethanol. The PXRD patterns from ball-milling experiments (Figure 4.12) clearly indicates that the patterns are mixtures of MPD and SebA, although predominantly that of SebA. The DSC trace of the ball-milled powder (Figure 4.12) shows a single endothermic event with an onset temperature of 52.9 °C which corresponds to the melting of the material. The melting point of the ball-milled phase does not match either of the starting materials, even though the PXRD patterns were both shown to be physical mixtures of MPD and SebA which could possibly be a depression of the melting point due to the presence of the second component.

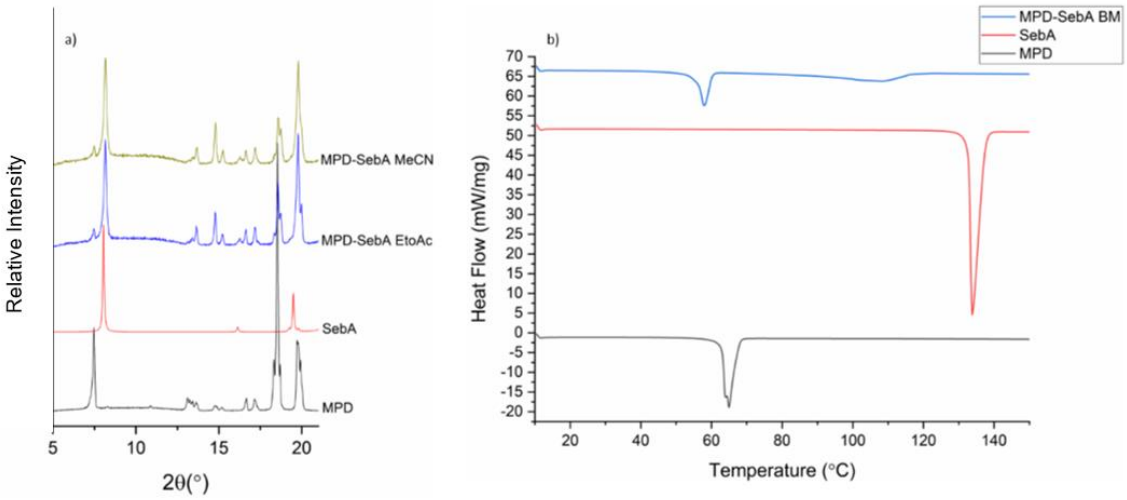

Figure 4.12: a) The PXRD patterns of MPD-SebA (1:1) BM compared with the simulated patterns for MPD and SebA; b) the DSC trace of the ball-milled powder from ethyl acetate/acetonitrile compared with the traces of MPD and SebA.

Solution crystallisation experiments utilised evaporative crystallisation in an attempt to co-crystallise MPD and SebA which had been unsuccessful via grinding. Evaporative crystallisation from alcohols resulted in suitable crystals from methanol which indexed as a = 4.95 Å, b = 10.11 Å, c = 11.21 Å crystallising in the triclinic space group $P\bar{1}$ which matches the cell parameters of SebA. In this case, both evaporative crystallisation and ball-milling failed to result in co-crystallisation (*Table 4.8*). It should be noted that these experiments were performed at the very end of the project and as due to time restraints, we were unable to perform as many experiments as we would have liked.

Table 4.8: Results from co-crystallisation experiments performed via solution crystallisation and grinding on MPD-SebA.

	Slow Evaporation	Ball Milling
Methanol	Sebacic acid	No product obtained – material dissolved
Ethanol	No crystals obtained	No product obtained – material dissolved
Acetonitrile	Not performed	Mixture of MPD + SebA
Ethyl Acetate	Not performed	Mixture of MPD + SebA

4.3.3.2 m-Phenylenediamine: Trimesic Acid

The powder pattern from LAG experiments (*Figure 4.13*) indicates the formation of a new crystalline phase that can be formed though ball-milling or solution crystallisation as confirmed by the Pawley refinement (*Figure 4.13*). The DSC trace of the LAG product (*Figure 4.13*) shows a new melt compared to the starting materials with an onset temperature of 213.2 °C, followed by a small broad endotherm which could possibly be the material becoming amorphous. To further understand what is happening beyond the melt, hot stage microscopy and/or heating the material up to the melt and then running PXRD to confirm if the material is in fact amorphous.

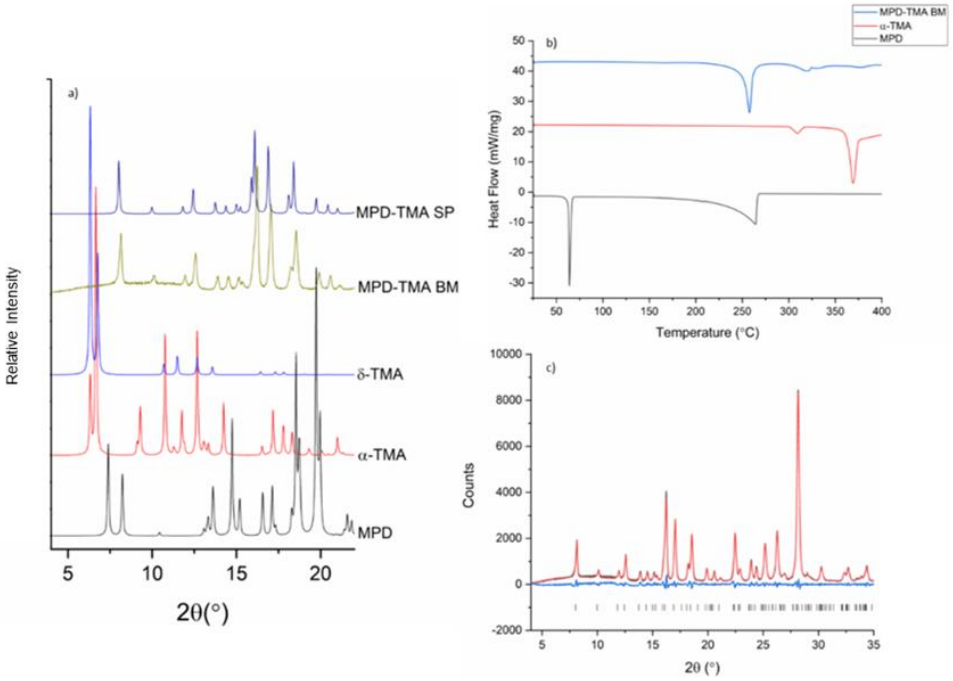

Figure 4.13: a) The PXRD pattern of MPD-TMA BM from methanol compared with the simulated patterns for MPD, *α*-TMA, *δ*-TMA and MPD-TMA; b) the DSC trace of the ball-milled product; c) the Pawley fit of MPD-TMA BM with the unit cell parameters from the single crystal experiment.

Crystallisation of the ball-milled product resulted in the formation of a 1:1 salt co-crystallising in the triclinic space group $P\bar{1}$ with one molecule of *m*-phenylenediamine and one molecule of trimesic acid in the asymmetric unit lying in general positions. The two molecules form a strong hydrogen bond through an acid···amine interaction (2.684(5) Å) resulting in $D_1^1 2$ graph set motifs with TMA molecules being connected through $R_2^2 8$ motifs. The layer is reminiscent of the OPD-TMA salt where the TMA dimer is retained and the dimers are linked between a singular acid···acid hydrogen bond. The MPD molecules are observed in a wider network of TMA that are in channels when viewed along the *c*-direction. The layers are not as planar as the OPD-TMA structure, but the layers are connected together through the third hydrogen of the ammonium group. There is also π-π stacking interactions observed between the phenylenediamine rings with the distance between the centroids of the rings being 5.157 Å and the distance between the planes of MPD being 2.876 Å.

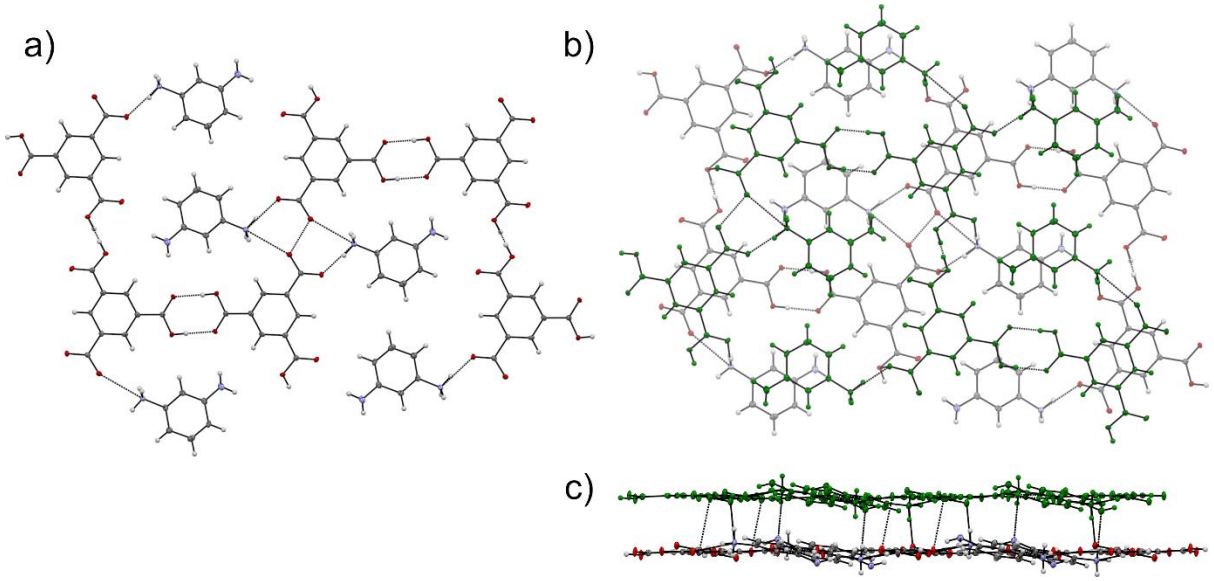

Figure 4.14: a) and b) The hydrogen bonding network of the MPD-TMA (1:1) salt with the molecules highlighted in green showing the molecules overlayed; c) the packing of the MPD-TMA salt showing the π-π stacking interactions between the rings with the thermal ellipsoids shown at the 50% probability level.

4.3.3.3 *m*-Phenylenediamine: Lawsone

The power diffraction pattern from ball-milling experiments (Figure 4.15) indicates the presence of a new crystal form which was also obtained from cooling crystallisation of the ball-milled powder as confirmed by the Pawley refinement (Figure 4.15). The DSC trace of the ball-milled powder (Figure 4.15) shows a sharp endotherm with an onset temperature of 110.5 °C corresponding to the melting of this material, immediately followed by a sharp exotherm due to recrystallization. The sharp melt with no other features in the DSC suggests that the material is in its pure form and that mechanochemical methods are able to produce the material with a high degree of purity.

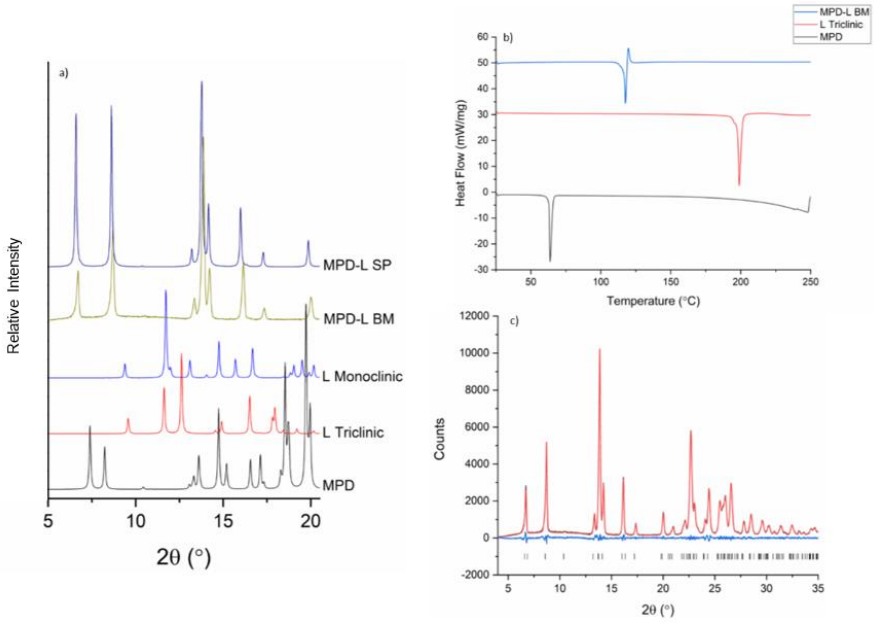

Figure 4.15: a) The PXRD pattern of MPD-L BM from methanol compared with the simulated patterns of MPD, L triclinic, L monoclinic and MPD-L; b) the DSC trace of the ball-milled product compared with the traces of MPD and L triclinic; c) the Pawley fit of MPD-L BM with the unit cell parameters from the single crystal experiment.

The crystal structure of MPD-L (Figure 4.16) was obtained through cooling crystallisation of the ball-milled powder, however, it should be noted that this data collection at 21.85 °C was stopped before the end of the first run because it was believed that this crystal was just a starting material. After a more in depth analysis of the data, the crystal indexed with the unit cell parameters: a = 13.626(7) Å, b = 4.103(2) Å, c = 26.103(15) Å, β = 100.53(3) °. The molecules co-crystallise in the space group $P2_1/c$ with one molecule of *m*-phenylenediamine and one molecule of lawsone in the asymmetric unit. Single crystal analysis revealed the formation of a 1:1 salt as a result of proton transfer from the phenol group to the protonated ammonium forming a strong O–H···N (2.660(14) Å) hydrogen bonding interaction resulting in $D_1^1 2$ graph set motifs. Two lawsone and two OPD molecules hydrogen-bond in a ring structure (Figure 4.16). These rings are stacked with an offset through the

third hydrogen of the ammonium group as depicted by the extended contacts to the top-left and bottom-right of Figure 4.16b. These stacks are connected via the second amine to form the extended structure (Figure 4.16c). The lack of data for this structure means that the resolution of the hydrogen positions prevents their location.

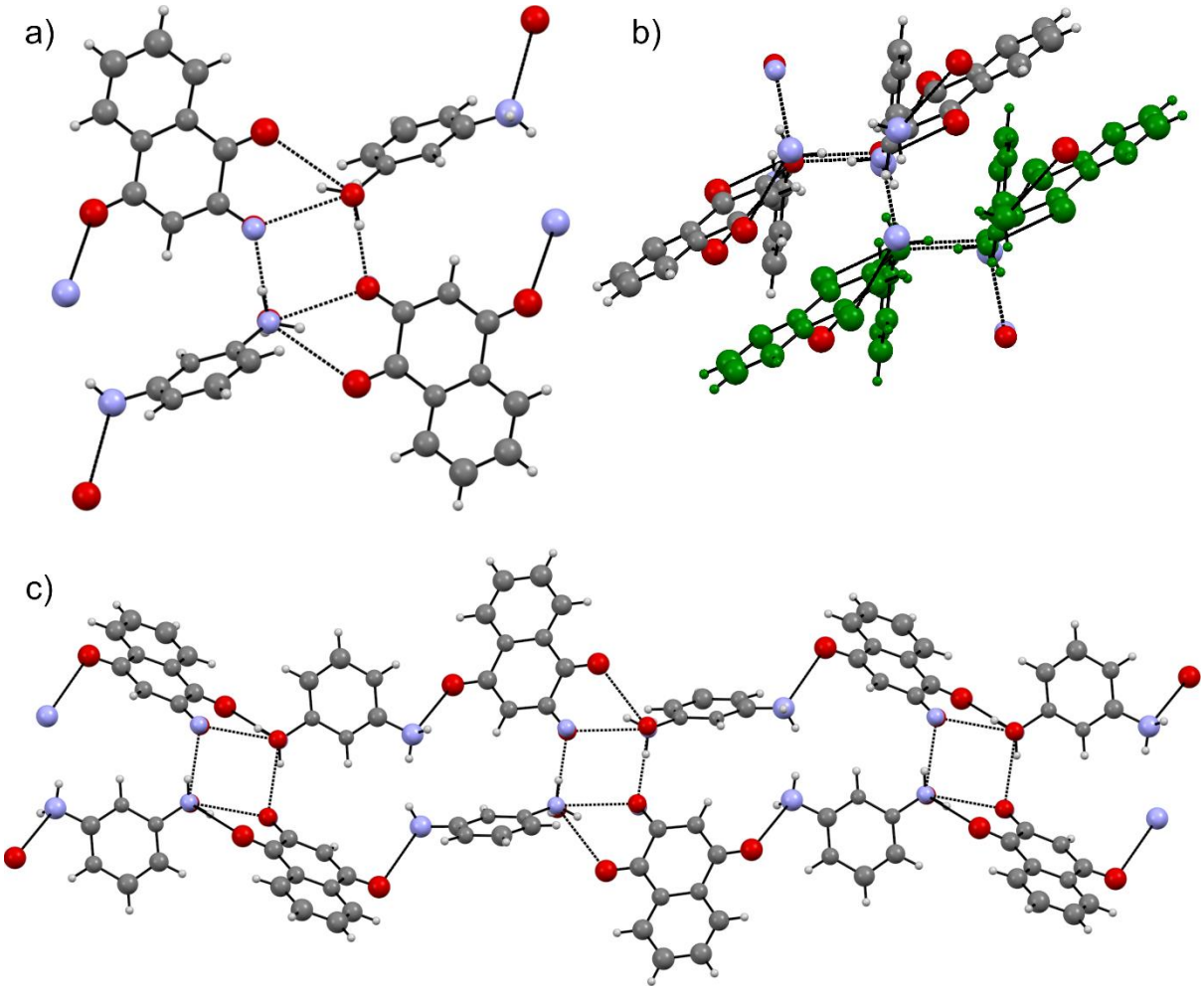

Figure 4.16: a) The hydrogen bonded network linking m-phenylenediamine and lawsone molecules together; b) another view of the hydrogen bonds between these two molecules showing the offset of the stacked rings; c) the extended structure of MPD-L showing the thermal ellipsoids at the 50% probability level.

4.3.3.4 Summary of OPD/MPD Series

Our co-crystallisation experiments, on the most part, resulted in the formation of salt forms of OPD and MPD, except for OPD-L which underwent a condensation reaction to form a single component phenazine based complex. Sebacic acid formed a 2:1 salt with OPD, but salt formation was not successful in the case of MPD. Trimesic acid formed salts with both OPD/MPD and lawsone only formed a salt with MPD. There are a series of salts of OPD with five aromatic acids in the literature which although do not utilise the same co-formers as we did, we can compare with our structures.[16] These organic salts largely interact through O–H···N hydrogen bonds with only one of the amine groups hydrogen bonding, the other amine group is redundant which we also observed in our TMA structures. UV/Vis of the OPD salts shows a shifting in the colour predominantly a bathochromic shift, except for OPD-L which shifts to a lower wavelength. It should be noted that the shifts in colour of the salts are very minor compared with pure OPD/MPD. Another point to note is that these salt forms changed colour when exposed to the air most likely due to oxidation rather than a colour change as a result of salt formation as was experienced in the PPD work.

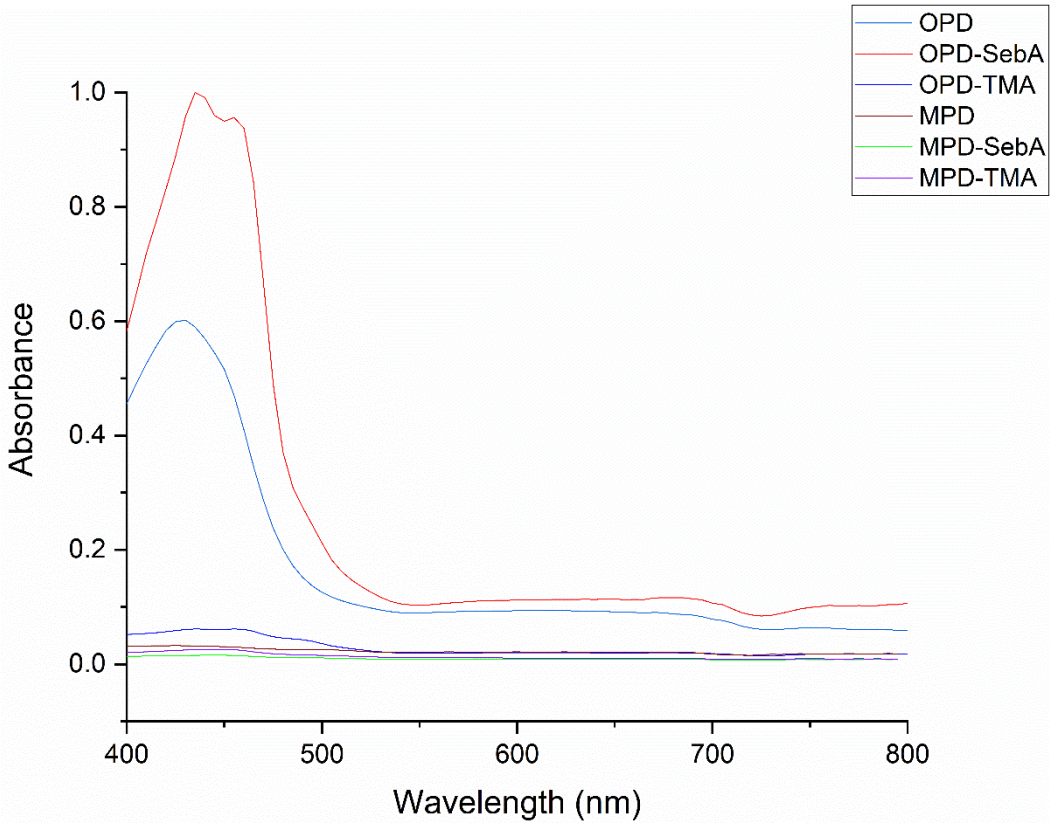

Figure 4.17: UV/Vis spectroscopy of the OPD and MPD series respectively in methanol

4.3.4 Co-crystallisation of 4IODAN

4-iodoaniline (4IODAN) was investigated as part of this study to study the change in the electronic structure with the change to iodine from amine moiety. The other reason was because it has been shown to display coloured multi-component forms with a range of co-formers when the starting materials were colourless.[23] This peaked our interest with this system and co-crystallisation conducted using the same approaches as above.

4.3.4.1 4-iodoaniline: Sebacic Acid

Co-crystallisation experiments between 4IODAN and SebA from LAG were ball-milled at a frequency of 30 Hz for 30 minutes, which resulted in mixtures of the two components in all cases as shown below in (Figure 4.18). All of the peaks in the ball-milled pattern can be attributed to either 4IODAN or SebA, there are no hints of any new peaks that would signify the presence of a new phase. Evaporative crystallisation experiments were also attempted, but this resulted in crystals of sebacic acid from a 1:1 ratio in methanol.

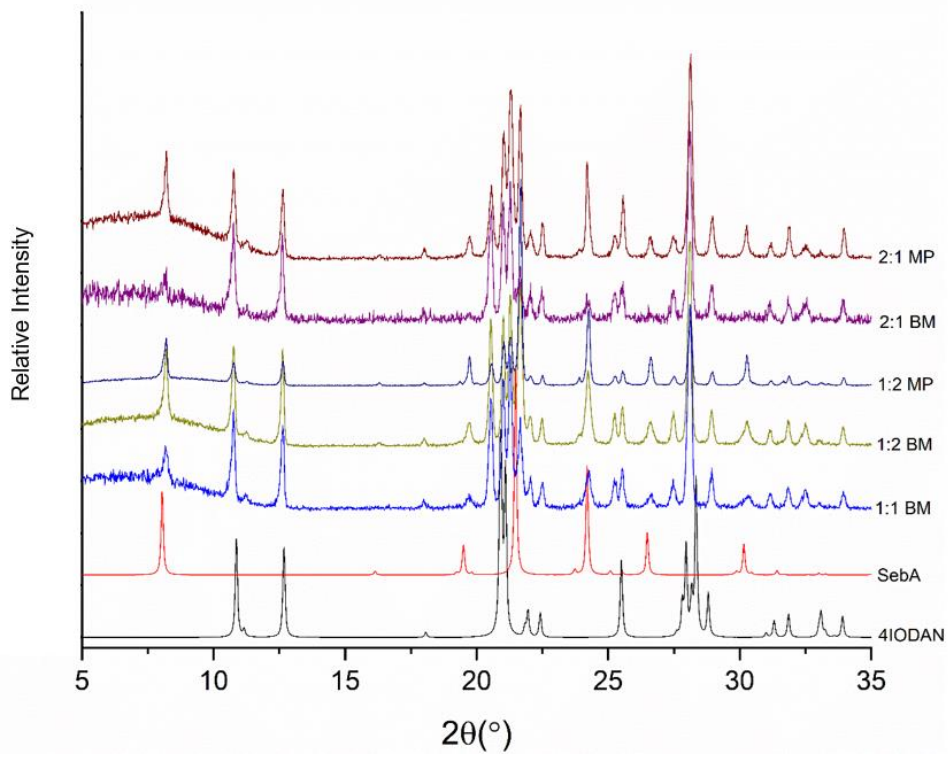

Figure 4.18: The PXRD pattern of 4IODAN-SebA from methanol compared with the simulated patterns for 4IODAN and SebA.

4.3.4.2 4-iodoaniline: Trimesic Acid

The PXRD patterns from LAG experiments (Figure 4.19) appear to indicate the presence of a mixture of 4IODAN and TMA. The DSC trace of the ball-milled powder (Figure 4.19) shows several endothermic events, most notably is the small broad endotherm with an onset temperature of 312.3 °C, corresponding to a phase transition at a very similar temperature to that of α-TMA, followed by another small broad endotherm with an onset temperature of 344.8 °C which corresponds to the melting of the material.

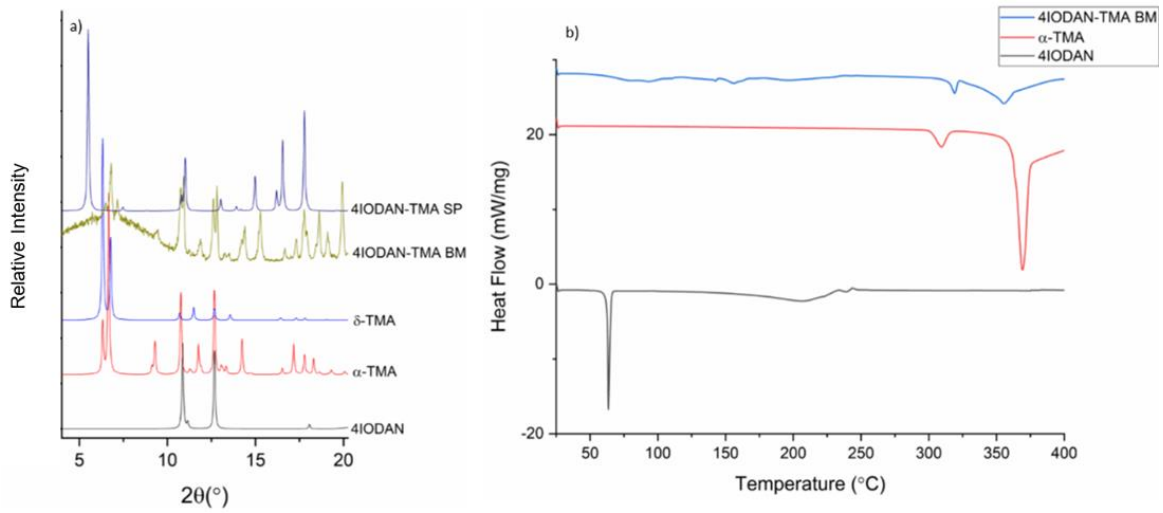

Figure 4.19: a) The PXRD pattern from 4IODAN-TMA BM from methanol compared with the simulated patterns of 4IODAN, α-TMA, δ-TMA and 4IODAN-TMA from the single crystal experiment; b) the DSC trace of 4IODAN-TMA BM compared with the traces of 4IODAN and α-TMA.

Evaporative crystallisation from methanol yielded a 4IODAN-TMA (1:1) salt hydrate co-crystallising in the monoclinic space group $P2_1/c$ with the asymmetric unit containing one molecule of 4-iodoaniline, one molecule of trimesic acid and one molecule of water. The three molecules are connected through a weak O–H···O (2.751(3) Å) hydrogen bond between the water molecule and TMA and an O–H···N^+ (2.777(4) Å) hydrogen bond between the water molecule and the protonated amine forming a $D_2^2 4$ graph set motif. The powder pattern of the ball-milled product and the simulated powder pattern of the phase obtained from evaporation are clearly different phases. In our ball-milling experiments, we had very small quantities of methanol (approx. 50 μL) in comparison to 5 mL in the evaporative crystallisation which is an important factor in the experimental outcome when considering that the ball-mill is a closed system compared with solution crystallisation. Since the ball-mill is a closed system, the material cannot uptake water to yield the hydrated salt form that could take place in solution crystallisation which is open to the air indicating why we have not observed the salt hydrate through milling as well as solution.

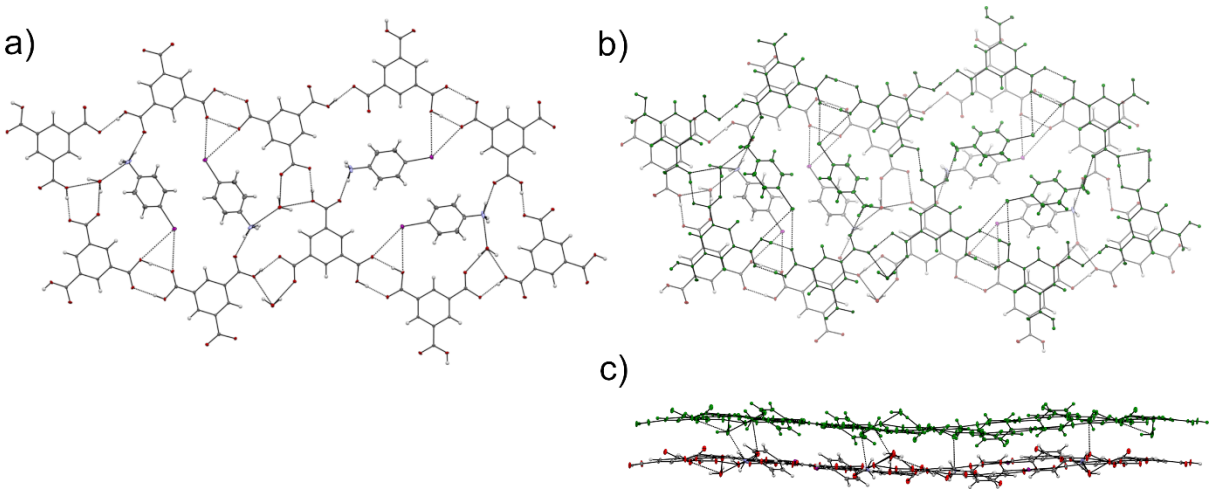

Figure 4.20: a) and b) The hydrogen bonding network of the 4IODAN-TMA (1:1) salt hydrate with the molecules highlighted in green showing the molecules overlaid ; c) the packing showing the π-π stacking interactions between the rings.

4.3.4.3 4-iodoaniline: Lawsone

Solution crystallisation of 4IODAN-L resulted in the formation of a single component material, where 4IODAN and L molecules reacted through a condensation reaction. The material crystallises in the orthorhombic space group *Fdd*2 containing one molecule in the asymmetric unit lying in general positions. The molecules are connected through a strong O–H···N (2.889(8) Å) hydrogen bond resulting in the formation of $C_1^1 6$ graph sets.

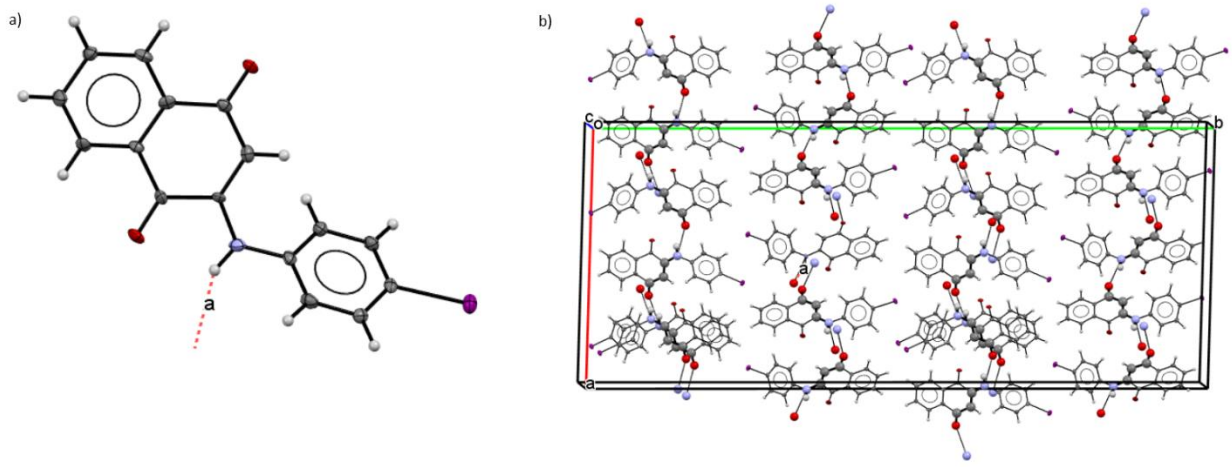

Figure 4.21: a) The crystal structure of 4IODAN-L determined at −173.13 °C; b) the packing arrangement of 4IODAN-L showing the thermal ellipsoids at the 50% probability level.

Liquid-assisted grinding (LAG) was carried out to investigate whether this material could also be formed via grinding. In this case, grinding was performed using a mortar and pestle rather than using a ball-mill as this approach had been shown to be successful in generating new co-crystals of 4-iodoaniline.[22] The two powder patterns from the ground material (Figure 4.22) indicates that both are mixtures of 4IODAN and L triclinic. Comparison with the simulated PXRD from the solution

crystallisation reveals a completely different pattern confirming that solution and grinding result in two completely different outcomes. The DSC trace of the ground material (Figure 4.22) shows a single endothermic event with an onset temperature of 233.8 °C which corresponds to the melting of this phase. However, we would have expected to see melts for both 4IODAN and L triclinic in the DSC since the PXRD pattern is a physical mixture of these two forms.

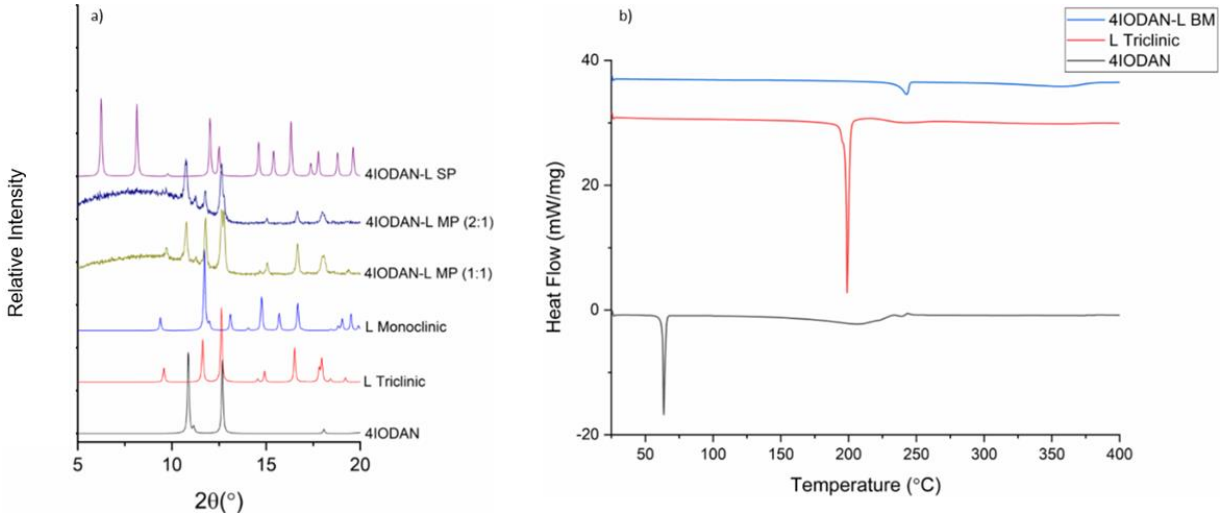

Figure 4.22: a) The PXRD pattern of 4IODAN-L MP from methanol compared with the simulated patterns for 4IODAN, L triclinic, L monoclinic and 4IODAN-L; b) the DSC trace of the ground material compared with the traces for 4IODAN and L triclinic.

4.4 Conclusions

This work has resulted in the formation of several new salt forms of OPD, MPD and 4IODAN as well as an HCl salt of PPD. The PPD salt resulted in a colour change in solution, so ionic co-crystals of PPD were attempted by both solution crystallisation and milling to further explore this colour change through ionisation, however, these were unsuccessful. Co-crystallisation of OPD and MPD largely resulted in new salt forms which were shown to have undergone a bathochromic shift with respect to the starting materials, however, these shifts in colour occurred over time rather than upon formation of the salts suggesting that this is a consequence of oxidation. Co-crystallisation of 4IODAN resulted in a new salt form with TMA, however, no colour change was observed. The work on 4IODAN multi-component with the presence of iodine appeared to impact on the reactivity with the 4IODAN-L system undergoing a condensation reaction which was not observed in the case of OPD and MPD.

4.5 References

1. Santos, A. F. L. O. M. & Ribeiro Da Silva, M. A. V. Diaminobenzenes: An experimental and computational study. *J. Phys. Chem. B* **115**, 4939–4948 (2011).

2. Ko, H. Y., Lin, Y. H., Shih, C. J. & Chen, Y. L. Determination of phenylenediamines in hair colors derivatizated with 5-(4, 6-dichlorotriazinyl)aminofluorescein via micellar electrokinetic chromatography. *J. Food Drug Anal.* **27**, 825–831 (2019).

3. María-Hormigos, R., Jurado-Sánchez, B. & Escarpa, A. Self-Propelled Micromotors for Naked-Eye Detection of Phenylenediamines Isomers. *Anal. Chem.* **90**, 9830–9837 (2018).

4. Meyer, A. & Fischer, K. Oxidative transformation processes and products of para-phenylenediamine (PPD) and para-toluenediamine (PTD)—a review. *Environ. Sci. Eur.* **27**, (2015).

5. Thomas, L. H., Klapwijk, A. R., Wales, C. & Wilson, C. C. Intermolecular hydrogen transfer and solubility tuning in multi-component molecular crystals of the API piroxicam. *CrystEngComm* **16**, 5924–5932 (2014).

6. Wicker, J. G. P., Crowley, L. M., Robshaw, O., Little, E. J., Stokes, S. P., Cooper, R. I. & Lawrence, S. E. Will they co-crystallize? *CrystEngComm* **19**, 5336–5340 (2017).

7. Agnew, L. R., Cruickshank, D. L., McGlone, T. & Wilson, C. C. Controlled production of the elusive metastable form II of acetaminophen (paracetamol): A fully scalable templating approach in a cooling environment. *Chem. Commun.* **52**, 7368–7371 (2016).

8. Pando, C., Cabañas, A. & Cuadra, I. A. Preparation of pharmaceutical co-crystals through sustainable processes using supercritical carbon dioxide: A review. *RSC Advances* **6**, 71134–71150 (2016).

9. Aakeröy, C. B., Fasulo, M. E. & Desper, J. Cocrystal or salt: Does it really matter? *Mol. Pharm.* **4**, 317–322 (2007).

10. Casali, L., Mazzei, L., Shemchuk, O., Honer, K., Grepioni, F., Ciurli, S., Braga, D. & Baltrusaitis, J. Smart urea ionic co-crystals with enhanced urease inhibition activity for improved nitrogen cycle management. *Chem. Commun.* **54**, 7637–7640 (2018).

11. Song, L., Shemchuk, O., Robeyns, K., Braga, D., Grepioni, F. & Leyssens, T. Ionic Cocrystals of Etiracetam and Levetiracetam: The Importance of Chirality for Ionic Cocrystals. *Cryst. Growth Des.* **19**, 2446–2454 (2019).

12. Shemchuk, O., André, V., Duarte, M. T., Braga, D. & Grepioni, F. Mechanochemical preparation of molecular and ionic co-crystals of the hormone melatonin. *CrystEngComm* **21**, 2949–2954 (2019).

13. Shemchuk, O., Degli Esposti, L., Grepioni, F. & Braga, D. Ionic co-crystals of enantiopure and racemic histidine with calcium halides. *CrystEngComm* **19**, 6267–6273 (2017).

14. Braga, D., Grepioni, F. & Shemchuk, O. Organic-inorganic ionic co-crystals: a new class of multipurpose compounds. *CrystEngComm* **20**, 2212–2220 (2018).

15. Czapik, A. & Gdaniec, M. A new polymorph of benzene-1,2-diamine: Isomorphism with 2-amino-phenol and two-dimensional iso-structurality of polymorphs. *Acta Crystallogr. Sect. C Cryst. Struct. Commun.* **66**, (2010).

16. Mishra, R. & Pallepogu, R. Supramolecular heterosynthon assemblies of ortho-phenylenediamine with substituted aromatic carboxylic acids. *Acta Crystallogr. Sect. B-Structural Sci. Cryst. Eng. Mater.* **74**, 32–41 (2018).

17. Caira, M. R., Horne, A., Nassimbeni, L. R., Okudab, K. & Todab, F. Selective inclusion of phenylenediamine isomers by 1 ,l-bis(4-hydroxypheny1)cyclohexane. *J. Chem. Soc. Perkin Trans. 2* 1063–1067 (1995).

18. Goswami, S., Mukherjee, R., Nigam, G. D., Chinnakali, K. & Fun, H. K. o-Phenylenediamine pyrocatechol hemihydrate complex. *Acta Crystallogr. Sect. C Cryst. Struct. Commun.* **54**, 1647–1649 (1998).

19. Betz, R., Klüfers, P. & Mayer, P. *m*-Phenylenediamine. *Acta Crystallogr. Sect. E Struct. Reports Online* **64**, o2501–o2501 (2008).

20. Anderson, K. M., Goeta, A. E., Hancock, K. S. B. & Steed, J. W. Unusual variations in the incidence of Z ' > 1 in oxo-anion structures. *Chem. Commun.* 2138–2140 (2006).

21. Dey, A., Jetti, R. K. R., Boese, R. & Desiraju, G. R. Supramolecular equivalence of halogen, ethynyl and hydroxy groups. A comparison of the crystal structures of some 4-substituted anilines. *CrystEngComm **5**, 248-252* (2003).

22. Mukherjee, A., Dixit, K., Sarma, S. P. & Desiraju, G. R. Aniline-phenol recognition: from solution through supramolecular synthons to cocrystals. *IUCrJ* **1**, 228–239 (2014).

23. Jones, C. L., Wilson, C. C. & Thomas, L. H. Turning colour on and off using molecular disorder and proton transfer in multi-component molecular complexes. *CrystEngComm* **16**, 5849–5858

(2014).

24. Delori, A., Urquhart, A. J. & Oswald, I. D. H. Supramolecular hair dyes: A new application of cocrystallization. *CrystEngComm* **18**, 5360–5364 (2016).

25. Cosier, B. J. & Glazer, A. M. A Nitrogen-gas-stream cryostat for general X-ray diffraction studies. *J. Appl. Crystallogr.* **19**, 105–107 (1986).

26. Bruker. APEX3. *APEX3; SAINT* (2016).

27. Sheldrick, G. M. SADABS program for area detector absorption correction. (2008).

28. Dolomanov, O. V., Bourhis, L. J., Gildea, R. J., Howard, J. K. & Puschmann, H. *OLEX2* : a complete structure solution, refinement and analysis program. *J. Appl. Crystallogr.* **42**, 339–341 (2009).

29. Sheldrick, G. M. SHELXT - Integrated space-group and crystal-structure determination. *Acta Crystallogr. A-Foundation Adv.* **71**, 3–8 (2015).

30. Sheldrick, G. M. Crystal structure refinement with SHELXL. *Acta Crystallogr. Sect. C Struct. Chem.* **71**, 3–8 (2015).

31. Chandrasekaran, R. Crystal structure of *p*-phenylenediamine dihydrochloride. *Acta Cryst. B* 369–374 (1969).

32. Morrison, J. D. & Robertson, J. M. The crystal and molecular structure of certain dicarboxylic acids. Part VI. Sebacic acid. *J. Chem. Soc.* 993–1001 (1949).

33. Duchamp, D. J. & Marsh, R. E. The crystal structure of trimesic acid (benzene-1,3,5-tricarboxylic acid). *Acta Crystallogr. Sect. B Struct. Crystallogr. Cryst. Chem.* **25**, 5–19 (1969).

34. Dale, S. H., Elsegood, M. R. J., Hemmings, M. & Wilkinson, A. L. The co-crystallisation of pyridine with benzenepolycarboxylic acids: The interplay of strong and weak hydrogen bonding motifs. *CrystEngComm* **6**, 207–214 (2004).

35. Vishweshwar, P., Beauchamp, D. A. & Zaworotko, M. J. An acetic acid solvate of trimesic acid that exhibits triple inclined interpenetration and mixed supramolecular homosynthons. *Cryst. Growth Des.* **6**, 2429–2431 (2006).

36. Nath, K. G., Ivasenko, O., MacLeod, J. M., Miwa, J. A., Wuest, J. D., Nanci, A., Perepichka, D. F. & Rosei, F. Crystal engineering in two dimensions: An approach to molecular nanopatterning. *J. Phys. Chem. C* **111**, 16996–17007 (2007).

37. Berns, S., Hernández, G., Portillo, R. & Gutiérrez, R. Trimesic acid dimethyl sulfoxide solvate: Space group revision. *Acta Crystallogr. Sect. E Struct. Reports Online* **64**, (2008).

38. Ward, M. R. & Oswald, I. D. H. Hidden solvates and transient forms of trimesic acid. *Crystals* **10**, 1–13 (2020).

39. Herbstein, F. H., Kapon, M. & Reisner, G. M. Trimesic acid, its hydrates, complexes and polymorphism. VIII. Interstitial complexes of *α*- and (the hypothetical) *γ*-trimesic acid. *Acta Crystallogr. Sect. B* **41**, 348–354 (1985).

40. Cui, P., McMahon, D. P., Spackman, P. R., Alston, B. M., Little, M. A., Day, G. M. & Cooper, A. I. Mining predicted crystal structure landscapes with high throughput crystallisation: Old molecules, new insights. *Chem. Sci.* **10**, 9988–9997 (2019).

41. Todkary, A. V., Dalvi, R., Salunke-Gawali, S., Linares, J., Varret, F., Marrot, J., Yakhmi, J. V., Bhadbhade, M., Srinivas, D., Gejji, S. P. & Rane, S. Y. SOM assembly of hydroxynaphthoquinone and its oxime: Polymorphic X-ray structures and EPR studies. *Spectrochim. Acta - Part A Mol. Biomol. Spectrosc.* **63**, 130–138 (2006).

42. Dekkers, J., Kooijman, H., Kroon, J. & Grech, E. 2-hydroxy-1,4-naphthoquinone. *Acta Crystallogr. Sect. C Cryst. Struct. Commun.* **52**, 2896–2899 (1996).

43. Wang, G. W. Mechanochemical organic synthesis. *Chem. Soc. Rev.* **42**, 7668–7700 (2013).

44. Vetr, F., Moradi-Shoeili, Z. & Özkar, S. Oxidation of *o*-phenylenediamine to 2,3-diaminophenazine in the presence of cubic ferrites MFe_2O_4 (M = Mn, Co, Ni, Zn) and the application in colorimetric detection of H_2O_2. *Appl. Organomet. Chem.* **32**, (2018).

Chapter Five – Alizarin Co-crystals

5 Alizarin Co-crystals

The main aim of this chapter is to explore the co-crystallisation of alizarin and hopefully provide a safer alternative to PPD for future supramolecular hair dyes. Alizarin was selected as we had some in our lab and because its part of the anthraquinone family and is extracted from plants. The co-formers (all pyrazine based derivatives) were chosen based on the supramolecular synthon approach. The colour and hair dyeing ability of these systems will be investigated following co-crystallisation experiments.

5.1 Introduction

Anthraquinones (AQ's) are a class of functionally diverse aromatic chemicals structurally related to anthracene which are used in the treatment of fungal skin diseases and are also used as laxatives.[1] Synthetic and natural AQ's have widespread applications across the medical and chemical industries because of their wide ranging therapeutic and pharmacological properties including antioxidant, anti-inflammatory, anticancer, antimicrobial, immunosuppressive, *etc.*[2-3] Previous studies on AQ's in the solid state have reported several solvates[4], hydrates[5-6] and co-crystals[7-8]. Multi-component forms are well known to alter the physical and chemical properties, *e.g.* melting point, phase transition temperature, solubility, stability, colour, *etc*.[9] Co-crystallisation is seen as a method of crystal engineering where the solid is 'designed' rather than hydrate/solvate formation, that for the most part, is serendipitous.[10] Co-crystals can be classed as crystalline materials comprised of at least two distinctly neutral components that are solids at ambient conditions and which are present in stoichiometric amounts.[11] These solid forms have applications in agrochemicals[12], neutraceuticals[13], pharmaceuticals[14] and energetic materials[15] as a result of their ability to engineer critical physical and chemical properties.[16] One successful route to the discovery of novel co-crystalline materials has been mechanochemistry.

Mechanochemistry is associated with chemical transformations initiated by mechanical means, *i.e.* shear, friction or compression.[17] It is well known that chemical reactions initiated via different forms of energy can result in different products and yield access to reactions that may be inaccessible through other means.[18] Mechanochemistry has been highlighted as an excellent approach to efficiently and rapidly screen for new pharmaceutical materials including salts[19], co-crystals[20] and solvates[21]. For the synthesis of multi-component materials via grinding there are two main approaches, neat grinding and liquid assisted grinding (LAG).[22] Neat grinding refers to grinding the two components in the absence of solvent whereas LAG utilises catalytic amounts of liquid to facilitate mechanically induced reactions that either occur slowly through neat grinding or do not occur at all.[23-24] Belengeur *et al.* has demonstrated that LAG experiments can yield different

products depending on the quantity of solvent used.[25] From the perspective of anthraquinone solid forms, none of those reported have been obtained through grinding, however co-crystals of other pigments, *e.g.* fluorescein, have been isolated through these methods.[20]

Alizarin (1,2-dihydroxy-9,10-anthraquinone) is isolated from the roots of the Rubia tinctorum plant and is one of the most stable organic pigments which is mainly used for colouring textiles, but also has applications in solar energy conversion, medicine and metal detection.[26] We selected alizarin as the molecule of interest mainly due to its simplistic structure compared to other AQ's (to aid structure solution in the case of failing to obtain a single crystal), but also because of the presence of hydroxyl groups which can hydrogen bond with pyridine based co-formers using the supramolecular synthon approach.[27] These pyridine based co-formers (pyrazine, PYR; and acridine, ACR) have been utilised as successful co-crystallisation reactants through the use of the O−H···N supramolecular synthon. Alizarin has two known polymorphic forms which were reportedly crystallised through slow evaporation and vapour growth techniques. Form I was obtained through vapour growth/solvent evaporation from methanol/ethanol solutions, whereas Form II resulted from toluene solutions. The crystal structures of the two forms show significant disorder as well as being twinned trough reticular pseudomerohedry.[28] The crystal packing of the two polymorphs (*Figure 5.1*) shows significantly more disorder in Form I with the only hydrogen bonding interaction forming weak O−H···O (2.605(3) Å) hydrogen bonds between adjacent oxygen atoms resulting in an $S_1^1 6$ graph set. In comparison, Form II results in an additional O−H···O (2.712(4) Å) hydrogen bond between alizarin molecules forming $C_1^1 8$ graph sets. Both polymorphic forms show very similar crystal packing in a herringbone arrangement exhibiting π-π stacking between the alizarin molecules.

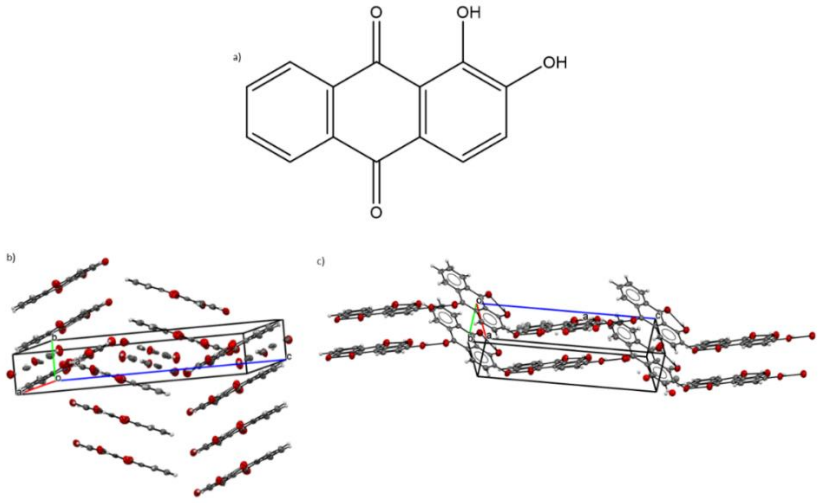

Figure 5.1: a) The chemical structure of alizarin (1,2-dihydroxy-9,10-anthraquinone); b) and c) the crystal packing of ALZ Form I (CSD:DHYANT01) and ALZ Form II (CSD: DHYANT02) showing the thermal ellipsoids at the 50% probability level.

In this study, the aim was to prepare a series of novel multi-component materials of ALZ with varying colours which could subsequently be used as supramolecular hair dyes. This study would hopefully increase the range of available colours compared with the previously formed supramolecular hair dyes.[9]

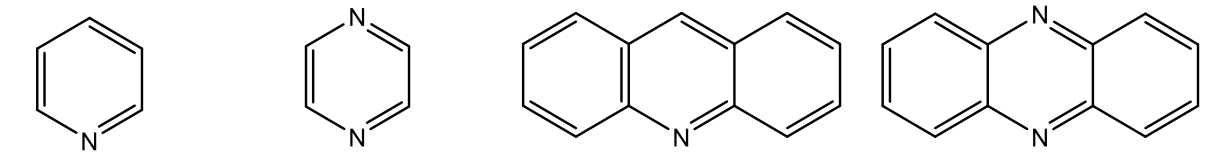

Pyridine (PYRD) Pyrazine (PYR) Acridine (ACR) Phenazine (PHN)

Scheme 5.1: Chemical structures of the co-formers used in co-crystallisation experiments with ALZ.

5.2 Materials & Methods

5.2.1 Materials

ALZ (purity 97%, Lot No. MKBJ8931V) and ACR (purity 97%, Lot No. BCBV4712) were obtained from Sigma-Aldrich, whereas PYR (purity 98%, Lot No. P22C018) and PHN (purity ≥99%, Lot No. E5846A) were obtained from Alfa Aesar. Ethanol absolute (purity ≥99.8%, Lot No. 1871407) and pyridine (purity ≥99.8%, Lot No. STBG0080V) were obtained from Fischer Scientific and Honeywell Research Chemicals respectively. All materials were used as received without any further purification.

5.2.2 Liquid Assisted Grinding (LAG)

LAG experiments were carried out using a Retsch MM400 mechanical mill equipped with 10 mL stainless steel grinding jars and two 7 mm steel balls per jar. A small quantity of ethanol (approx. 50 μL) was added and the milling process was carried out at a frequency of 30 Hz for 30 minutes.

Table 5.1: List of weights of each component used in LAG experiments.

	Weight of Alizarin (mg; mmol)	Weight of Co-Former (mg; mmol)
ALZ-PYR	120.4; 0.501	39.2; 0.489
ALZ-ACR	121.5; 0.506	93.8; 0.523
ALZ-PHN	135.1; 0.562	104.0; 0.577

5.2.3 Solution Crystallisation

ALZ-PYRD (1): A saturated solution of ALZ (250.3 mg, 1.042 mmol) was prepared in 10 mL of pyridine. The solution was filtered through a 0.22 μm filter before being left to slowly evaporate in the fume cupboard at approximately 19 °C – 22 °C. The sample crystallised after several months as orange needles of suitable quality for single crystal X-ray diffraction.

ALZ-PYR (2): The following method is to the best of our knowledge, the conditions used, however, we cannot be definitely sure of this. Approximately 50 mg of ball-milled powder created by procedure in 5.2.2 was dissolved in 0.5 mL of 1,4-dioxane. The solution was then heated from 15 °C to 60 °C at a rate of 0.3 °C or 0.5 °C/min, followed by cooling to 15 °C at 0.2 °C or 0.3 °C/min. The sample crystallised as light orange needles of suitable quality for single crystal X-ray diffraction.

ALZ-ACR (3): A saturated solution of ALZ (21.9 mg, 0.0912 mmol) and ACR (1.195 g, 6.668 mmol) was prepared in 10 mL of ethanol. The solution was filtered through a 0.22 μm filter before being left to slowly evaporate at 23 °C. The sample crystallised after approximately two weeks as light orange needles of suitable quality for single crystal X-ray diffraction.

ALZ-PHN (4): A saturated solution of ALZ (27.8 mg, 0.116 mmol) and PHN (76.5 mg, 0.425 mmol) was prepared in 10 mL of ethanol. The solution was filtered through a 0.22 μm filter before being left to slowly evaporate at 23 °C. The sample crystallised after approximately one week as light orange needles of suitable quality for single crystal X-ray diffraction.

5.2.4 Single Crystal X-ray Diffraction (SC-XRD)

Single crystals were selected using a Leica M165 CX microscope and silicone oil was used as an adhesive to aid in mounting the single crystals. Diffraction data was collected on a Bruker Kappa Apex II Duo using Mo-Kα radiation (λ = 0.71073 Å), except for ALZ-PYR which was collected on a Bruker D8 Venture using Cu-Kα radiation (λ= 1.5406 Å). Both instruments were equipped with an Oxford cryosystems low temperature device operating at −173.13 °C.[29] Data reduction was performed using Bruker SAINT[30] and a multi-scan absorption correction was applied using SADABS[31]. The crystal structures were solved in Olex2[32] using SHELXT[33] and the model refined by full-matrix least squares against F^2 using all data (SHELXL[34]). All non-hydrogen atoms were refined anisotropically and the hydrogen atoms attached to carbon and oxygen were placed geometrically.

Table 5.2: Crystallographic data and structure refinement parameters.

	alz_pyridine_100k	alz_pyr_050819_0m	alz_acr_100k_01_0m	alz_phn_100k_01_0m_tw
Chemical formula	$C_{14}H_8O_4 \cdot C_5H_5N$	$2(C_{14}H_8O_4) \cdot C_4H_6N_2$	$C_{14}H_8O_4 \cdot C_{13}H_9N$	$2(C_{14}H_8O_4) \cdot C_{12}H_8N_2$
*M*r	319.30	562.51	419.42	660.61
Crystal system, space group	Orthorhombic, $Pna2_1$	Monoclinic, $P2_1/c$	Triclinic, $P\bar{1}$	Triclinic, $P\bar{1}$
Temperature (°C)	−173.13	22.85	−173.13	−173.13
a, *b*, *c* (Å)	14.5756(7), 26.0514(13), 3.7776(2)	7.7046(4), 3.8360(2), 41.668(3)	3.852(1), 12.600(3), 19.632(5)	3.7954(12), 12.580(4), 16.213(5)
α, *β*, *γ* (°)	90, 90, 90	90, 90.976(4), 90	97.595(6), 91.003(8), 95.242(7)	68.157(7), 83.543(7), 85.548(7)
V (Å^3)	1434.41(13)	1231.32(12)	940.1(4)	713.5(4)
Z	4	2	2	1
Radiation type	Mo-*Kα*	Cu-*Kα*	Mo-*Kα*	Mo-*Kα*
μ (mm^{-1})	0.11	0.92	0.10	0.11
Crystal size (mm)	0.62 × 0.04 × 0.04	0.72 × 0.02 × 0.02	0.88 × 0.02 × 0.02	0.78 × 0.02 × 0.02
Diffractometer	Bruker *APEX*-II CCD	Bruker D8 Venture	Bruker *APEX*-II CCD	Bruker *APEX*-II CCD
Absorption correction	Multi-scan *SADABS2016*/2 (Bruker,2016/2) was used for absorption correction. w*R*2(int) was 0.1319 before and 0.0521 after correction. The Ratio of minimum to maximum transmission is 0.7447. The $\lambda/2$ correction factor is Not present.	Multi-scan *SADABS2016*/2 (Bruker,2016/2) was used for absorption correction. w*R*2(int) was 0.1850 before and 0.0996 after correction. The Ratio of minimum to maximum transmission is 0.2389. The $\lambda/2$ correction factor is Not present.	Multi-scan *SADABS2016*/2 (Bruker,2016/2) was used for absorption correction. w*R*2(int) was 0.1474 before and 0.0824 after correction. The Ratio of minimum to maximum transmission is 0.5627. The $\lambda/2$ correction factor is Not present.	Multi-scan *SADABS2016*/2 (Bruker,2016/2) was used for absorption correction. w*R*2(int) was 0.1302 before and 0.0784 after correction. The Ratio of minimum to maximum transmission is 0.8093. The $\lambda/2$ correction factor is Not present.
T_{min}, T_{max}	0.555, 0.745	0.180, 0.754	0.419, 0.745	0.603, 0.745
No. of measured, independent and observed [$I > 2\sigma(I)$] reflections	13284, 2665, 2537	6155, 2402, 1606	8593, 3572, 2583	12790, 12790, 7715
R_{int}	0.041	0.102	0.057	0.073
$(\sin \vartheta/\lambda)_{max}$ (Å^{-1})	0.611	0.625	0.612	0.599
$R[F^2 > 2\sigma(F^2)]$, $wR(F^2)$, *S*	0.033, 0.092, 1.06	0.227, 0.555, 2.10	0.068, 0.197, 1.03	0.093, 0.213, 1.10
No. of reflections	2665	2402	3572	12790
No. of parameters	219	196	291	229
No. of restraints	1	0	0	0
H-atom treatment	H-atom parameters constrained	H atoms treated by a mixture of independent and constrained refinement	H-atom parameters constrained	H-atom parameters constrained
$\Delta\rho_{max}$, $\Delta\rho_{min}$ (e Å^{-3})	0.30, −0.19	0.84, −0.69	0.37, −0.37	0.41, −0.40
Absolute structure	Flack x determined using 975 quotients [(I+)-(I-)]/[(I+)+(I-)] (Parsons, Flack and Wagner, Acta Cryst. B69 (2013) 249-259).	-	–	–
Absolute structure parameter	0.7(4)	-	–	–

5.2.5 Powder X-ray Diffraction (PXRD)

The materials obtained from LAG experiments were analysed by PXRD. PXRD was carried out using a flat-plate transmission geometry multi-well Bruker D8 Advance II powder diffractometer using Cu-Kα radiation (λ = 1.5406 Å) at approximately 21 °C - 24 °C. Data was collected between a 2ϑ of 4-35°, a step size of 0.017° and S_1/step. Variable temperature (VT) was carried out for ALZ-PHN BM using a flat-plate reflection geometry (Bragg-Brentano) Bruker D8 Discover using Cu-Kα radiation equipped with a CHC+ Anton Paar variable temperature and humidity stage. Data was collected between a 2ϑ of 4-35°, a step size of 0.017° and S_1/step in 25 °C increments from 25 °C to 150 °C and in 10 °C increments from 150 °C to 210 °C with a collection time of 35 minutes.

5.2.6 Differential Scanning Calorimetry (DSC)

DSC was carried out using a Mettler Toledo DSC822e equipped with auto-sampler (TSO801RO). Approximately 1-4 mg of sample was loaded into a 40 μL aluminium crucible with a pierced aluminium lid before being crimped and loaded onto the calorimeter. Samples were then heated from 20 °C to 300 °C at a rate of 10 °C/min with a constant N_2 gas flow.

5.2.7 Thermogravimetric Analysis (TGA)

TGA was carried out using a Netzsch STA 449 F1 Jupiter. Approximately 2-3 mg of sample was loaded into a 25 μL aluminium crucible with a pierced aluminium lid before being crimped and loaded onto the carousel. The samples were heated from 20 °C to 300 °C at a rate of 10 °C/min, held constant for 30 minutes before being cooled to 20 °C at a rate of 10 °C/min.

5.2.8 Infrared Spectroscopy (FT-IR)

FT-IR spectra were acquired using a Shimadzu IRSpirit QATR-S in transmittance mode between 400-4000 cm^{-1}, a resolution of 4 cm^{-1} and averaged over 64 scans featuring a diamond ATR attachment.

5.2.9 UV/Visible Spectrometry (UV/Vis)

UV/Vis was carried out using a Cary 50 spectrophotometer with scans being acquired between 325-800 nm. Stock solutions of approximately 0.1% w/v were prepared in ethanol before being sufficiently diluted by a factor of 50 to yield an absorbance value of approximately 1.0.

5.2.10 Dyeing of Hair

Approximately (150-200 mg) of undyed yak hairs were immersed in hot water for approximately 2 minutes to swell the hairs. A paste was generated by adding a small volume of solvent (approx. 500-1000 μL) to a quantity of solid (approx. 250-500 mg) in a mortar and ground for several minutes. The hairs were mixed with the paste for 30, 45, 60 and 90 minutes before being thoroughly washed with hot soapy water at 50 °C. This method was adapted from the published method by Delori *et al.* in which yak hairs were used instead of human hairs and for generation of the paste, a small amount of liquid was added to the solid rather than a saturated solution of the salt/co-crystal.

5.3 Results and Discussion

5.3.1 Effects of Ball Milling on Starting Materials

Prior to our multi-component LAG experiments, the starting materials were ball-milled using identical milling conditions as the multi-component experiments to determine whether the starting materials would undergo any transformations during the process. Our results very clearly indicate that in all cases, the fresh solid from the bottle remains the same form after 30 minutes of grinding at 30 Hz in ethanol (Figure 5.2). After ball-milling, alizarin remained as Form II, PYR converted to Form III, ACR remained as Form III and PHN remained as the α-form. If any new crystalline forms are obtained via this approach in section 5.3.2, then this will be due to the formation of a new co-crystalline material rather than new single component materials.

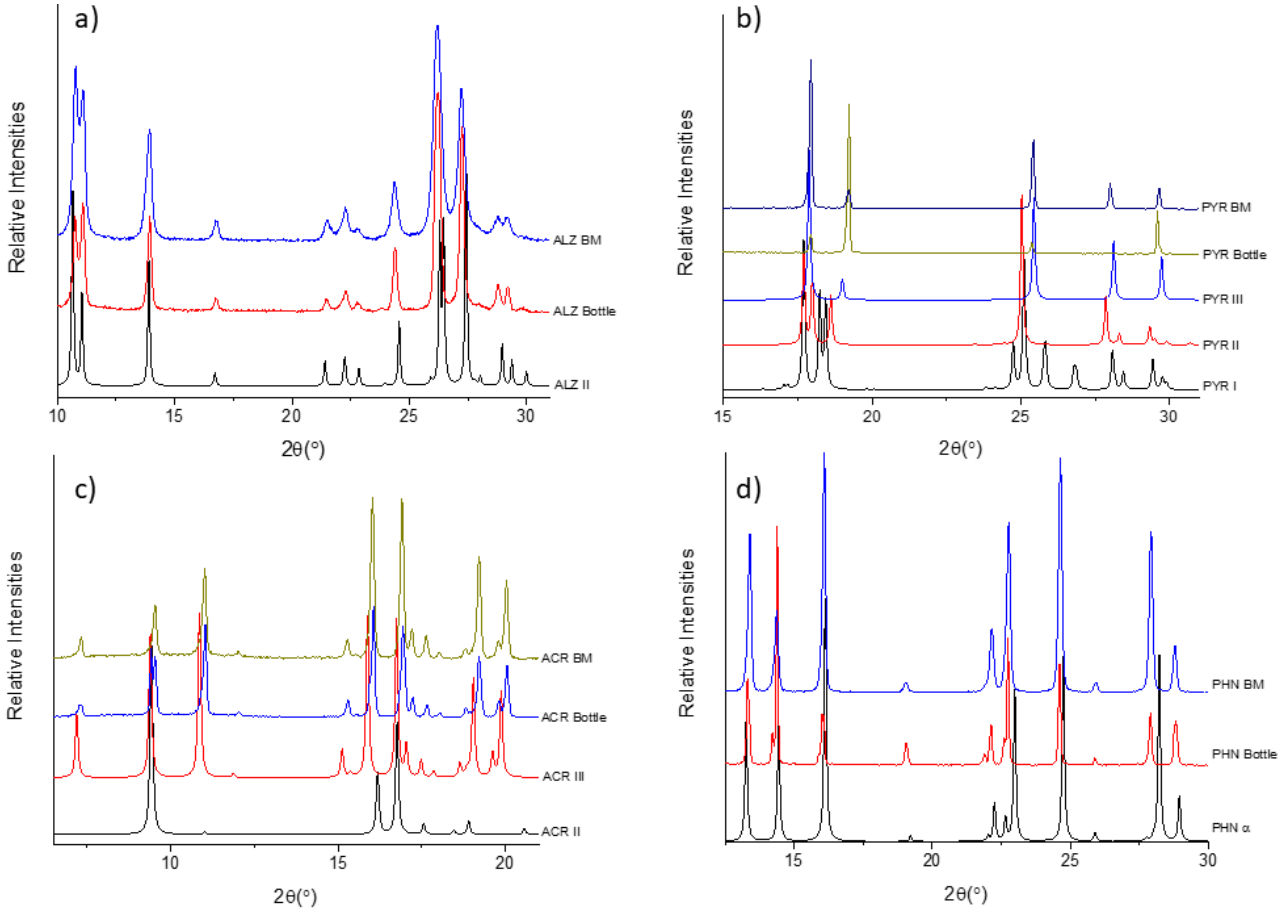

Figure 5.2: The PXRD pattern of: a) ALZ BM compared with the simulated patterns of ALZ Form II and pure ALZ, no diffraction until 10° 2ϑ; b) PYR BM compared with the simulated patterns of PYR Forms I, II, III and pure PYR, no diffraction until 17.5° 2ϑ. From these patterns, we can conclude that the starting material is PYR Form III; c) ACR BM compared with the simulated patterns of ACR Forms II, III and pure ACR, no diffraction until 8° 2ϑ. The data shows that the unprocessed powder is ACR Form III; d) PHN BM compared with the simulated patterns of PHN α and pure PHN, no diffraction until 12.5° 2ϑ.

5.3.2 Co-crystallisation of Alizarin

5.3.2.1 *Alizarin:* Pyridine

As a starting point to this study, we investigated the crystallisation from a pure pyridine solvent. This has been successfully performed on a number of other systems as the binary system reduces the complexity of the system and enables the greatest opportunity for co-crystallisation.[35] From the solution, we were able to isolate a new pyridine solvate which is inherently unstable at 25 °C. The diffraction pattern from the ambient temperature data collection rapidly deteriorated within two and a half hours leading us to believe that de-solvation results in the collapsing of the structure, although further analysis would be required to confirm this. Despite the reduced data collection time, we were able to identify and solve the structure with the unit cell parameters: *a* = 3.912(7) Å, *b* = 14.72(2) Å, *c* = 26.40(4) Å in the orthorhombic space group *Pn*. The identity of the solid was confirmed when the data was collected at −173.13 °C which in fact solved in $Pna2_1$ rather than *Pn* most likely due to the lack of data collected at ambient temperature. The crystal structure of the pyridine solvate contains one molecule of alizarin and one molecule of pyridine in the asymmetric unit lying in general positions with the two molecules connected through strong O−H···N (2.657(3) Å) hydrogen bonds forming $D_1^1 2$ graph set motifs. There are also short contact interactions (*Figure 5.3*a) linking alizarin molecules together through weak O−H···O hydrogen bonds propagating throughout the structure. The crystal packing arrangement (*Figure 5.3*b) shows a typical herringbone type arrangement with the molecules forming a V shape which results in π-π stacking interactions between the alizarin and pyridine molecules.

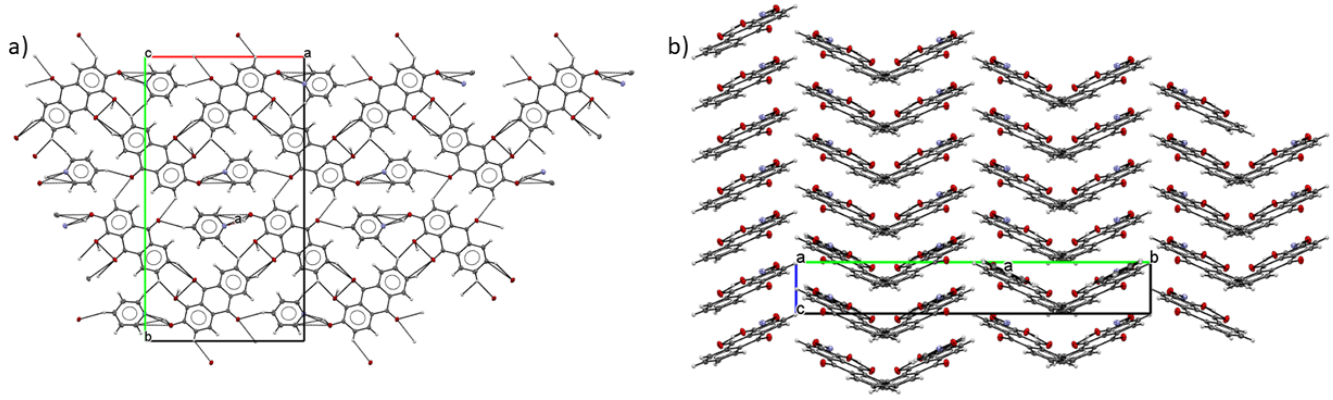

Figure 5.3: a) The hydrogen-bonded network of short contact interactions viewed along the crystallographic *c*-direction; b) the crystal packing arrangement of the ALZ pyridine solvate viewed along the crystallographic *a*-direction showing the thermal ellipsoids at the 50% probability level.

5.3.2.2 Alizarin: Pyrazine

5.3.2.2.1 Polymorphism of Pyrazine

For us to be able to understand the formation of a new crystalline form, we need to understand the polymorphism of Pyrazine by itself to identify possible transitions that might occur on manipulating the solids. Pyrazine has four polymorphic forms that can be obtained through the modification of pressure and temperature.[36] The most stable form under ambient temperature conditions is Form III hence it is likely that this form will be observed.[37] Forms I and II are high temperature forms which were obtained from melt crystallisation, but the isolation of the two forms depended on the rate of cooling. On fast cooling (360 °C/h), Patyk *et al.* were able to isolate Form I whilst slower cooling (100 °C/h) was used to access Form II. Their DSC measurements showed that Form II was always accessed at a heating and cooling rate of 5 °C/min leading them to conclude that Form I is a metastable phase at ambient temperature and hence Forms II and III are enantiotropically related. Our DSC measurements (*Figure 5.4*) show that PYR Form III undergoes a phase transformation at approx. 30 °C followed by the melting of this phase believed to be Form II at approx. 50 °C which conforms with the literature. Form IV of pyrazine can be accessed through high-pressure routes at 1.1 gigapascals (GPa) and 22 °C.[36] There is evidence to suggest that the temperature inside a ball-mill can be influenced by the milling balls material, diameter as well as the operating frequency, volume and material of the grinding jars.[38] It has been reported that 30 minutes of milling can result in a temperature as high as 50 °C.[39 -40] This gives rise to the potential of also observing Forms I and II during our milling experiments.

5.3.2.2.2 Characterisation of Alizarin: Pyrazine Co-crystal

As we have been discussing, pyrazine is a solid under ambient conditions hence co-crystallisation through ball-milling is a viable route to a new product. The powder diffraction pattern from ball-milling (*Figure 5.4*) reveals the presence of several new peaks which cannot be attributed to the starting materials. The DSC trace of the ball-milled powder (*Figure 5.4*) features two endothermic events, firstly, a broad endotherm with an onset temperature of 73.8 °C corresponding with the decomposition of PYR. The second endotherm corresponds to the melt of this material with an onset temperature of 287.1 °C and the melt occurring at 290.1 °C which is identical to that of ALZ Form II. The TGA trace (*Figure 5.4*) shows an initial weight loss of 13% at approximately 70 °C, followed by decomposition around the melting point of ALZ. This indicates that the weight loss of 13% is a result of PYR being ejected from the crystal, leaving ALZ which then melts. The DSC/TGA traces indicate that the sample is a mixture of the two components, as no new thermal events corresponding to the melting of a new crystal form have been observed. However, the powder

diffraction pattern indicates that although there are very few reflections from the starting materials, this pattern is representative of a new phase with a small amount of unreacted material as well.

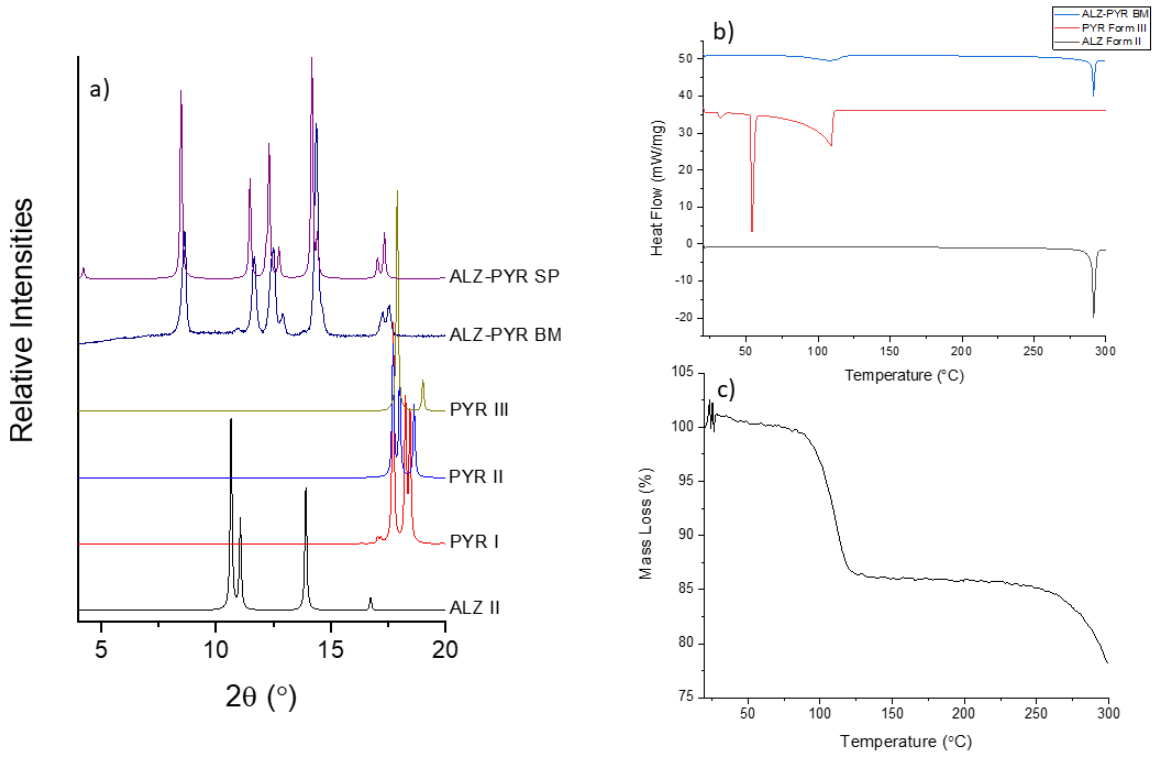

Figure 5.4: a) The PXRD pattern of ALZ-PYR BM compared with the simulated patterns of ALZ Form II and PYR Forms I, II and III; b) the DSC trace of ALZ-PYR BM compared with the traces for ALZ Form II and PYR Form III; c) the TGA trace of ALZ-PYR BM.

Solution crystallisation from toluene and ethyl acetate resulted in crystals which failed to index, however, suitable crystals were isolated from 1,4-dioxane which indexed as ALZ Form II. Visually, there was a very significant difference in solubility between the two components which made solution based crystallisation techniques unlikely to result in crystallisation. As a result, temperature cycling of the ball-milled powder was the chosen method and largely resulted in poor quality crystals, although crystals of suitable quality for SCXRD were obtained from 1,4-dioxane which yielded a 2:1 co-crystal. The crystal structure solution yielded a very high *R* factor of 22.7% and an R_{int} of 10.2% indicating that the crystal was of poor quality. The crystal diffracted out to a resolution of 0.8 Å which gives us a reliable connectivity of the atoms. The data were collected at 22.85 °C (296 K), but in the future data collected at −173.13 °C (100 K) would give more certainty to the structure.

Single crystal analysis of the ALZ-PYR (2:1) co-crystal crystallised in the monoclinic space group $P2_1/c$ with the asymmetric unit containing one molecule of alizarin and half a molecule of pyrazine as pyrazine is positioned on a crystallographic inversion centre. The intermolecular interaction

observed between ALZ and PYR results in strong O−H···N (2.779(9) Å) hydrogen bonds forming $D_1^1 2$ graph set motifs as well as $D_2^2 6$ motifs which are formed between one alizarin molecule and two pyrazine molecules. The alizarin molecules also form short contact interactions through weak O−H···O hydrogen bonds with pyrazine molecules forming short contact interactions with alizarin molecules through adjacent carbon atoms of the pyrazine linking with oxygen atom of alizarin via C−H···O interactions (*Figure 5.5*a). The crystal packing arrangement (*Figure 5.5*b) shows a typical herringbone type arrangement with the molecules adopting a zig-zag shape and exhibiting π-π stacking interactions between the layers.

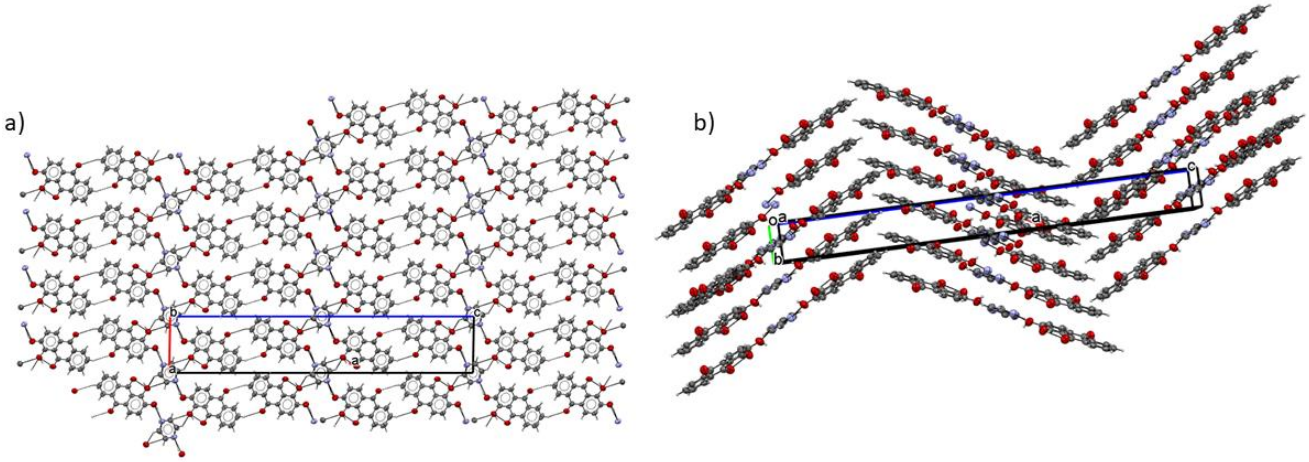

Figure 5.5: a) Short contact interactions observed in the hdrogen bonding network of ALZ-PYR (2:1) co-crystal; b) the crystal packing arrangement of ALZ-PYR showing the thermal ellipsoids at the 50% probability level.

5.3.2.3 Alizarin: Acridine

5.3.2.3.1 Polymorphism of Acridine

The solid form landscape of ACR has been extensively studied since it was first isolated in 1870 with eight polymorphs and a hydrate having been reported to date.[41] Forms II, III, IV, V and IX were reported from solvent evaporation, whereas Forms VI and VII were reported through the use of dicarboxylic acids in solution as crystallisation templates.[42] The crystal structures have been determined for all forms, except Form V for which only the unit cell parameters and space group have been determined and Form VIII was observed concomitantly with Form II from PXRD.[41] ACR polymorphs have been shown to occur concomitantly and transformations between forms are very common which is particularly rapid at elevated temperature. Form III is the commercial form and Form II is the thermodynamically stable form at ambient conditions.[43] Braga *et al.* showed that Form II converts to a high temperature form, designated as Form VIII at 101 °C with the two forms being related enantiotropically. However, the reverse transition was not observed upon cooling which indicates that this high temperature form is a metastable form at RT. This transition is much more visible from samples produced via melt crystallisation in comparison to samples obtained from re-crystallisation. This would suggest that Forms II and III are the most likely to be observed during our LAG experiments.

5.3.2.3.2 Characterisation of Alizarin: Acridine Co-crystal

An ALZ-ACR (1:1) co-crystal was isolated from a saturated ethanol solution co-crystallising in the $P\bar{1}$ space group with one molecule of alizarin and one molecule of acridine in the asymmetric unit in general positions. The two molecules are connected through the predicted strong O–H···N (2.748(3) Å) hydrogen bonds resulting in $D_1^1 2$ hydrogen bonding motifs. Much like the previous structures, short contact interactions connect alizarin molecules through weak O–H···O hydrogen bonds as well as additional contacts between acridine molecules forming dimers. These dimers also connect alizarin and acridine molecules through a combination of strong O–H···N and weak O–H···O hydrogen bonds. The molecules pack in a herringbone type arrangement which we have also seen the same packing arrangement with the pyridine/pyrazine structures, but in this case the alizarin and acridine molecules overlap with the two molecules being offset with each other which results in additional π-π stacking interactions between the layers (Figure 5.6).

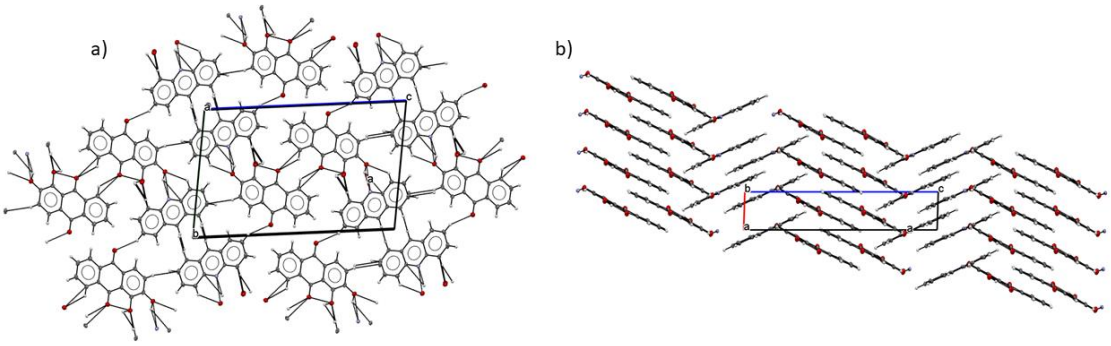

Figure 5.6: a) Short contacts in the hyrogen-bonded network of ALZ-ACR co-crystal; b) the crystal packing arrangement of ALZ-ACR showing the thermal ellipsoids at the 50% probability level.

The powder pattern from ball-milling experiments (*Figure 5.7*) features several reflections that can be attributed to ACR Form II occurring at approx. 7° and 11° 2θ as well as the presence of multiple reflections occurring at 2θ values of approx. 8°, 12.5°, 14.5°, 15.5° and 17° which are not present in either ALZ or ACR. Using the model obtained from the single crystal experiment, we were able to fit it to the data and perform a Pawley refinement (*Figure 5.7*). The fit indicates that the powder is largely phase pure where the differences are related to the peak fitting. There may be hints of a different phase at approx. 25.5°. The DSC trace of the ball-milled powder (*Figure 5.7*) features a single endothermic event with an onset temperature of 151.9 °C which does not correspond with the melting point of either ALZ or ACR, thereby confirming that this phase is pure. The TGA trace (*Figure 5.7*) shows no significant weight loss with the sample mass remaining constant until approx. 200 °C at which point the sample gradually decomposes.

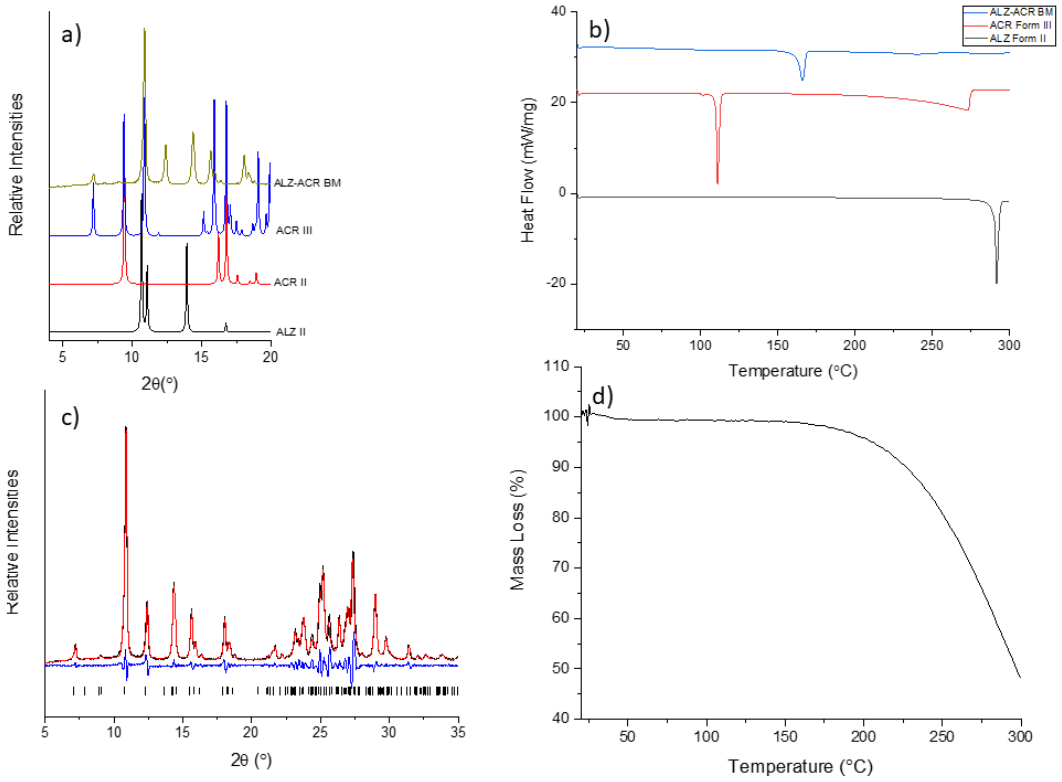

Figure 5.7: a) The PXRD pattern of ALZ-ACR BM from ethanol compared with the simulated patterns of ALZ Form II, ACR Form II, ACR Form II and ALZ-ACR; b) the DSC trace of ALZ-ACR BM compared with the traces of ALZ Form II and ACR Form III; c) the Pawley fit of ALZ-ACR BM with the unit cell parameters from the single crystal experiment; d) the TGA trace of ALZ-ACR BM.

5.3.2.4 Alizarin: Phenazine

5.3.2.4.1 Polymorphism of Phenazine

PHN has two known polymorphic forms, the *α* form and the *β* form.[44 -45] The *α* form is the commercial form which can be obtained through solvent evaporation from acetonitrile, toluene, 1,4-dioxane, THF and ethanol with the *β* form crystallising from nitromethane.[43] Braga *et al.* were able to show that the *β* form is the thermodynamically more stable form at RT.

5.3.2.4.2 Characterisation of Alizarin: Phenazine Co-crystal

Evaporative crystallisation yielded an ALZ-PHN (2:1) co-crystal from a saturated ethanol solution co-crystallising in the triclinic space group $P\bar{1}$ with the asymmetric unit containing half a molecule of phenazine and one molecule of alizarin as phenazine is positioned on a crystallographic inversion centre. The intermolecular interaction observed between ALZ and PHN results in strong O–H···N (2.803(7) Å) hydrogen bonds forming $D_1^1 2$ graph sets as well as $D_2^2 6$ motifs formed between one alizarin and two phenazine molecules. Much like the ACR structure, the short contacts between the two molecules result in the dimers made up both strong O–H···N and weak O–H···O interactions. The two structures are very similar which is not surprising considering that one of the carbons has been changed for a nitrogen to give the PHN structure. The crystal packing arrangement is the same

as that of ACR with the molecules overlapping each other which offsets the alizarin and phenazine rings allowing for the molecules to form a layered structure which exhibits π-π stacking interactions.

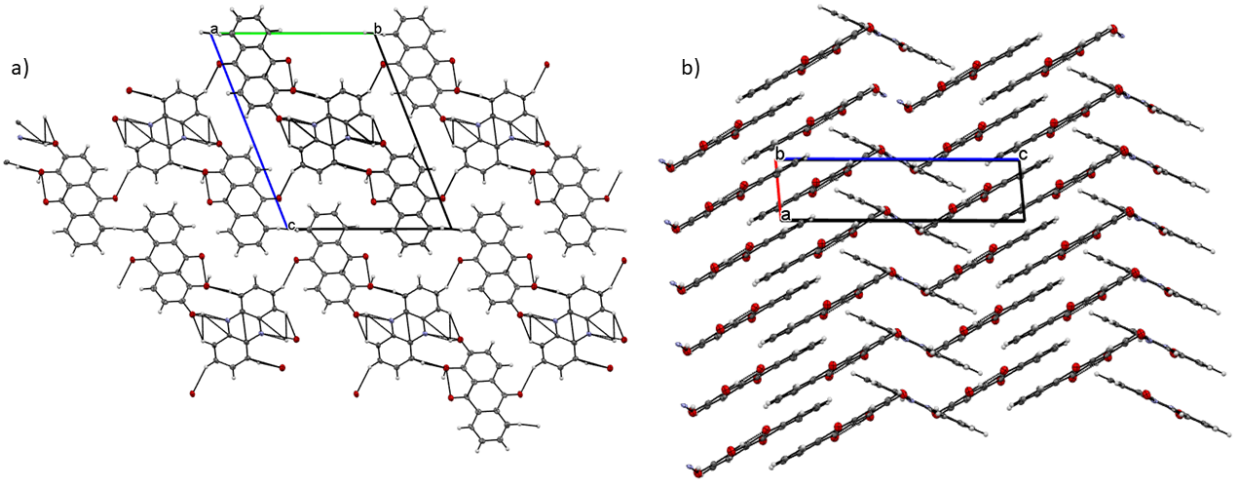

Figure 5.8: a) The hydrogen-bonding network of ALZ-PHN (2:1) showing the short contact interactions; b) the crystal packing arrangement sowing the herringbone crystal packing showing the thermal ellipsoids at the 50% probability level.

Comparison of the simulated PXRD pattern from the 2:1 co-crystal does not match with the solid obtained from the LAG experiment. The powder from LAG experiments (Figure 5.9) reveals the presence of a new crystalline powder pattern which cannot be attributed to either ALZ Form II, PHN α, PHN β or indeed the new co-crystalline phase that was obtained through solution crystallisation. This indicated that the ball-milled pattern is a new material. The DSC trace (Figure 5.9) shows two endothermic events, firstly, the thermal event with an onset temperature of 185.7 °C is thought to correspond to a phase transition and the main endothermic event with an onset temperature of 221.8 °C corresponds to the melting of this material. The melting point of this material does not match either ALZ Form II or PHN α, further confirming the presence of a new phase.

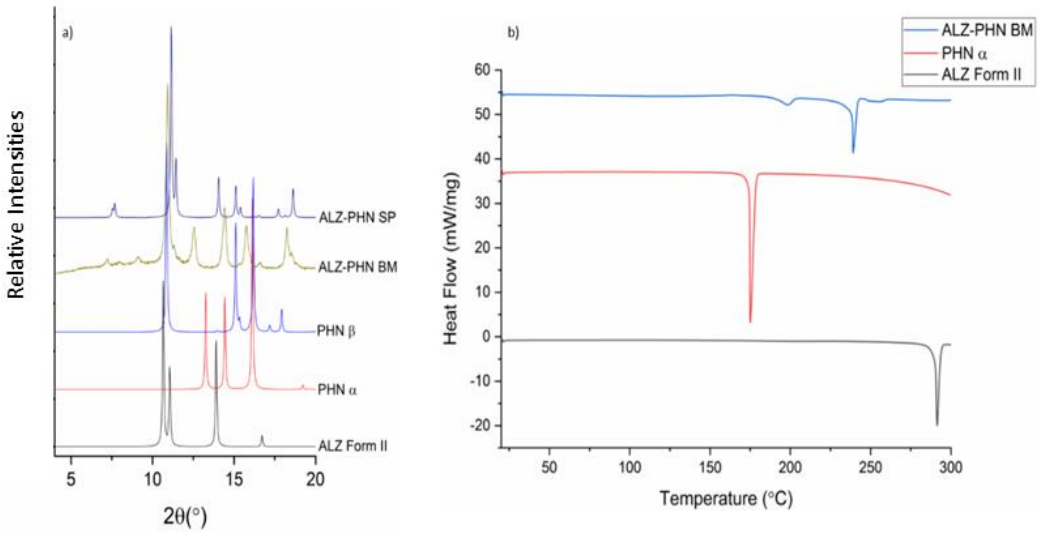

Figure 5.9: a) The PXRD pattern of ALZ-PHN BM from ethanol compared with the simulated patterns of ALZ Form II, PHN *α*, PHN *β* and ALZ-PHN; b) the DSC trace of ALZ-PHN BM compared with the traces of ALZ Form II and PHN *α*.

The DSC trace of the LAG product (Figure 5.9) indicated that the material underwent a phase transition at approximately 200 °C and so we investigated the change in the solid through variable temperature PXRD. The PXRD patterns collected up to 125 °C shows that the ambient temperature phase is still present. Beyond this temperature, there is the emergence of several new peaks at approximately 13° and 19° 2*ϑ* indicating the appearance of a new phase. We heated the sample to a maximum temperature of 210 °C which is beyond the small endothermic event, hence should provide a diffraction pattern of this suspected new phase. The final pattern collected at 25 °C after cooling of the sample shows a clear sharpening of the peaks compared to the patterns at 200 °C and 210 °C suggesting that this high temperature phase is simply a mixture of ALZ and PHN.

At the end of the experiment, we observed a change in the crystalline material when the sample chamber was opened. The crystallised material in the chamber possessed two distinct morphologies with different colours, greyish plates and orange needles (*Figure 5.10*). The greyish plates indexed as *a* = 7.08 Å, *b* = 5.07 Å, *c* = 12.77 Å, *β* = 102.36° which matches the unit cell parameters for the *α* form of PHN. However, the orange needles were not of sufficient quality for single crystal analysis and failed to index.

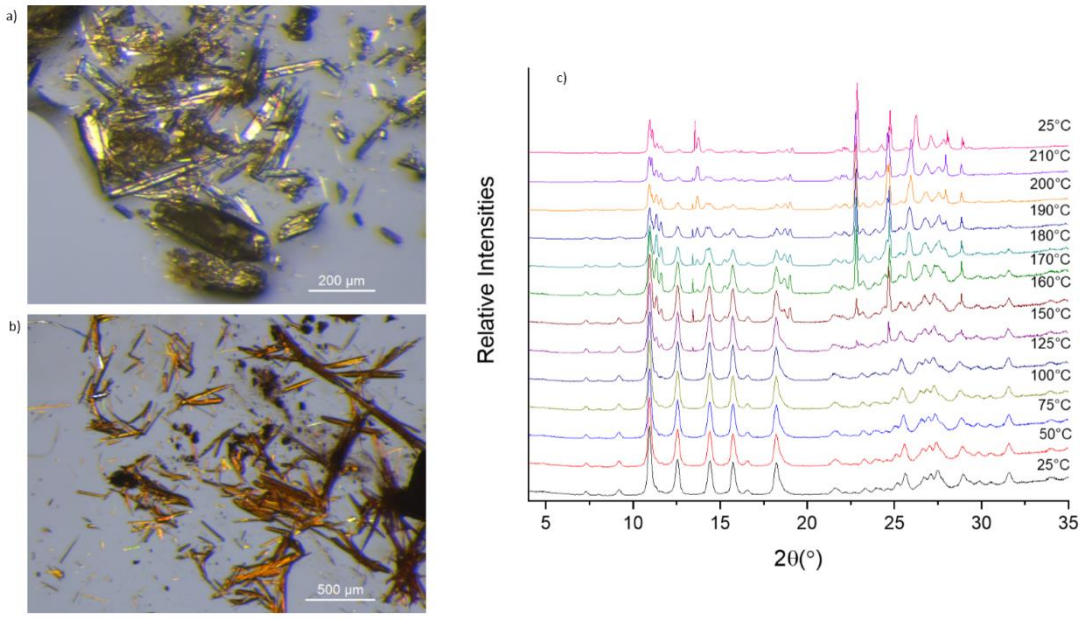

Figure 5.10: a) and b) Microscope images of the greyish plates and orange needles obtained from crystallisation within the VT sample chamber respectively; b) VT PXRD of ALZ-PHN BM from ethanol collected at 25 °C increments from 25 °C to 150 °C, followed by 10 °C increments from 150 °C to 210 °C before being cooled and collected at 25 °C.

The PXRD patterns from the VT experiment were Pawley fitted to yield the unit cell parameters for the ambient temperature ball-milled pattern which we have shown does not match any of the existing forms of either ALZ, PHN or the new 2:1 co-crystal. The obtained unit cell parameters (*Figure 5.11*) match with the ALZ-ACR co-crystal unit cell parameters indicating that this ball-milled phase is likely isomorphous with the ACR co-crystal. The ALZ-PHN ball-milled product was Pawley fitted with the ACR and PHN co-crystals to confirm whether this phase was in fact isomorphous or isostructural with the ACR co-crystal. The fits clearly indicate that the phase matches the ACR phase confirming indicating that the two materials are most likely isomorphous, however, further work would be required to confirm this.

Table 5.3: Unit cell parameters for ALZ-PHN BM as a function of temperature from 25 °C to 160 °C

	Unit Cell Parameters		
Temperature (°C)	*a*, *b*, *c* (Å)	*α*, *β*, *γ* (°)	*V* (Å^3)
25	3.920876, 12.667742, 19.579723	98.18471, 90.48601, 93.63685	960.503
50	3.951943, 12.597750, 19.479151	98.10968, 90.23253, 94.41536	957.124
75	3.965697, 12.609808, 19.491580	98.12154, 90.37108, 94.36715	961.985
100	3.974129, 12.616205, 19.489382	98.12351, 90.42181, 94.29860	964.481
125	3.979797, 12.607564, 19.450670	98.10655, 90.45113, 94.21180	963.422
150	3.979775, 12.605660, 19.417084	98.08748, 90.43560, 94.20811	961.664
160	3.992868, 12.619143, 19.412873	98.05485, 90.48733, 94.18904	965.737

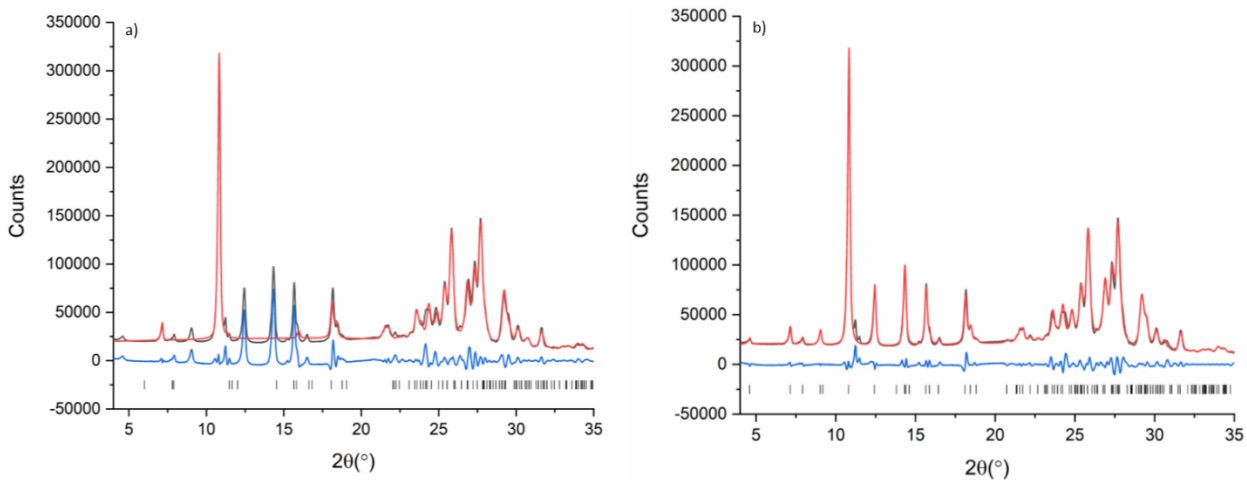

Figure 5.11: a) The Pawley fit of the ball-milled ALZ-PHN phase with the unit cell parameters from the PHN single crystal experiment and b) the ACR single crystal experiment respectively indicating the match with the ACR structure.

Now that we had formed multi-component materials of ALZ, we wanted to investigate whether these new materials would show a shift in the colour in solution with respect to pure ALZ. The UV/Vis (Figure 5.12) clearly indicated that there was no shift in the colour of any of the forms compared with ALZ, so we would look to investigate the hair dyeing ability of these ALZ co-crystals and assess whether they could be utilised as new supramolecular hair dyes in Section 5.3.3.

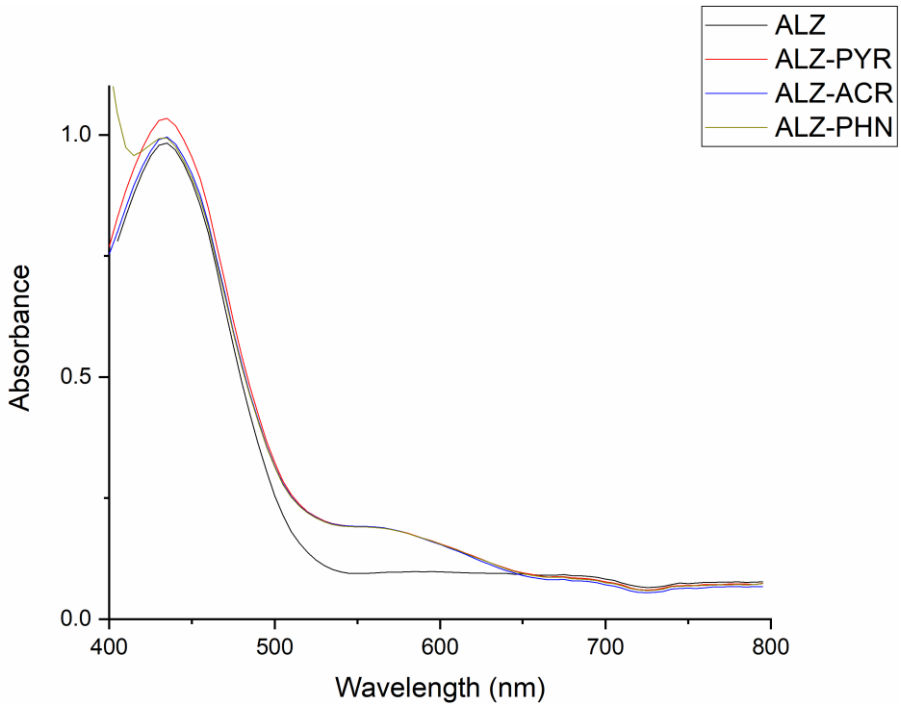

Figure 5.12: UV/Vis spectroscopic analysis of ALZ and the new multi-component forms in ethanol.

5.3.3 Hair Dyeing Experiments

Hair dyeing experiments were initially performed using pure alizarin as a benchmark with the adapted method using the formation of a paste to dye the hairs for 30 minutes, followed by washing for 30 minutes.[9] The hairs were then subsequently dyed using the new co-crystals to determine whether these new materials could be utilised as supramolecular hair dyes therefore expanding the range of available colours. Comparison of the hairs coloured with the co-crystals show no significant difference in colour over the pure material, although it was noted that in all cases the colour was maintained, but in this case there is no real advantage of the co-crystals compared with pure ALZ in terms of the hair dyeing.

Figure 5.13: Hairs dyed with ALZ, ALZ-PYR, ALZ-ACR and ALZ-PHN respectively after 30 minutes of dyeing, followed by 30 minutes of washing in hot soapy water at 50 °C.

5.4 Conclusions

This work has resulted in the formation of a new pyridine solvate as well as three new co-crystals of ALZ with the co-crystals being obtained through ball-milling as well as solution crystallisation, except for the ALZ-PHN co-crystal which resulted in three distinct phases. The ALZ-PHN ball-milled phase yielded a new pattern which did not correspond to ALZ, PHN or the ALZ-PHN (2:1) co-crystal from solution which was investigated through the use of VT-PXRD as the thermal data showed a possible phase transition at 200 °C. Pawley fitting of the VT-PXRD patterns indicated that the unit cell parameters of this phase matched the ALZ-ACR unit cell parameters confirming that the two co-crystals are in fact isostructural. The main aim of this experimental work was to generate a series of novel co-crystalline materials that could subsequently be used to colour hair. Although we have identified a series of new multi-component forms of ALZ, none of these materials show a change in colour, therefore offering no improvement with pure ALZ.

5.5 References

1. Dave, H. & Ledwani, L. A review on anthraquinones isolated from Cassia species and their applications. *Indian Journal of Natural Products and Resources. **3**, 291-319* (2012).

2. Nikoofard, H. & Jobi, H. N. Theoretical study of 1-amino-9,10-anthraquinone oligomers: Structural, electronic, and UV–visible spectral properties. *J. Mol. Struct.* **1191**, 138–144 (2019).

3. Duval, J., Pecher, V., Poujol, M. & Lesellier, E. Research advances for the extraction, analysis and uses of anthraquinones: A review. *Industrial Crops and Products* **94**, 812–833 (2016).

4. Li, M., Zhang, Q., He, H., Wang, J. R. & Mei, X. Vapor triggered fluorescent color changes among solvates of Emodin. *J. Mater. Chem. C* **5**, 5970–5976 (2017).

5. Li, M., Zhang, Q., Wang, J. R. & Mei, X. Mechanochromism triggered fluorescent color switching among polymorphs of a natural fluorescence pigment. *Chem. Commun.* **52**, 11288–11291 (2016).

6. Kashino, S., Senoo, K. & Haisa, M. Structure of 1,4-Diaminoanthraquinone Dihydrate. *Acta Crystallogr. Sect. C-Crystal Struct. Commun.* **44**, 1044–1046 (1988).

7. Park, B., Yoon, W., Yun, J., Ban, E., Yun, H. & Kim, A. Emodin-nicotinamide (1:2) cocrystal identified by thermal screening to improve emodin solubility. *Int. J. Pharm.* **557**, 26–35 (2019).

8. Armaghan, M., Amini, M. M., Ng, S. W. & Tiekink, E. R. T. Co-crystals of 1,8-dihydroxy-2,4,5,7-tetranitro-9,10-anthraquinone with dibenzothiophene and 4,6-dimethyldibenzothiophene. *Zeitschrift fur Krist.* **288**, 598–605 (2013).

9. Delori, A., Urquhart, A. J. & Oswald, I. D. H. Supramolecular hair dyes: A new application of cocrystallization. *CrystEngComm* **18**, 5360–5364 (2016).

10. Mohamed, S. & Li, L. From serendipity to supramolecular design: Assessing the utility of computed crystal form landscapes in inferring the risks of crystal hydration in carboxylic acids. *CrystEngComm* **20**, 6026–6039 (2018).

11. Aitipamula, S., Chow, P. S. & Tan, R. B. H. Polymorphism in cocrystals: A review and assessment of its significance. *CrystEngComm* **16**, 3451–3465 (2014).

12. Nauha, E. & Nissinen, M. Co-crystals of an agrochemical active - A pyridine-amine synthon for a thioamide group. *J. Mol. Struct.* **1006**, 566–569 (2011).

13. Sinha, A. S., Khandavilli, U. B. R., O'Connor, E. L., Deadman, B. J., Maguire, A. R. & Lawrence, S. E. Novel co-crystals of the nutraceutical sinapic acid. *CrystEngComm* **17**, 4832–4841 (2015).

14. Connor, L. E., Vassileiou, A. D., Halbert, G. W., Johnston, B. F. & Oswald, I. D. H. Structural investigation and compression of a co-crystal of indomethacin and saccharin. *CrystEngComm* **21**, 4465–4472 (2019).

15. Millar, D. I. A., Maynard-Casely, H. E., Allan, D. R., Cumming, A. S., Lennie, A. R., Mackay, A. J., Oswald, I. D. H., Tang, C. C. & Pulham, C. R. Crystal engineering of energetic materials: Co-crystals of CL-20. *CrystEngComm* **14**, 3742–3749 (2012).

16. Zhao, L., Raval, V., Briigs, N. E. B., Bhardwaj, R. M., McGlone, T., Oswald, I. D. H. & Florence, A. J. From discovery to scale-up: *α*-lipoic acid: Nicotinamide co-crystals in a continuous oscillatory baffled crystalliser. *CrystEngComm* **16**, 5769–5780 (2014).

17. Takacs, L. The historical development of mechanochemistry. *Chem. Soc. Rev.* **42**, 7649–7659 (2013).

18. Howard, J. L., Cao, Q. & Browne, D. L. Mechanochemistry as an emerging tool for molecular synthesis: what can it offer? *Chem. Sci.* **9**, 3080–3094 (2018).

19. Hasa, D., Perissutti, B., Cepek, C., Bhardwaj, S., Carlino, E., Grassi, M., Invernizzi, S. & Voinovich, D. Drug salt formation via mechanochemistry: The case study of vincamine. *Mol. Pharm.* **10**, 211–224 (2013).

20. Bučar, D. K., Filip, S., Arhangelskis, M., Lloyd, G. O. & Jones, W. Advantages of mechanochemical cocrystallisation in the solid-state chemistry of pigments: colour-tuned fluorescein cocrystals. *CrystEngComm* **15**, 6289–6291 (2013).

21. Hasa, D., Pastore, M., Arhangelskis, M., Gabriele, B., Cruz-Cabeza, A. J., Rauber, G. S., Bond, A. D. & Jones, W. On the kinetics of solvate formation through mechanochemistry. *CrystEngComm* **21**, 2097–2104 (2019).

22. Friščić, T. & Jones, W. Recent Advances in Understanding the Mechanism of Cocrystal Formation via Grinding. *Cryst. Growth Des.* **9**, 1621–1637 (2009).

23. Trask, A. V., Haynes, D. A., Motherwell, W. D. S. & Jones, W. Screening for crystalline salts via mechanochemistry. *Chem. Commun.* ***1,*** 51–53 (2006).

24. Friščić, T., Halasz, I., Strobridge, F, C., Dinnebier, R. E., Stein, R. S., Fábián, L. & Curfsw, C. A rational approach to screen for hydrated forms of the pharmaceutical derivative magnesium

naproxen using liquid-assisted grinding. *CrystEngComm* **13**, 3125–3129 (2011).

25. Belenguer, A. M., Lampronti, G. I., Cruz-Cabeza, A. J., Hunter, C. A. & Sanders, J. K. M. Solvation and surface effects on polymorph stabilities at the nanoscale. *Chem. Sci.* **7**, 6617–6627 (2016).

26. Say-Liang-Fat, S. & Cornard, J. P. Al(III) complexation by alizarin studied by electronic spectroscopy and quantum chemical calculations. *Polyhedron* **30**, 2326–2332 (2011).

27. Desiraju, G. R. Supramolecular Synthons in Crystal Engineering—A New Organic Synthesis. *Angewandte Chemie* **34**, 2311–2327 (1995).

28. Cyranski, M. K., Jamroz, M. H., Rygula, A., Dobrowolski, J. C., Dobrzycki, L. & Baranska, M. On two alizarin polymorphs. *CrystEngComm* **14**, 3667–3676 (2012).

29. Cosier, B. J. & Glazer, A. M. A Nitrogen-gas-stream cryostat for general X-ray diffraction studies. *J. Appl. Crystallogr.* **19**, 105–107 (1986).

30. Bruker. APEX3. *APEX3; SAINT* (2016).

31. Sheldrick, G. M. SADABS program for area detector absorption correction. (2008).

32. Dolomanov, O. V., Bourhis, L. J., Gildea, R. J., Howard, J. A. K. & Puschmann, H. *OLEX2* : a complete structure solution, refinement and analysis program. *J. Appl. Crystallogr.* **42**, 339–341 (2009).

33. Sheldrick, G. M. SHELXT - Integrated space-group and crystal-structure determination. *Acta Crystallogr. Sect. A Found. Crystallogr.* **71**, 3–8 (2015).

34. Sheldrick, G. M. Crystal structure refinement with SHELXL. *Acta Crystallogr. Sect. C Struct. Chem.* **71**, 3–8 (2015).

35. Aitipamula, S., Chow, P. S. & Tan, R. B. H. The solvates of sulfamerazine: Structural, thermochemical, and desolvation studies. *CrystEngComm* **14**, 691–699 (2012).

36. Patyk, E., Podsiadło, M. & Katrusiak, A. Discrete CH···N Bonded Patterns Modified by Temperature and Pressure in Four Pyrazine Polymorphs. *Cryst. Growth Des.* **15**, 5670–5674 (2015).

37. de With, G., Harkema, S. & Feil, D. Crystal structure and charge distribution of pyrazine: effects of extinction, thermal diffuse scattering and series termination. *Acta Crystallogr. Sect. B Struct. Crystallogr. Cryst. Chem.* **32**, 3178–3185 (1976).

38. Schmidt, R., Martin Scholze, H. & Stolle, A. Temperature progression in a mixer ball mill. *Int. J. Ind. Chem.* **7**, 181–186 (2016).

39. Colacino, E., Nun, P., Colacino, F. M., Martinez, J. & Lamaty, F. Solvent-free synthesis of nitrones in a ball-mill. *Tetrahedron* **64**, 5569–5576 (2008).

40. McKissic, K. S., Caruso, J. T., Blair, R. G. & Mack, J. Comparison of shaking versus baking: Further understanding the energetics of a mechanochemical reaction. *Green Chem.* **16**, 1628–1632 (2014).

41. Schur, E., Bernstein, J., Price, L. S., Guo, R., Price, S. L., Lapidus, S. H. & Stephens, P. W. The (Current) Acridine Solid Form Landscape: Eight Polymorphs and a Hydrate. *Cryst. Growth Des.* **19**, 4884–4893 (2019).

42. Mei, X. & Wolf, C. Formation of new polymorphs of acridine using dicarboxylic acids as crystallization templates in solution. *Cryst. Growth Des.* (2004).

43. Braga, D., Grepioni, F., Maini, L., Mazzeo, P. P. & Rubini, K. Solvent-free preparation of co-crystals of phenazine and acridine with vanillin. *Thermochim. Acta* **507**–**508**, 1–8 (2010).

44. Herbstein, F. H. & Schmidt, G. M. J. The crystal and molecular structures of heterocyclic compounds. I. The analysis of the crystal structure of *α*-phenazine. *Acta Crystallogr.* **8**, 399–405 (1955).

45. Jankowski, W. & Gdaniec, M. The *β*-polymorph of phenazine. *Acta Crystallogr. Sect. C Cryst. Struct. Commun.* **58**, 181-182 (2002).

Chapter Six – Conclusions and Future Work

6 Conclusions & Future Work

The main aim of this body of work was to further explore the use of co-crystallisation as a strategy to prepare coloured multi-component forms that could be used as supramolecular hair dyes with the goal of moving away from PPD. The ability of these new multi-component forms to increase the range of available colours as well as investigating their ability to colour hair has been studied.

In Chapter 3, the solution reactivity of PPD was investigated through the use of various analytical techniques to better understand the reaction pathway that leads to the deeply coloured solutions that were observed during our studies. Initial observations showed that PPD solutions changed colour going from a colourless solution to a deep red/black over a period of 12 weeks which was monitored through UV/Vis indicating that the absorbance continued to increase indicating that PPD reacted with itself at which point the reaction plateaued. The salt forms of PPD were also investigated to understand if salt formation would help stabilise the reactive PPD which from our studies, we concluded that in the case of the PPD-L system this was the case, however, we are unsure of the exact mechanism by which this is achieved.

Chapter 4 investigated the impact small structural changes to PPD would have on the resultant colour through co-crystallisation of *o*-phenylenediamine, *m*-phenylenediamine and 4-iodoaniline with the same co-formers as PPD. Co-crystallisation of OPD and MPD successfully resulted in a series of salt forms with UV/Vis analysis showing that these salts had undergone a bathochromic shift in comparison to pure OPD and MPD. The shifts in colour were shown to occur overtime most likely as a result of oxidation much like PPD. Ionisation of PPD was investigated as another route to altering the colour which was first attempted through recrystallization from a hydrochloric acid solution resulting in a purple solution indicating that ionisation was a successful route to altering the colour. The next steps with ionisation of PPD was to investigate the formation of ionic co-crystals which were attempted using both milling and solution crystallisation, however, all attempts to prepare ionic co-crystals were unsuccessful. Co-crystallisation of 4IODAN was also investigated to ascertain whether new multi-component forms of 4IODAN would shift the colour and how small structural changes would impact upon the colour and reactivity of the system. This resulted in a salt hydrate with TMA and the system underwent a condensation reaction during attempted co-crystallisation experiments between 4IODAN and L, although the TMA showed no shift in the colour. In conclusion, this chapter generated new multi-component forms, but with the same reactivity observed with PPD and reiterated the need to move away from phenylenediamines from a reactivity and safety standpoint.

Chapter 5 investigated the possibility of creating new multi-component forms of alizarin which could be used as supramolecular hair dyes as a replacement to PPD with their hair dyeing ability also being assessed. Co-crystallisation of ALZ resulted in a pyridine solvate as well as three co-crystals with pyrazine, acridine and phenazine which were obtained via milling and solution crystallisation. The ALZ-PHN system resulted in two distinct co-crystals, one of which was obtained from solution and the other which was obtained through ball milling. VT-PXRD was performed on the ALZ-PHN ball-milled phase as the thermal data indicated a possible phase transition at 200 °C with Pawley refinement indicating that this phase was isostructural to the ACR co-crystal. The hair dyeing ability of these new multi-component forms was assessed, although none of these materials showed a change in colour as a result of co-crystallisation, there was no improvement over pure ALZ.

Overall, in conclusion, the goal of this project was to explore the potential of identifying new multi-component crystalline materials that could be used instead of PPD. Although we have identified a range of new co-crystalline materials, none of these result in an altering of the colour or an improvement over the starting material in terms of the hair dyeing ability. Several systems were also investigated that haven't been included in this thesis which also failed to yield any promising candidates to move forward with as a replacement to PPD suggesting that with regards to future work, co-crystallisation may not be the way to move forward.